Project No. 15-8251

Enhanced Performance Fast Reactors with Engineered Passive Safety Systems

Reactor Concepts Research Development and Demonstration (RCRD&D)

Ehud Greenspan
University of California, Berkeley

Thomas Sowinski, Federal POC
Matthew Denman, Technical POC

NEUP Nuclear Energy University Programs
U.S. Department of Energy

Enhanced Performance Fast Reactors with Engineered Passive Safety System

NEUP Project #15-8251

Final Report

PI: E. Greenspan[a]

Contributors: T. Fanning[b], M. Fratoni[a], M. Gradecka[a], C. Keckler[a], and S. Qvist[a]

[a]Department of Nuclear Engineering, University of California, Berkeley, CA

[b]Nuclear Engineering Division, Argonne National Laboratory, Lemont, IL

December 2018

Executive Summary

This report summarizes the work and results of NEUP Project #15-8251, "Enhanced Performance Fast Reactors with Engineered Passive Safety System," performed from 2015-2018 at UC Berkeley and Argonne National Laboratory. This project concerns the incorporation of a novel engineered passive safety system, called the Autonomous Reactivity Control (ARC) system, into Sodium-cooled Fast Reactors (SFRs) to improve their transient and economic performance. The first part of this project consisted of fleshing out the basic principles and the manufacturing process for an SFR fuel assembly with the ARC system installed, with the details provided in high-quality, step-by-step CAD drawings. Once the detailed design is laid out, high-fidelity simulations were performed to optimize the dimensions of important ARC system components and to quantify the standalone time-response of ARC systems in a typical SFR environment. These high-fidelity simulations were used to create reduced-order models of ARC system response which could be incorporated into the SAS4A/SASSYS-1 whole-core transient models. In order to accurately account for the time-response of ARC systems in whole-core transient simulations, modifications were made to the SAS4A/SASSYS-1 transient code. These new capabilities were tested and incorporated into the production version of the code, and have been used extensively in this analysis.

Before performing whole-core transient calculations, the two reference cores selected for this study to cover a wide design space were simulated and characterized. The two reference cores, (1) a medium-sized oxide-fueled Advanced Burner Reactor and (2) a large metal-fueled Breed-and-Burn core, challenge conventional means of achieving passive safety. Because the two cores vary substantially, simulating the ARC system in both allows for conclusions to be drawn about the applicability of ARC systems in different SFRs. Once both cores were fully characterized, transient calculations were performed to understand the complicated interplay between the ARC system and other inherent reactivity feedback mechanisms. By performing parametric studies of the transient behavior, ARC system designs that best improve transient performance in each core were identified. Once transient improvements were established, the transient calculations were extended to improve reactor economics through design modifications. Upon establishing the potential benefits of ARC system inclusion, the study examines the negative neutronic implications of incorporating ARC systems into the reference cores. The study concludes by discussing a number of knowledge gaps that exist which may have important implications for ARC system implementation.

Ultimately, the results of this project indicate that ARC systems may provide an effective means to improve transient performance in certain types of systems. The transient simulations in the oxide Advanced Burner Reactor showed that significant margin to coolant boiling and fuel melting could be

gained through the use of a properly designed ARC system, thus improving inherent safety. While oscillatory behavior was induced in the transient response for certain combinations of ARC system parameters, the oscillation-free design space that can be effectively used to improve performance was found to be large, and the additional margin was demonstrated to allow economical improvements to the core design. Conversely, difficulties were encountered in the Breed-and-Burn core due to fundamental aspects of the core design. The combination of a particularly strong positive coolant void feedback and the use of metallic fuel allowed for diverging oscillations to manifest in response to certain transient initiators, and in the end it was found that the current ARC system design could not simultaneously enable passive safety in all transients examined. In order for complete passive safety to be achieved, a mechanism for slowing the reverse actuation of ARC systems is necessary. Regardless, the standard ARC system was able to improve the performance of two out of the three examined transients by increasing the margin to boiling in Loss of Heat Sink transients and avoiding boiling in Transient Overpower accidents. Additionally, no significant barriers to implementation were found, although the issue of tritium production should be closely monitored in any core incorporating ARC systems. Still, a number of technology gaps exist, and these are discussed at the conclusion of the report to recommend directions for future work.

Contents

1 Background and Motivation **10**

2 ARC System Principles **12**
2.1 Basic Design and Response Sequence . . . 12
2.2 Materials Selection . . . 12
2.2.1 The mutual solubility of potassium and lithium . . . 15
2.2.2 Properties of ARC materials . . . 17

3 ARC System Manufacturing Process **20**
3.1 Components and Configuration . . . 20
3.2 Assembly Process . . . 21
3.3 Summary of Findings . . . 23

4 High-fidelity ARC System Characterization **24**
4.1 Design Constraints . . . 26
4.2 Geometry and Numerical Modeling . . . 28
4.3 Results . . . 30
4.3.1 Geometry of Upper Reservoir at Constant Volume . . . 31
4.3.2 Reduced Volume Upper Reservoir . . . 32
4.4 Impact of Coolant Flow Rate on Time Response . . . 34
4.5 Effect of Wall Thermal Expansion . . . 35
4.6 Summary of Results . . . 37

5 ARC System Simulation Capabilities **38**

6 Reference Cores **42**
6.1 Oxide ABR Core . . . 42
6.2 B&B Core . . . 42
6.3 Comparison of the Reference Cores . . . 45
6.4 Plant Systems . . . 48

7 Performance of the Oxide ABR core **52**
7.1 Transient Model . . . 52
7.2 Transient Initiators and Assumptions . . . 54
7.3 Nominal performance . . . 55
7.4 Performance with ARC inclusion . . . 57
7.5 Suppression of Oscillations in the ULOF . . . 60
7.6 Summary of Results . . . 63

8 Performance of the B&B core **64**
8.1 Transient Model . . . 64
8.2 Transient Initiators and Assumptions . . . 64
8.3 Nominal Performance . . . 65
8.4 Nominal Performance Sensitivity Studies . . . 67
8.4.1 Pump Coast Down Time . . . 67
8.4.2 Control Rod Driveline Feedback . . . 67
8.4.3 Rate of Reactivity Insertion . . . 68
8.4.4 Locked Rotor Loss Coefficient . . . 69
8.5 Performance with ARC inclusion . . . 69

8.6 Summary of Results . . . 72

9 Neutronic Impact of ARC System Inclusion **74**
9.1 Methodology . . . 74
9.1.1 Computational models . . . 74
9.1.2 Determination of soluble lithium distribution . . . 75
9.2 Neutronic impact . . . 80
9.2.1 Removal of fuel . . . 80
9.2.2 Addition of ARC tubes . . . 81
9.2.3 Soluble absorber . . . 82
9.3 Tritium production . . . 83
9.3.1 In-core tritium production . . . 83
9.3.2 Ex-core tritium production . . . 84
9.4 Depletion of lithium reservoir inventory . . . 86
9.4.1 Lower reservoir depletion through mass diffusion . . . 86
9.4.2 Lower reservoir depletion through neutron transmutation . . . 87
9.5 Validation of Infinite Sink Assumption . . . 88
9.6 Impact of System Breach . . . 90
9.6.1 Leakage of Inert Gas . . . 92
9.6.2 Leakage of Absorber Fluid . . . 94
9.7 Extension of Results to the ABR Core . . . 96

10 Improving Economic Performance **97**
10.1 ARC System Design . . . 97
10.2 Core Power Uprate . . . 97
10.3 Flow Halving Time Reduction . . . 99
10.4 Extension of Results to Higher Conversion Ratio Cores . . . 99
10.5 Extension of Results to Metallic-fuel Cores . . . 101

11 Technology Gap Analysis **102**
11.1 Technology Gaps . . . 102
11.2 Summary and Ranking . . . 105

12 Summary **106**

List of Figures

1 An ARC-equipped fuel assembly (not to scale). 13
2 CAD model of the top of an ARC-equipped fuel assembly. 14
3 CAD model of the bottom part of an ARC-equipped fuel assembly. 14
4 Schematic view of the lower ARC reservoir at different states. Green, red, and blue are the expander, absorber, and inert fluids, respectively. 15
5 The K-Li phase diagram as calculated by Zhang. 16
6 Nosepiece of ARC-equipped assembly. 21
7 Cut-through view of the upper part of the nosepiece, showing the lower reservoir and its shielding region as well as the attachment of the outer ARC-tube. 21
8 The pin mounting rail, modified to accomodate more stabilization rods (4 in total) and a single ARC-tube. 22
9 The rod bundle consists of the lower end plug, cladding, fuel (inside the cladding) and upper end plug, and wires wrapped around the rods for spacing. 22
10 The upper gas reservoir is open at the top and closed at the bottom, and includes a hole through which the outer ARC tube is mounted and welded. 23
11 Isometric cut-through view of the hexagonal duct section. 23
12 At the top of the lower duct section, there are two reservoir positioning slots on opposite sides, in to which the slits attached to the upper liquid reservoirs are inserted from above. 24
13 The upper ARC (liquid) reservoir is located on top of the gas reservoir. It has two duct-attachment slits protuding from its sides, and the inner ARC tube is welded through the bottom surface. 24
14 Cut-through view of the upper ARC (liquid) reservoir showing the attachment of the inner ARC tube. 25
15 Isometric view of the upper duct section and handling head. 25
16 Cut-through iso-view of the upper duct section and handling head. The thicker uppermost section of the handling head extends beyond the outer limit of the duct to form the top load pad. 26
17 Step #1, The pin mounting rails and stabilization bars are inserted in to their respective slots in the nose piece. 26
18 Step #2, The rod bundle (containing the pre-fabricated complete fuel rods and wire-wraps) is slid on to the pin mounting rails. 27
19 Step #3, The gas reservoir is welded to the outer ARC tube. 27
20 Step #4, The lower section of the duct is welded to the nose-piece. 28
21 Step #5, The upper liquid is positioned on top of the gas reservoir, with the inner ARC tube inserted in to the outer ARC tub and the positioning fins inserted in to the duct slots. The liquid reservoir is welded on to the gas reservoir at the inner and outer edges. 28
22 Step #6, The uppermost section, consisting of the upper duct section and the handling head, is welded on to the lower duct section. 29
23 Iso-view of final assembly (with transparent ducts and handling head). 29
24 Example of the advanced UR design. 30
25 Monitor of the surface averaged pressure at the coolant inlet boundary. 32
26 Monitor of the surface maximum velocity magnitude at the coolant outlet boundary. . . . 32
27 Temperature (°C) contour of the G2 design 1 cm away from the Y-Z symmetry plane. . . 33
28 Comparison of mass fraction of potassium in UR for designs G1-G3. 33
29 Summary of performance for designs G1-G3. 34
30 Summary of performance for designs G2, G4, and G5. 34
31 The impact of flow rate on the value of τ as calculated by COMSOL for the ABR core. . 35
32 2D axisymmetric geometry used to evaluate the impact of UR wall thermal expansion. . . 36

33 Test of the variable lag-compensator implemented into SAS4A/SASSYS-1 with a sine wave for the value of τ and a sine wave driving function. . . . 39
34 Comparison between the SAS variable lag-compensator result and Wolfram Mathematica result for the test case shown in Figure 33. . . . 40
35 Coolant and reservoir temperatures during a UTOP event in the metallic ABR with a step change in τ showing that the curvature of the reservoir temperature curve changes with τ. 41
36 Flowrate, tau, outlet temperature, and ARC reservoir temperature during the first two minutes of a ULOF transient in the oxide ABR with an ARC system installed. . . . 41
37 Core layout for the reference ABR core [1]. . . . 42
38 Distribution of fuel worth in the ABR core. . . . 43
39 Distribution of cladding worth in the ABR core. . . . 44
40 Distribution of coolant worth in the ABR core. Values on the fine mesh of Figures 38 and 39 were not available for the coolant worth. . . . 45
41 Distribution of fuel doppler worth in the ABR core under flooded conditions. Values on the fine mesh of Figures 38 and 39 were not available for the doppler worth. . . . 46
42 Core layout and shuffling scheme for the reference B&B core. . . . 48
43 Assembly-wise power profile of the B&B core at EOEC. . . . 49
44 Distribution of fuel worth in the B&B core at EOEC. . . . 50
45 Distribution of cladding worth in the B&B core at EOEC. . . . 50
46 Distribution of coolant worth in the B&B core at EOEC. . . . 51
47 Distribution of doppler worth in the B&B core at EOEC under flooded conditions. . . . 51
48 Assembly mass flow rates in the B&B core resulting from the orificing procedure and constraints outlined in Table 7. . . . 52
49 General plant layout for both reference cores. . . . 53
50 Grouping of assemblies into channels for the transient model of the ABR core. . . . 54
51 Channel model used to represent the core heat transfer in the transient model. . . . 55
52 Response to a ULOHS accident in the nominal oxide ABR core. . . . 56
53 Response to a UTOP accident in the nominal oxide ABR core. . . . 58
54 Response to a ULOF accident in the nominal oxide ABR core. . . . 59
55 Margin to coolant boiling gained during each transient as a function of w and ΔT_{act} for $S = 65$°C. . . . 60
56 Margin to coolant boiling gained as a function of S with $w = 0.87\$$ and $\Delta T_{act} = 10$°C. . . . 61
57 Transient response during the early phase of a ULOF accident in the oxide ABR equipped with an ARC system of $S = 65$ C, $w = \$0.87$, and $\Delta T_{act} = 10$ C. . . . 62
58 Reactivity inserted by the ARC system into the oxide ABR during the ULOF transient with increasing actuation span, S. $w = \$0.87$ and $\Delta T_{act} = 10$ C. . . . 62
59 Reactivity injected by the ARC system into the oxide ABR during the ULOF transient with increasing heat transfer resistance from coolant to upper reservoir. $w = \$0.87$, $S = 65$ C, and $\Delta T_{act} = 10$ C. . . . 63
60 Grouping of assemblies into channels for the transient model of the B&B core. . . . 64
61 Power and flow with time for the ULOHS scenario in the B&B core without ARC system inclusion. . . . 66
62 Reactivity feedbacks with time for the ULOHS scenario in the B&B core without ARC system inclusion. . . . 66
63 Core temperatures with time for the ULOHS scenario in the B&B core without ARC system inclusion. . . . 67
64 Reactivity feedbacks with time for the ULOF scenario in the B&B core without ARC system inclusion. . . . 68
65 Reactivity feedbacks with time for the UTOP scenario in the B&B core without ARC system inclusion. . . . 69

66 Time of boiling initiation in the ULOF transient of the B&B core with varying primary pump coast down halving times. 70
67 Time of boiling initiation in the B&B core with varying control rod drive thermal expansion coefficients for all three transients. 71
68 Time of boiling initiation in the UTOP of the B&B core with varying reactivity insertion rates. 72
69 Time of boiling initiation in the ULOF of the B&B core with varying locked rotor loss coefficients. 73
70 Net and coolant reactivity components in the UTOP of the B&B core with varying locked rotor loss coefficients. 74
71 Margin to coolant boiling gained in the ULOHS scenario of the B&B core with ARC system inclusion as a function of ARC system design parameters. 75
72 Power and flow with time for the UTOP scenario in the B&B core with ARC system inclusion. 76
73 Reactivity feedbacks with time for the UTOP scenario in the B&B core with ARC system inclusion. 77
74 Core temperatures with time for the UTOP scenario in the B&B core with ARC system inclusion. 78
75 ARC system reactivity insertion in the UTOP as τ is increased. 79
76 Power and flow with time for the UTOP scenario in the B&B core with ARC system inclusion and $\tau = 250$ s. 80
77 Reactivity feedbacks with time for the UTOP scenario in the B&B core with ARC system inclusion and $\tau = 250$ s. 81
78 Core temperatures with time for the UTOP scenario in the B&B core with ARC system inclusion and $\tau = 250$ s. 82
79 Margin to coolant boiling gained in the UTOP scenario of the B&B core with ARC system inclusion as a function of ARC system design parameters. 83
80 Peak coolant temperatures in the ULOHS scenario of the B&B core as a function of ARC design parameters with increasing τ. 84
81 Reactivity feedbacks with time for the ULOF scenario in the B&B core with ARC system inclusion. 85
82 Actual and simplified ARC system geometries used to study the impact of dissolved lithium in the core, fictitiously depicting the migration of lithium upwards into the active core. . . 86
83 Normalized neutron spectra at two radial points within the B&B core. Batch 5 corresponds to a position close to the high flux zone and has experienced 12 burnup cycles, while Batch 10 corresponds to a position close to the core periphery and has experienced 2 burnup cycles. 87
84 Dimensionless ratio as a function of residence time in the core for two different values of neutron flux. 88
85 k_{eff} evolution in the equilibrium cycle with the fuel removed from a number of pins. . . . 89
86 Amount of tritium produced in the lower reservoir and lower shield as the lower shield thickness is increased, as well as the nominal amount produced in-core. 90
87 Rate of diffusion of lithium atoms from the lower reservoir into the active core as a function of the radius of the inner ARC tube for different assumed diffusion coefficients assuming an infinite sink for Li atoms at mid-core. All curves assume three ARC tubes per assembly. . 91
88 Atom percent of lithium dissolved in upper reservoir potassium as a function of time for various upper reservoir volumes, along with the solubility limits at operating and refueling temperatures. 92
89 Reactivity insertion as a function of breach position for the breach of a single ARC system in the B&B core with $r_i = 0.23$ cm, $P_{Ai}/P_c = 1.5$, and three ARC tubes per assembly. . . 94
90 Maximum reactivity insertion as a function of the inner gas volume radius for a variety of ARC tube initial pressures, assuming the breach of an ARC system with three ARC tubes. 95

91 Power transient response to a breach in a single ARC system leading to a sudden leak of absorber fluid into the coolant. 96
92 Reactivity transient response to a breach in a single ARC system leading to a sudden leak of absorber fluid into the coolant. 97
93 Peak temperature transient response to a breach in a single ARC system leading to a sudden leak of absorber fluid into the coolant. 98
94 Power and flow in the oxide ABR with pump coast down halving time of 5 seconds, both with and without the ARC system. 100
95 Core reactivity in the oxide ABR with pump coast down halving time of 5 seconds, both with and without the ARC system. 101
96 Peak temperatures in the oxide ABR with pump coast down halving time of 5 seconds, both with and without the ARC system. 102

List of Tables

1 Initial and boundary conditions for the CFD simulations. 30
2 General dimensions of the ARC geometry consistent over the optimization efforts. 31
3 General dimensions of the ARC geometries considered in the constant-volume stage of the optimization. 31
4 General dimensions of the ARC geometries considered in the reduced-volume stage of the optimization. 35
5 Amount of potassium expelled from the upper reservoir using different thermal expansion models for the UR walls. 37
6 TRU vector of the charge fuel of the ABR core [1]. 43
7 Nominal constraints used for the orificing optimization in the B&B core. 45
8 Design parameters of the oxide ABR and metallic B&B cores. 47
9 Nodalization of the core channel model for the ABR. 56
10 Assumptions specific to each of the three transients examined in the ABR core. 56
11 Peak transient temperatures in the nominal transients of the ABR reference core. 57
12 Margin to coolant boiling gained over the reference design through optimal ARC system inclusion. 61
13 Nodalization of the core channel model for the BnB core. 65
14 Assumptions specific to each of the three transients examined in the B&B core. 65
15 Time of boiling initiation in the B&B core without ARC system inclusion. 65
16 Amount of lower reservoir lithium lost to transmutation, assuming the reservoir is located immediately below the lower shield and its lithium is 100% enriched in ^{6}Li. 88
17 Difference in k_{eff} of the B&B core at BOEC and EOEC with a single ARC system's worth of absorber fluid at the location of highest worth. 95
18 Peak temperatures in the three unprotected transients for the nominal and uprated cores, showing the impact of the ARC system. 99
19 Technology gaps rated according to their importance and ease of resolution. 105

1 Background and Motivation

The establishment of passive safety (i.e. the ability for a reactor to avoid catastrophic consequences in response to an initiating event without operator intervention) has long been a challengt to the Sodium Fast Reactor (SFR) design community. It has been computationally and experimentally validated that small cores with high neutron leakage probability can be designed as passively safe. However, as core size increases, it becomes more difficult for SFRs to achieve passive safety as the coolant void reactivity feedback becomes more positive and the radial expansion feedback becomes less negative. The situation may be further exacerbated in designs with a high fraction of transuranic (TRU) actinides into the fuel, leading to small delayed neutron fractions and neutron lifetimes which accelerate transient progression. Therefore, avoiding or mitigating a positive coolant void feedback has been the focus of many studies as SFRs move towards commercialization.

Many methods for reducing the coolant void reactivity have been proposed in order to achieve passive safety [2]. Many of these are based on increasing neutron leakage. Examples of these methods include 'pancaking' the core so that it has a small height-to-diameter ratio and arranging fuel into highly heterogeneous configurations so that neutrons effectively leak from high reactivity fuel to nearby blanket material. While these methods have been effective in reducing the coolant void feedback, they inevitably lead to degraded core performance by worsening neutron economy and requiring higher fuel enrichments. In some cases, the penalties of leakage-based methods are high enough to eliminate the possibility for certain types of reactor missions, such as breed-and-burn (B&B).

Other studies have attempted to reduce the positive coolant void feedback through the addition of moderating material. Similar to leakage-based methods, these moderation-based methods are generally undesirable because many of the benefits of the fast spectrum, such as the ability to transmute waste and breed fissile material, are degraded under softer spectra. Therefore, reducing the coolant void feedback by softening the spectrum is often in direct competition with the reactor mission.

To avoid the drawbacks of both leakage- and moderation-based methods, numerous methods have been proposed that do not directly reduce the coolant void feedback, but rather attempt to compensate by adding a new engineered system. Examples of this include the Gas Expansion Modules (GEMs) tested in FFTF [2], control rods actuated by the Curie point tested in JOYO [3], and systems that enhance the control rod driveline feedback mechanism [4]. While multiple of these have proven effective, they suffer from certain limitations. For instance, GEMs only actuate in response to a reduction in core flow, and thus do not enhance the performance of transients in which flow remains unchanged. In the case of Curie point and other related systems, their actuations are irreversible such that a complicated procedure must be followed to un-actuate the system. These drawbacks have led to limited adoption in current SFR designs.

One engineered passive safety system that avoids the previously outlined issues is the Lithium Expansion Module (LEM) proposed by Kambe et al. [5]. In this system, a liquid column of lithium absorber is passively inserted and retracted from the core in response to changes in core temperature. Such a system allows for an easily reversible response to any initiating event without significantly impacting the neutron economy or spectrum. However, the system as originally proposed suffers from practical complications that would make it difficult to implement. The current project is based on a similar, but improved, version of the LEM, referred to as the Autonomous Reactivity Control (ARC) system. The ARC system was developed by Qvist et al. during work on a previous NEUP funded project (see for instance [6], [7]). The proposed system is autonomously actuated by a coolant temperature increase that passively induces thermal expansion of the ARC system working fluid that results in insertion of an absorbing liquid into the active core. It has a small penalty on the core neutron economy at standard operating conditions that can be greatly out-weighted by its ability to reduce core leakage, and its effect is reversible.

The objective of this project is to rigorously analyze the ARC system from a wide range of perspectives to determine its suitability for implementation into SFRs of varying missions. The major thrust of this project is to study the feasibility of the ARC system to improve transient performance. Once the expected

performance of the ARC system is confirmed, the project will proceed to assess the feasibility of using the ARC system to improve the neutron economy and, thereby, the performance of sodium cooled fast reactors. Due to limited funding being offered, this feasibility study focuses on numerical simulations. Experimental validation and engineering feasibility study will be proposed as a follow up study if justified by this study's conclusions.

2 ARC System Principles

2.1 Basic Design and Response Sequence

The ARC system in its standard configuration is installed as a modification to a conventional SFR fuel assembly design, as shown in Figure 1. The components relating to the ARC (upper and lower reservoir and tubes) are in approximate scale to one another, while the midsections of the assembly (that contains the fuel bundle) have been reduced in axial length by about a factor of 10 compared to the ARC-components for greater clarity. The system consists of two reservoirs, located at the top and bottom of the assembly, and two concentric tubes that link the reservoirs. The inner tube is open at both ends and connects the insides of both reservoirs, while the outer tube is open at the bottom (connected to the lower reservoir) and at the top connects to a closed gas-filled reservoir. During operation, the upper reservoir is completely filled with a liquid (henceforth the "expansion" liquid), while the lower reservoir contains the same expansion liquid and, floating on top of it, a separate immiscible liquid (henceforth the "absorber" liquid). The remaining free volume between the two concentric tubes in the closed system is filled with an inert gas. The outer ARC-tube has the same outer dimension as the fuel rods. Installing an ARC-tube therefore implies replacing one of the fuel rods in the assembly. More realistic drawings of the system reservoirs are given in Figures 2-3.

During an accident/transient scenario in the reactor, the ARC system responds in the following way:

1. Some event raises the temperature in the core, which heats up the coolant.
2. The heated coolant flows to the top of the assembly and transfers heat to the expansion liquid in the upper reservoir.
3. The expansion liquid in the upper reservoir thermally expands. Since the reservoir is completely filled and sealed at the top, this expansion is directed down the inner ARC-tube that connects the two reservoirs.
4. As expansion liquid enters the lower reservoir from the upper reservoir (through the inner ARC-tube), the level of absorber liquid rises into the active core, while compressing the inert gas above.
5. The absorber liquid, which has a high neutron capture cross-section, introduces negative reactivity by absorbing neutrons in the core, which in turn causes a reduction in power and temperature.
6. As the core cools down, the temperature of the expansion liquid starts to fall. Thermal contraction combined with the pressure of the inert gas again lowers the axial level of the absorber liquid until the system reaches a stable critical configuration.

A schematic view of how the liquid levels change in the lower ARC reservoir as the temperature increases is shown in Figure 4. Properly designed, the ARC-system can act as a thermostat in the core, autonomously controlling temperature without the need for any operator action, electrical systems, or moving mechanical parts. The actuation responds to temperature and relies solely on the laws of physics, and is therefore an inherent feedback mechanism.

2.2 Materials Selection

One of the most important aspects for the ARC system to function adequately is the proper selection of system fluids. Because the three fluids are in direct contact with each other, it is important to ensure that they remain properly stratified. This means that the fluids must be largely immiscible with each other and have the proper relative densities such that the absorber fluid sits on top of the expander fluid. Additionally, the fluids must have neutronic properties such that the absorber fluid can insert a strong enough negative reactivity while the expander fluid and inert gas are sufficiently neutronically

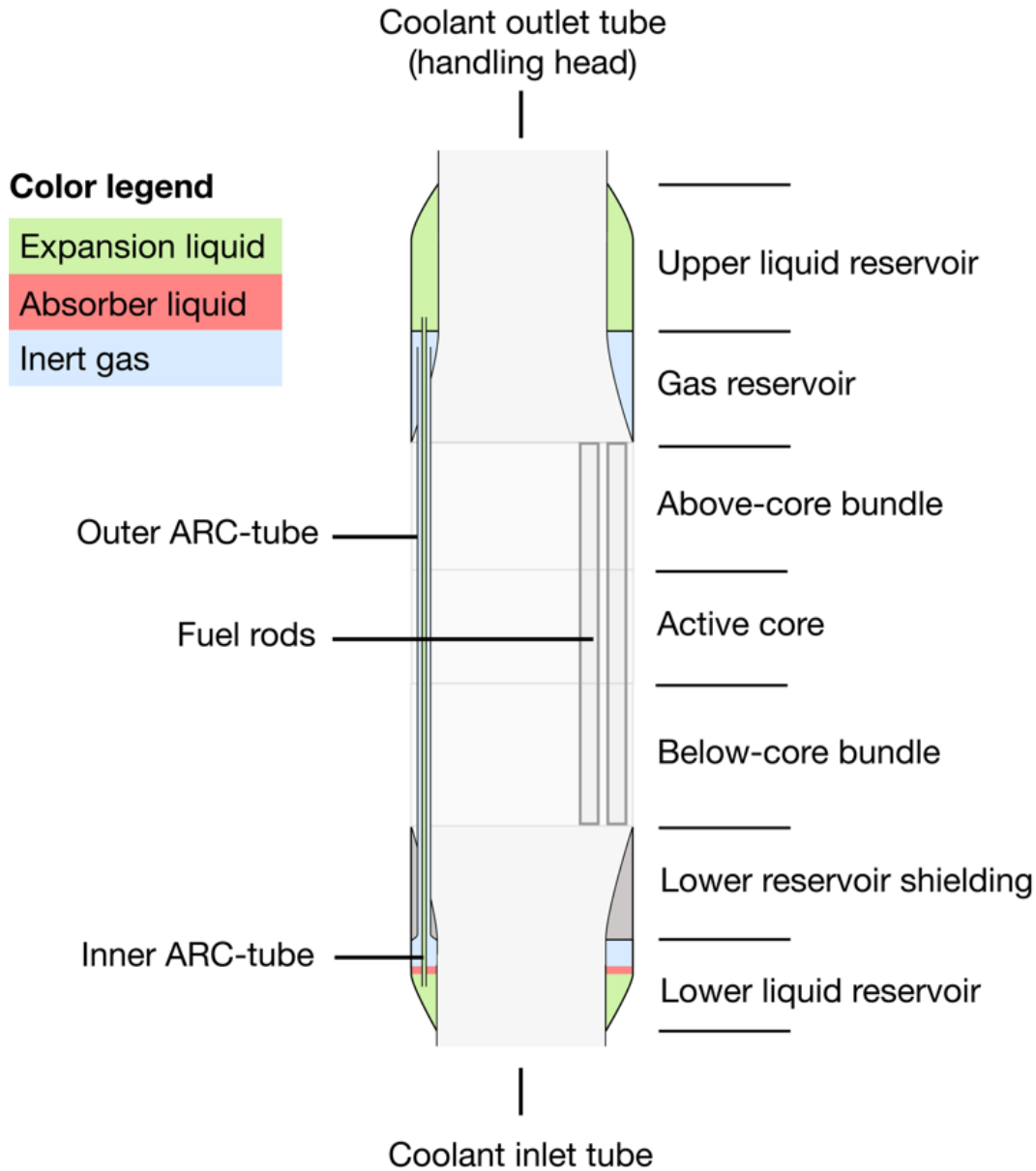

Figure 1: An ARC-equipped fuel assembly (not to scale).

inert. Finally, all fluids must be compatible with the structural material and must remain in the proper phase over the range of temperatures in both normal and off-normal operations. Taking into account these considerations, the recommended material selections are:

- **Expansion liquid**: Potassium, with potential alternatives Indium, Caesium, or Rubidium
- **Absorber liquid**: Lithium
- **Inert gas**: Helium, or alternatively Argon
- **Structural material**: Same as cladding and/or duct (HT9, T91, D9, etc.)

In this section, additional considerations are discussed and a review of the available and needed material data for the chosen materials is performed.

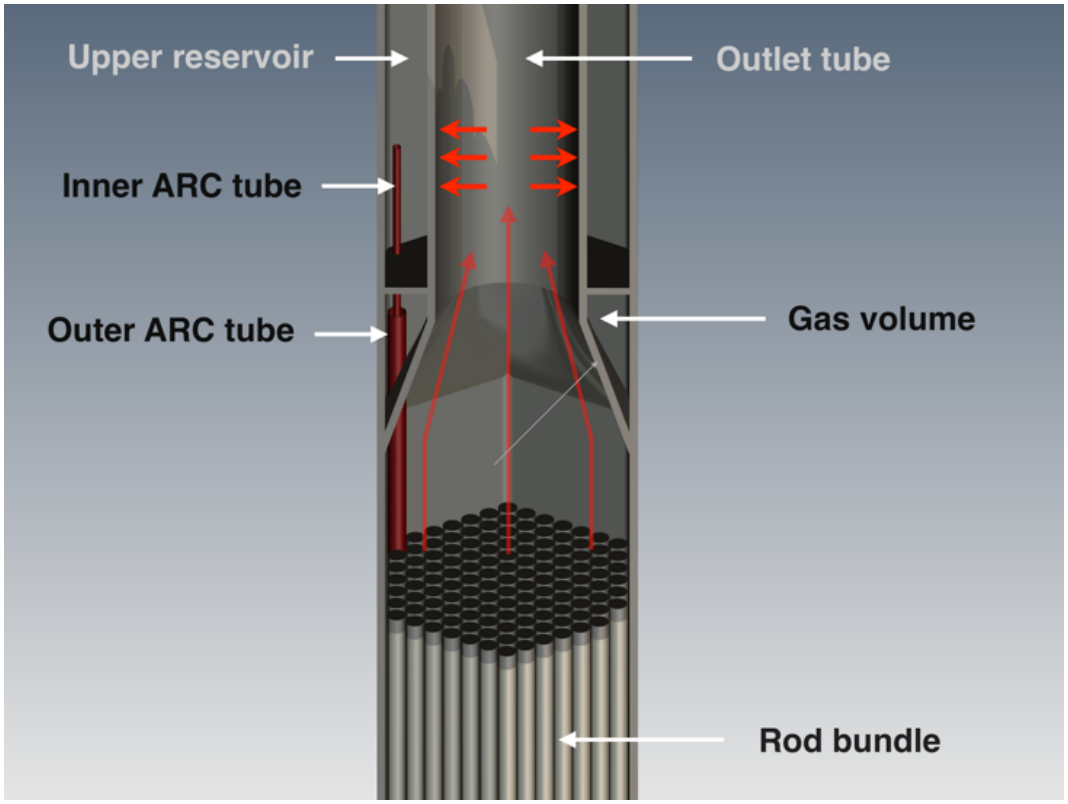

Figure 2: CAD model of the top of an ARC-equipped fuel assembly.

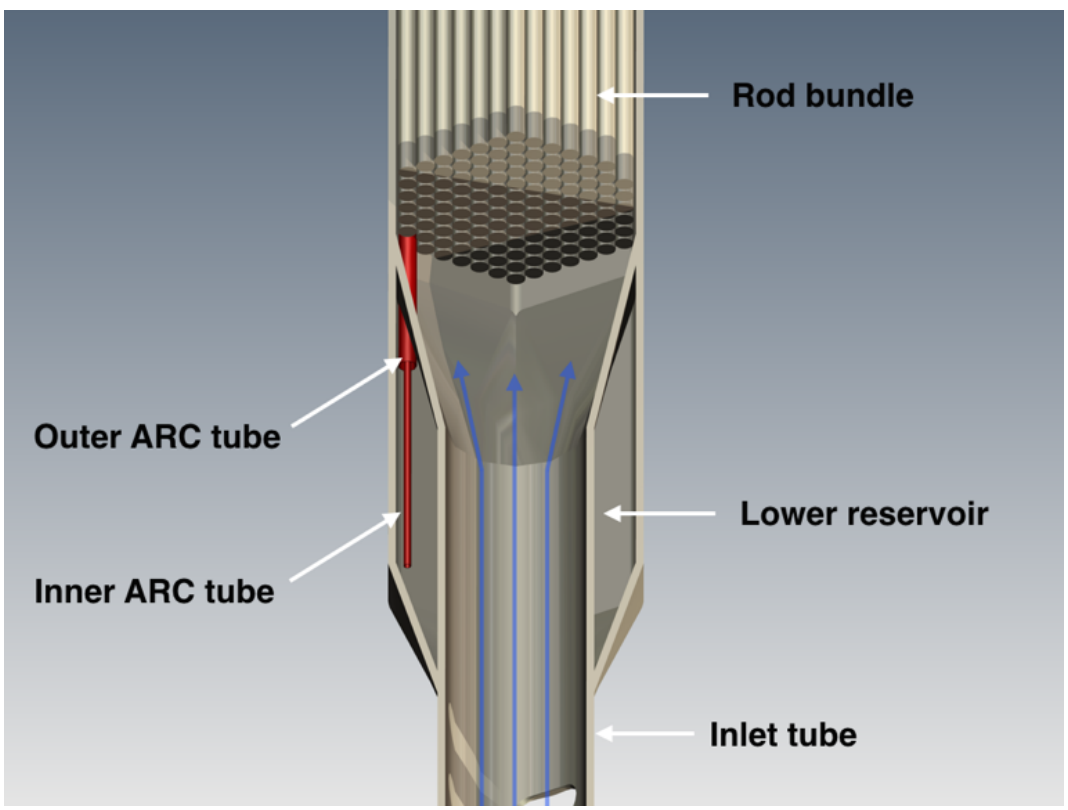

Figure 3: CAD model of the bottom part of an ARC-equipped fuel assembly.

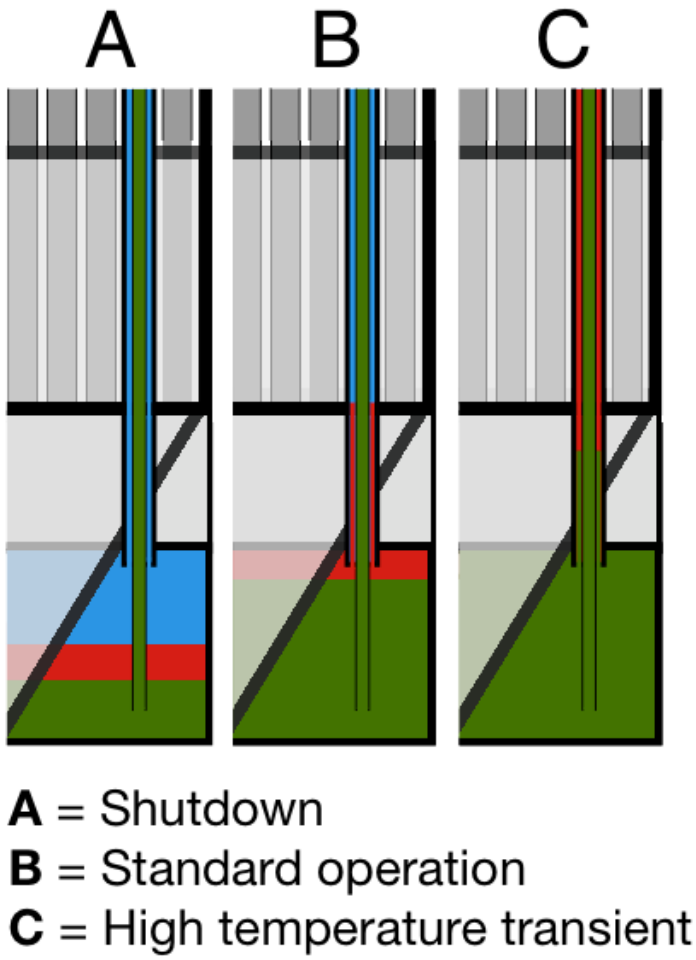

Figure 4: Schematic view of the lower ARC reservoir at different states. Green, red, and blue are the expander, absorber, and inert fluids, respectively.

2.2.1 The mutual solubility of potassium and lithium

In 1939, Bohm and Klemm found using thermal analysis that lithium and potassium do not alloy and there are neither intermetallic compounds nor solid solutions in the Li-K system [8]. Two published data sets for the mutual liquid solubility of lithium and potassium exists: that of Dotson and Hand and that of Smith, both outlined by Bale [9].

The data of Smith were obtained by equilibrating 15 g of lithium with 75 g of potassium in a molybdenum crucible held in an inert atmosphere. The lithium had been purified by treating it with zirconium in a tin crucible at 800°C for more than 100 h. The potassium had been vacuum distilled at 250°C. Although complete impurity levels were not reported, chemical analyses showed the lithium and potassium to have oxygen concentrations of 62 and 51 ppm, respectively. The results of Smith were not tabulated, but the paper gives the following correlations (here rewritten from their original base-10 logarithmic form and temperature converted to Celsius) as a fit to the data:

$$S_{Li\rightarrow K}\ [wt.ppm] = \exp(14.022 - \frac{4229.9}{T+273}) \quad 63 < T < 500°C \tag{1}$$

$$S_{K\rightarrow Li}\ [wt.ppm] = \exp(12.664 - \frac{3136.1}{T+273}) \quad 181 < T < 600°C \tag{2}$$

In atom fraction units, the solubility of lithium in potassium is always larger than the solubility of potassium in lithium. According to Bale, Equations 1 and 2 can be re-written to represent atom fractions instead as:

$$S_{Li\rightarrow K}\ [at.\%] = 691.86\exp(\frac{-4229.9}{T+273}) \quad 63 < T < 500°C \tag{3}$$

$$S_{K\rightarrow Li}\ [at.\%] = 5.62\exp(\frac{-3136.1}{T+273}) \quad 181 < T < 600°C \tag{4}$$

The measurements of Dotson and Hand were made by equilibrating 377 g of potassium with 274 g of lithium in a 304SS-type container maintained in an inert atmosphere. The metals had been purified by filtration, hot trapping, and vacuum distillation. A complete chemical analysis revealed a total impurity content of less than 500 wt.ppm, including 31 and 6 ppm of oxygen in the lithium and potassium metals, respectively. According to Bale, the results were in fair agreement with the unpublished data at 540°C by Tepper at the Mine Safety Appliance Research Company.

The lithium in potassium data from Smith agrees reasonably well with the data of Dotson and Hand (in which there are only three data points for Li in K) for temperatures from 427°C up to 538°C. Unfortunately, no published experimental data has been found for the solubility of lithium in potassium above 538°C. For potassium in lithium, the data is more scattered, and Equation 2 based on the data from Smith poorly represents some of the data of Dotson and Hand. At 538°C the two sources agree with a relative difference of less than 6%, while at 666°C the difference is more than a factor of 2.

In 2006, Zhang modeled the K-Li system using the CALPHAD approach as a part of a doctoral dissertation [10], and the resulting phase diagram along with the data of Smith is shown in Figure 5.

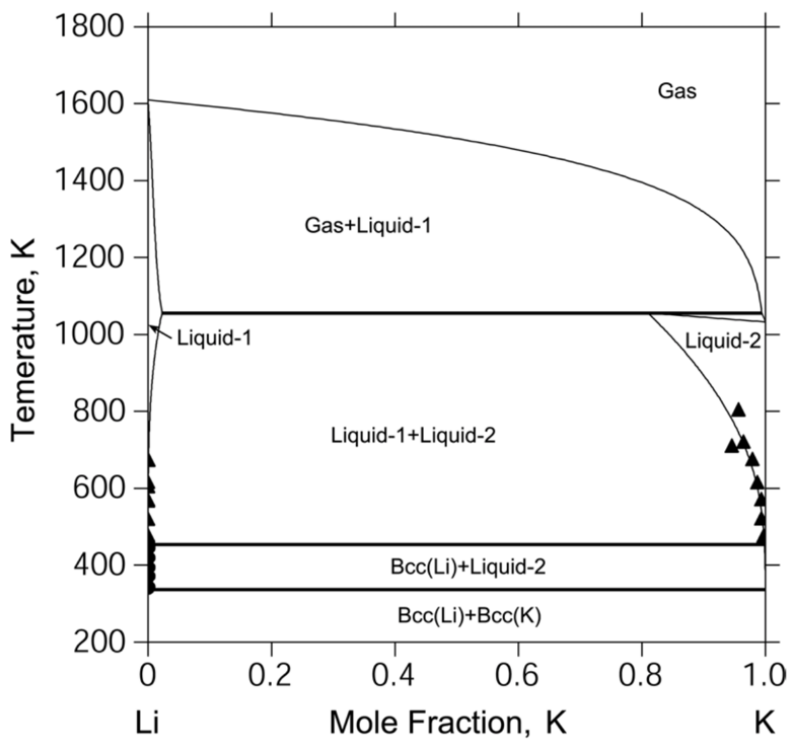

Figure 5: The K-Li phase diagram as calculated by Zhang.

It is clear that more extensive experimental data on the K-Li system to higher temperatures is required. However, based on the available data and simulations, a few conclusions can be drawn:

- The two liquids are expected to remain essentially immiscible throughout their respective liquid temperature ranges, with their relative mixing peaking at the boiling temperature of potassium
- The atomic fraction of potassium in lithium remains below 1% up to 700°C
- The risk for loss of lithium into potassium accelerates at temperatures above about 550°C

Coolant inlet temperatures seen in liquid metal cooled reactor designs are typically in the range from 250°C (in lead-bismuth eutectic (LBE) cooled designs) up to a maximum of about 420°C (in certain lead-cooled designs). Sodium-cooled reactors are typically designed for a coolant inlet temperature in the span 350-395°C. Since the temperature of the lower ARC reservoir is identical to the coolant inlet temperature at all times except for during a transient, the lithium and potassium in the lower reservoir will mix approximately according to Equations 1 and 2.

As temperatures rise, the problem of mixing in the liquids rapidly becomes increasingly severe. At a temperature of 700°C, which is a reasonable peak allowable temperature during a transient, the correlations, while technically not valid at this temperature, indicate that the liquids may mix by several weight percent. Fortunately, this rapid increase in solubility is not a big concern to the operation of the ARC system:

- Once the system is actuated, the interfacial area between the two liquids is miniscule (the annulus area between the ARC-tubes), making the mixing process at high temperatures very slow. Even with a large area for the liquids to interface, it typically takes several hours to reach equilibrium.
- The location where the two liquids interface remains below the active core during all transients. Therefore, the temperature at the interface will be more closely correlated to the coolant inlet temperature.
- It is only in the unprotected loss of heat sink (ULOHS) transient event that we see elevated coolant inlet temperatures for an extended period of time.
- As temperatures go back down following a transient, the solubilities fall back as well, causing the two liquids to de-mix.

The practical issues which may arise from Li-K mixing, including the loss of lithium, tritium production, and a neutronic penalty, are addressed in Section 9.

While it appears that pure lithium and pure potassium will function as ARC liquids as required, it may be preferential to identify and introduce impurities or alloying materials to both liquids that will cause the bulk liquids to maintain complete immiscibility throughout the liquid temperature range. Regardless, an extension of the available experimental data for mutual solubility up to at least 700°C will be required.

2.2.2 Properties of ARC materials

For the properties of liquid lithium, the main references are three reports: (1) Davison [11], which contains a literature review and nearly all the relevant correlations, (2) Jeppson, Ballif, Yuan and Chou [12], which covers chemical interactions and corrosion, and (3) Alcock, Chase and Itkin [13], which gives an extensive review of heat capacity data for all alkaline metals. The thermophysical data for potassium is primarily collected from The Sodium-NaK Engineering Handbook [14], which contains extensive information on all relevant properties of potassium. The coolant outlet tube should be made from the same material as the fuel assembly duct to minimize stress. While this may in principle be any fast reactor steel, in this analysis we have used the material properties of the low-swelling ferritic-martensitic steel HT9. The references for HT9 thermophysical properties are: (1) Leibowitz and Blomquist [15], (2) Yamanouchi, Tamura, Hayakawa, and Kondo [16], and (3) The Nuclear Systems Materials Handbook by the Hanford Engineering Development Laboratory (HEDL).

The melting temperature of pure liquid lithium as recommended by Jeppson, Ballif, Yuan, and Chou is:

$$T_{m,Li}\ [^\circ C] = 180.54 \tag{5}$$

The recommended density correlation for liquid lithium, based on a fit to data from several references in Davison, is:

$$\rho_{Li}\ [kg/m^3] = 562 - 0.1T \quad T(K) < T_{m,Li} \tag{6}$$

For the heat capacity of liquid lithium, there are significant differences between sources. Davison tries to resolve this by assigning a constant value, while the extensive review work by Alcock et al. specifically recommends the correlation of Douglas, Epstein, Dever, and Howland. In our modeling, we follow this recommendation, defined as:

$$C_{p,Li}\ [J/kg/K] = 4759.4 - 0.838T \quad T_{m,Li} < T < 700K \tag{7}$$

$$C_{p,Li}\ [J/kg/K] = 4227.3 - 0.072T \quad 700 < T < 1600K \tag{8}$$

The correlation for thermal conductivity used is that presented in the Handbook of Thermodynamic and Transport Properties of Alkali Metals [17]:

$$k_{Li}\ [W/m/K] = 22.28 - 0.05T - 1.243 \times 10^{-5}T^2 \quad 455 < T < 1500K \tag{9}$$

The correlation for vapor pressure used is that recommended by Davison:

$$P_{Li}\ [Pa] = \exp(23.06 - \frac{18569.2}{T}) \quad 800 < T < 1800K \tag{10}$$

The boiling temperature of lithium is thus given as:

$$T_{b,Li}\ [K] = \frac{18569.2}{23.06 - \ln(P[Pa])} \tag{11}$$

Finally, all types of steel used in fast reactors are corrosion resistant to static liquid lithium at relevant temperatures as seen in the lower reservoir (300-400°C) [12].

The melting temperature of potassium is:

$$T_{m,K} = 63.6[^\circ C] \tag{12}$$

The density of liquid potassium is:

$$\rho_K\ [g/cm^3] = 0.8415 - 2.172 \times 10^{-4}T - 2.70 \times 10^{-8}T^2 + 4.77 \times 10^{-12}T^3 \quad T_{m,K} < T < 1250^\circ C \tag{13}$$

The heat capacity of liquid potassium is:

$$C_{p,K}\ [J/kg/K] = 838.47 - 0.3672T + 4.5899 \times 10^{-4}T^2 \quad T_{m,K} < T < 1150^\circ C \tag{14}$$

The vapor pressure for liquid potassium is given by Bowles [18]:

$$P_K\ [Pa] = 0.1013 \exp(\frac{17.843T - 11081 - 1.026T\ln(T)}{T}) \tag{15}$$

The boiling temperature of potassium is:

$$T_{b,K}\ [K] = 586.1P[MPa]^{0.3289} + 764.1 \tag{16}$$

The liquid potassium thermal conductivity can be well represented by the following correlation:

$$k_K\ [J/m/K] = 56.16\exp(-7.958 \times 10{-}4T) \quad 100 < T < 900^{\circ}C \tag{17}$$

A curve-fit was made from the data points of HT9 density measurements from the Materials Handbook for Fusion Energy Systems. An excellent fit to the density data is obtained by the following correlation:

$$\rho_{HT9}\ [kg/m^3] = 7824 - 9.288 \times 10^{-5}T - 0.1859T^2 \quad 298 < T < 923K \tag{18}$$

The thermal conductivity and specific heat is given by:

$$k_{HT9}\ [W/m/K] = 17.622 + 2.42 \times 10^{-2}T - 1.696 \times 10^{-5}T^2 \quad T < 1030K \tag{19}$$

$$k_{HT9}\ [W/m/K] = 12.027 + 1.218 \times 10^{-2}T \quad T \geq 1030K \tag{20}$$

$$C_{p,HT9}\ [J/kg/K] = \frac{T - 600}{6} + 500 \quad T < 800K \tag{21}$$

$$C_{p,HT9}\ [J/kg/K] = 3\frac{T - 600}{5} + 550 \quad T \geq 800K \tag{22}$$

With sufficiently low oxygen concentration, steel corrosion rates due to exposure to the static potassium appears to be completely negligible at all relevant temperatures of the system [19] [20].

3 ARC System Manufacturing Process

In order to ensure that the ARC system can be manufactured in practice, the manufacturing and assembly processes were devised. The components and assembly steps for the ARC system were developed for the more advanced design with an annular upper reservoir (outlined later in Section 4), since this design options shows more promise.

3.1 Components and Configuration

The ARC system design requires some changes to the conventional fuel assembly manufacturing procedure. The added difficulty stems primarily from the fact that the outer ARC tube needs to be attached to both the ARC reservoirs and the length and attachment of this tube is different from that of the rest of the fuel rods.

Rods in a typical fuel assembly are attached to, and stand on, pin mounting rails. The mounting rails are thin sheets with an enlarged upper edge that span from one side of the assembly to the other. Key-hole slots in the lower end plugs of the fuel rods slide onto the rails and are trapped by a bulging upper rail edge in the upper end enlargement of the key-hole slot. The mounting rails are positioned by rail pins that pass through the lower area of the rails (below the keyhole). The rail pins pass through the nosepiece at each end, which positions the rails with respect to the nosepiece to prevent axial motion. An ARC-equipped assembly requires a modified mounting rail and rail pin structure that omits one or more of the rod positions, depending on the number of ARC-tubes used.

To assemble the ARC-type design, the components of the assembly are subdivided into the following pieces, which are assembled individually:

- The nose piece, which contains the lower ARC reservoir and the complete outer ARC-tube (pre-welded to the lower reservoir). The lower ARC reservoir contains, in solid state, the appropriate amount of absorber and expansion materials.
- The pin mounting rail grid for the rod bundle, with a slightly modified arrangement to allow for one or more ARC-tubes to pass through.
- Stabilization bars (at least 4) that support the mounting grid.
- The fuel rod bundle, missing one or more pins to make room for the ARC tube(s).
- The ARC upper gas reservoir piece, with an opening in the bottom allowing for the outer ARC-tube to enter (and be welded on). The gas reservoir piece is open at the top.
- The upper ARC liquid reservoir, which is fully enclosed (its bottom surface forms the top surface of the gas reservoir below) with the full-length inner ARC tube pre-welded on. The upper ARC reservoir is completely filled with ARC expansion material (in solid state), and has fins spreading out in two for positioning with the duct.
- A “lower duct” piece, long enough to go from the nose-piece to connecting with the fins of the upper liquid reservoir.
- The remaining “upper duct” section (covering the region of the upper ARC-reservoir) and handling socket.

The pieces are shown in axial order from the bottom in Figures 6-16, with welds (pre-made before assembly of the separate pieces) marked in red. The stabilization bars, which are simple steel cylinders, are not shown separately.

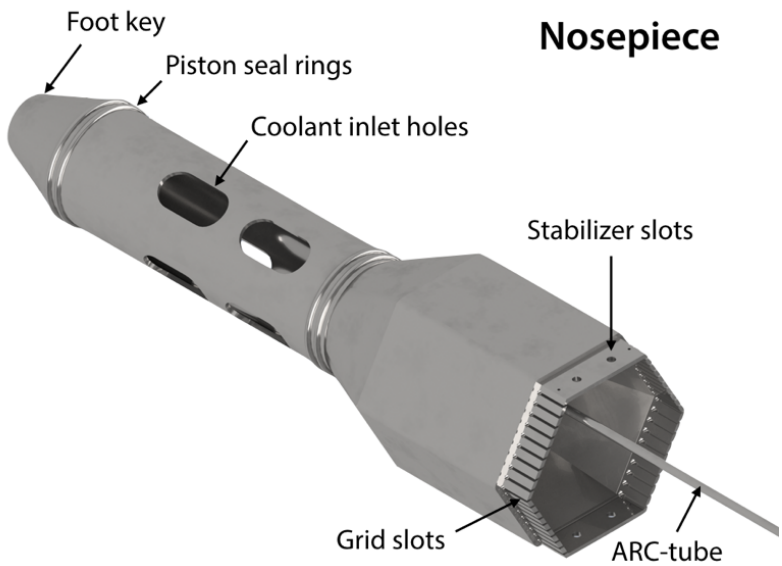

Figure 6: Nosepiece of ARC-equipped assembly.

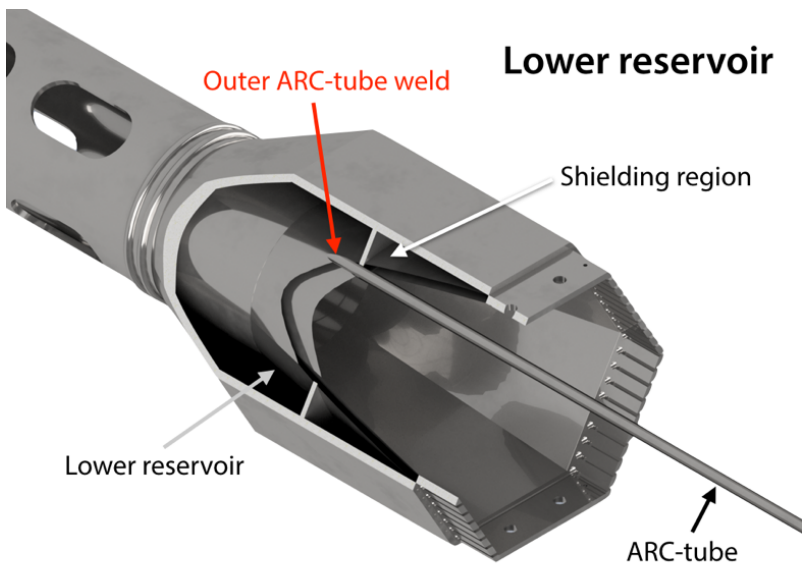

Figure 7: Cut-through view of the upper part of the nosepiece, showing the lower reservoir and its shielding region as well as the attachment of the outer ARC-tube.

3.2 Assembly Process

The assembling steps for an assembly of this type are:

1. The mounting rails pins are inserted into their slots in the nose piece and the stabilization rods are inserted in their slots through both the pin mounting rails and the nose piece.
2. The bottom end of the lower duct piece is welded to the nosepiece.
3. The open gas reservoir piece is welded onto the outer ARC tube.
4. The lower duct section is welded on the nose piece.

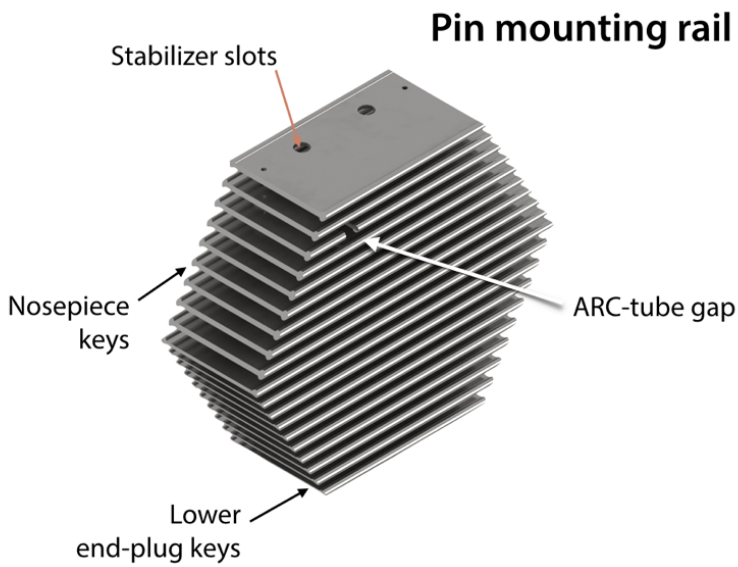

Figure 8: The pin mounting rail, modified to accomodate more stabilization rods (4 in total) and a single ARC-tube.

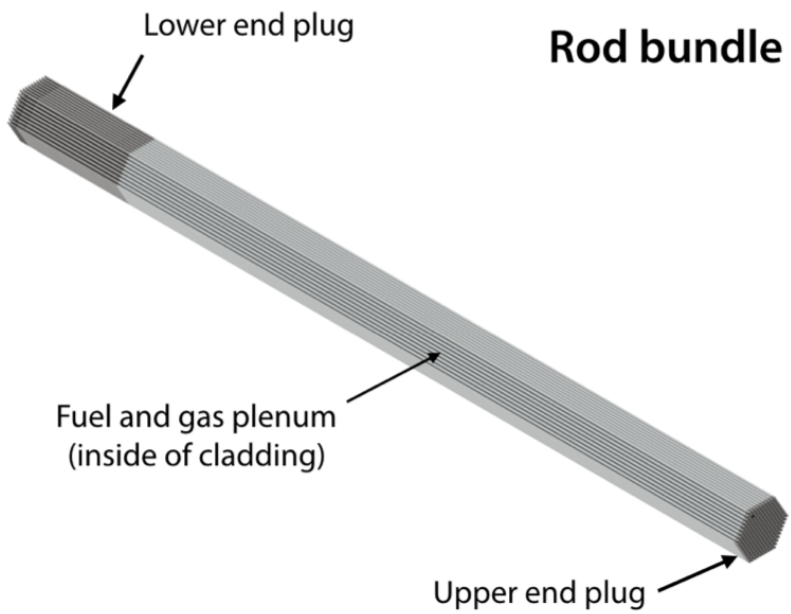

Figure 9: The rod bundle consists of the lower end plug, cladding, fuel (inside the cladding) and upper end plug, and wires wrapped around the rods for spacing.

5. The liquid reservoir piece is positioned on top of the gas reservoir piece and slid into its positioning slots in the duct. The inner ARC tube which is pre-welded to the liquid reservoir is inserted into the outer ARC tube through the gas reservoir. The liquid reservoir piece is then welded on (outside and inside) to the gas reservoir piece.

6. Finally, the upper duct piece and handling head piece is welded to the lower duct piece.

The assembling steps are shown in Figures 17-22 with welds (made during the assembly of the separate pieces) marked in red. A view of all components assembled (with the ducts and handling head transparent)

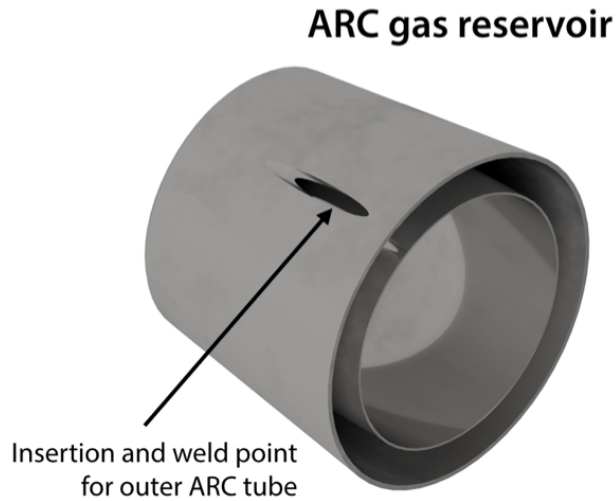

Figure 10: The upper gas reservoir is open at the top and closed at the bottom, and includes a hole through which the outer ARC tube is mounted and welded.

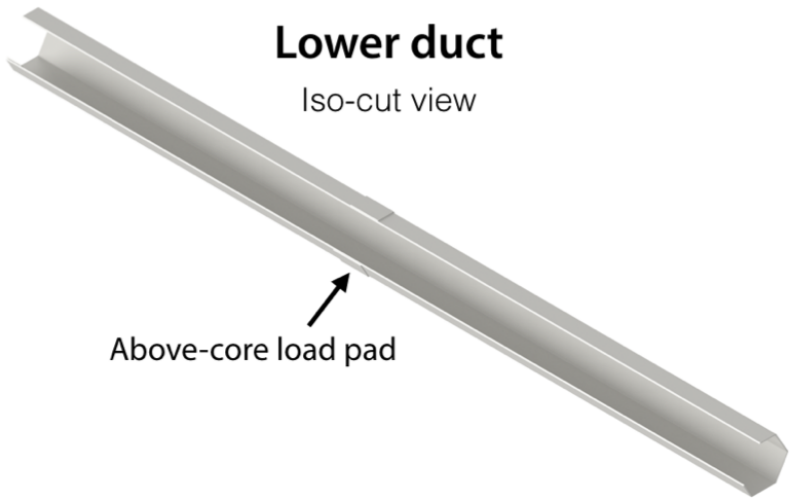

Figure 11: Isometric cut-through view of the hexagonal duct section.

is shown in Figure 23. The most challenging step is the inner edge weld between the gas reservoir and the upper liquid reservoir. This may present a challenge to the welder if the coolant outlet tube diameter is relatively small and the gas and liquid reservoirs are long. All the other operations can be carried out using only slightly modified fuel assembly manufacturing equipment. The reservoir connection and positioning piece installed in the duct allows the reservoirs to travel axially, thus reducing the risk of breaking the outer ARC tube from thermal stress as its temperature changes.

3.3 Summary of Findings

The evaluation performed in this section has outlined the method for manufacturing and assembling ARC systems to fit into standard SFR assemblies. It has been found that ARC systems may be included without unreasonable modifications to the standard SFR assembly design, and it is envisioned that the modified assemblies may be manufactured using the same general equipment and processes. The most difficult additional aspect is likely to be the incorporation of a number of welds which must be made during the assembly process, although these should be able to be accommodated. Therefore, additional complications in the assembly process are not viewed as a significant barrier to ARC system utilization.

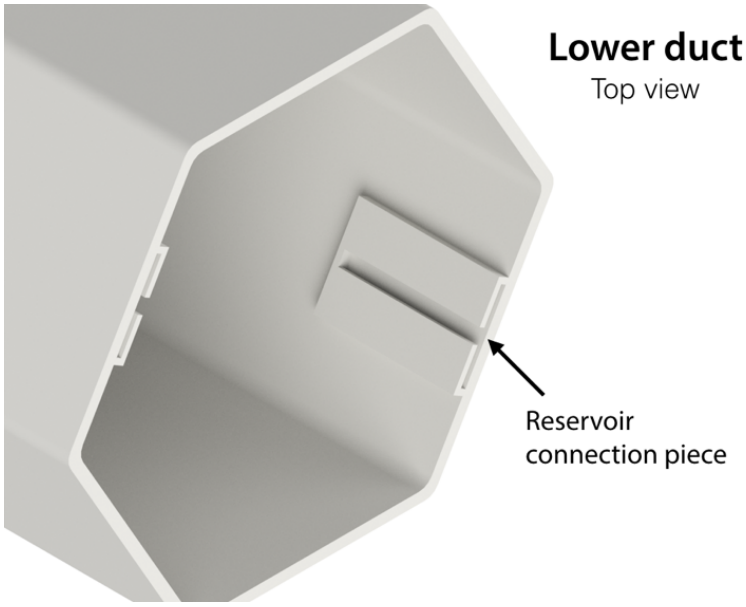

Figure 12: At the top of the lower duct section, there are two reservoir positioning slots on opposite sides, in to which the slits attached to the upper liquid reservoirs are inserted from above.

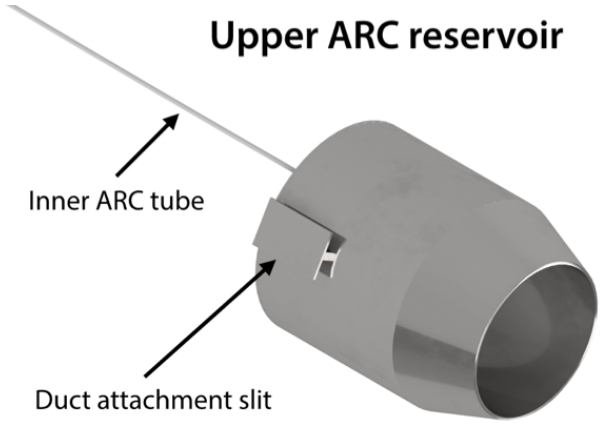

Figure 13: The upper ARC (liquid) reservoir is located on top of the gas reservoir. It has two duct-attachment slits protuding from its sides, and the inner ARC tube is welded through the bottom surface.

4 High-fidelity ARC System Characterization

The response of the ARC system is dependent on heat transfer from the flowing coolant to the expander fluid contained in the upper reservoir (UR). The speed of this heat transfer process can have important implications on the outcome of a given transient, and as such it is necessary to accurately quantify the behavior of the ARC system in response to a change in coolant temperature before performing whole-core transient calculations. By using high-fidelity Computational Fluid Dynamics (CFD) calculations, the details of the response can be fully understood, and the essential behavior may be simplified to a model more appropriate for whole-core simulations. In addition, high-fidelity models that account for all of the physics allow for accurate design optimizations to be performed so that the ARC system may be designed to best improve performance. This section outlines the high-fidelity simulations performed to quantify and optimize the response of the upper reservoir through geometric design changes. All simulations are performed using the COMSOL Multiphysics finite element software.

The key quantifications made are the pressure drop induced by the upper reservoir and the time that

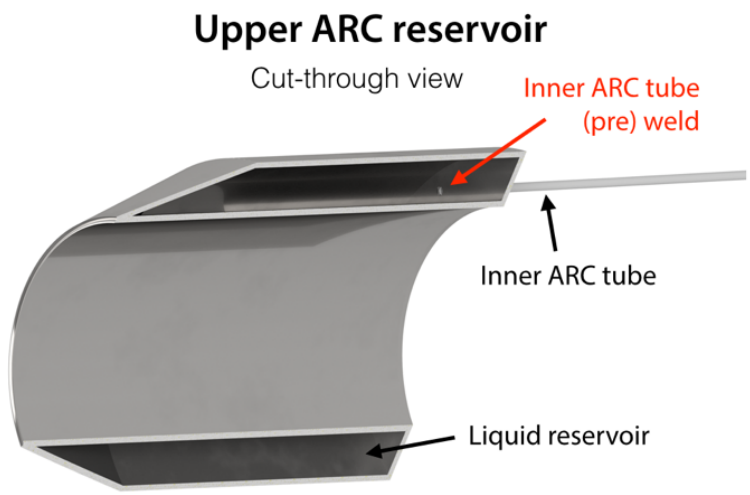

Figure 14: Cut-through view of the upper ARC (liquid) reservoir showing the attachment of the inner ARC tube.

Figure 15: Isometric view of the upper duct section and handling head.

it takes for the upper reservoir to heat up in response to a change in coolant temperature. This heat up time is quantified as a time lag parameter, τ, which is later used in the whole-core transient studies. τ is the amount of time it takes for the upper reservoir to heat up to 63% of the driving temperature as defined by the following equation:

$$T_{UR}(t) = T_{coolant} + (T_{UR}(0) - T_{coolant}) \exp(-\frac{t}{\tau}) \tag{23}$$

An alternative definition sometimes used in this study is the amount of time it takes for the upper reservoir to heat up to 90% of the driving temperature. The use of either definition is acceptable when

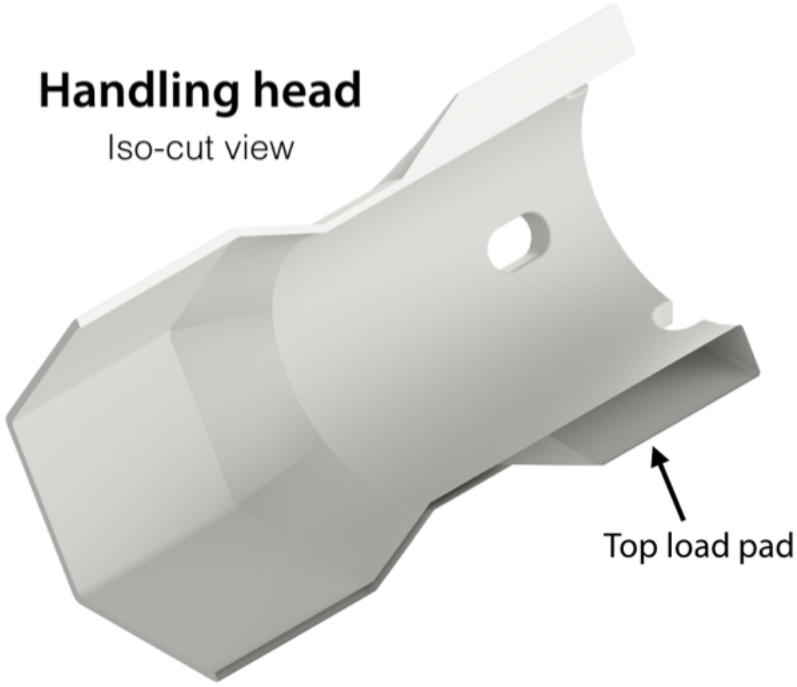

Figure 16: Cut-through iso-view of the upper duct section and handling head. The thicker uppermost section of the handling head extends beyond the outer limit of the duct to form the top load pad.

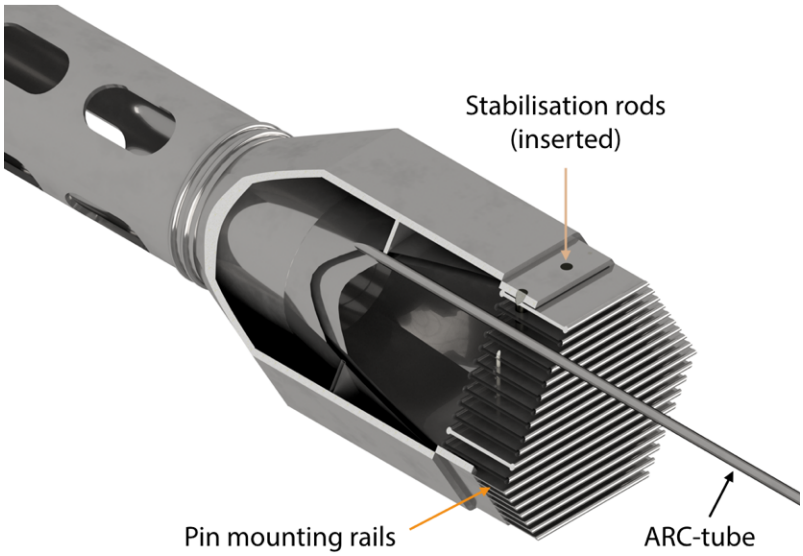

Figure 17: Step #1, The pin mounting rails and stabilization bars are inserted in to their respective slots in the nose piece.

comparing the performance between UR designs, as long as a consistent definition is used.

4.1 Design Constraints

Design of the ARC system is flexible, however a range of criteria need to be met. The target criteria in this study are:

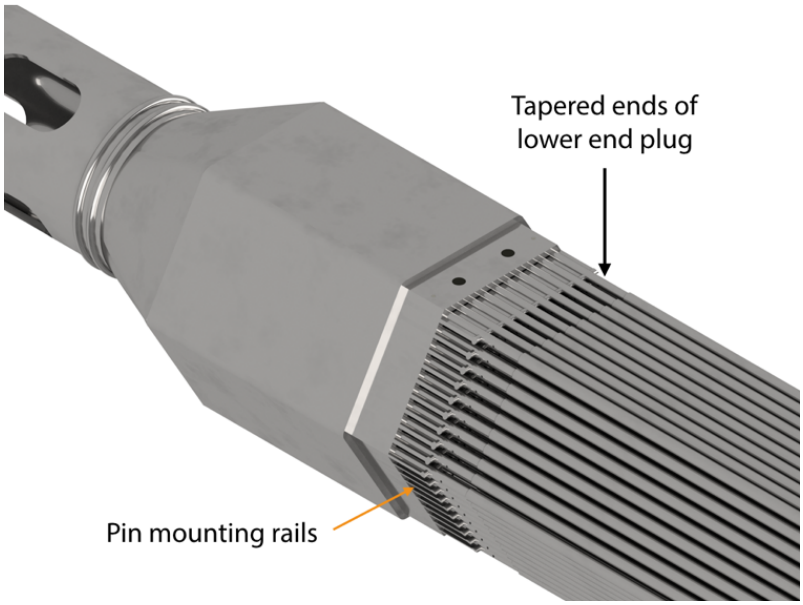

Figure 18: Step #2, The rod bundle (containing the pre-fabricated complete fuel rods and wire-wraps) is slid on to the pin mounting rails.

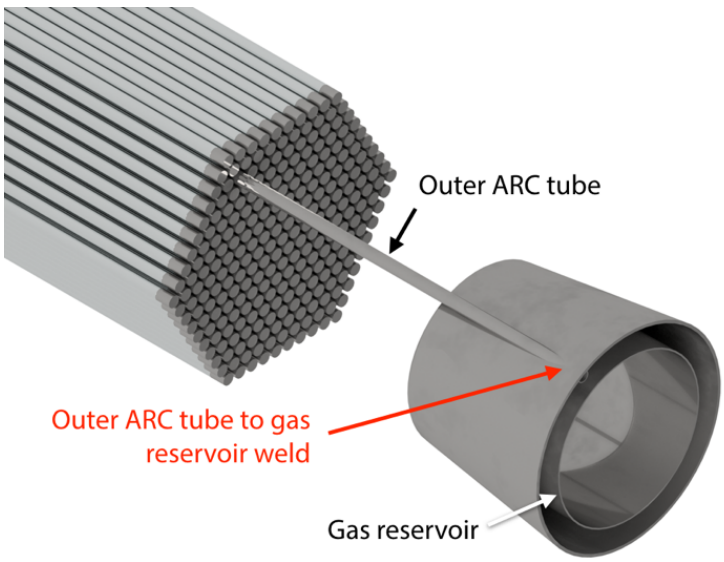

Figure 19: Step #3, The gas reservoir is welded to the outer ARC tube.

- The UR must contain approximately 0.5 - 1 liter of potassium.
- The UR, independent of shape, needs to be wide enough to enable connection of the UR to the lower reservoir (LR) via two concentric tubes. Practical value of thickness should be not smaller than 1 cm.
- The shape of the UR must permit installation of the tubes in straight line from UR to LR and in a location that corresponds to the fuel pin array.

Other goals regarded as soft constraints are:

- ARC introduces less than 10% of the total pressure drop

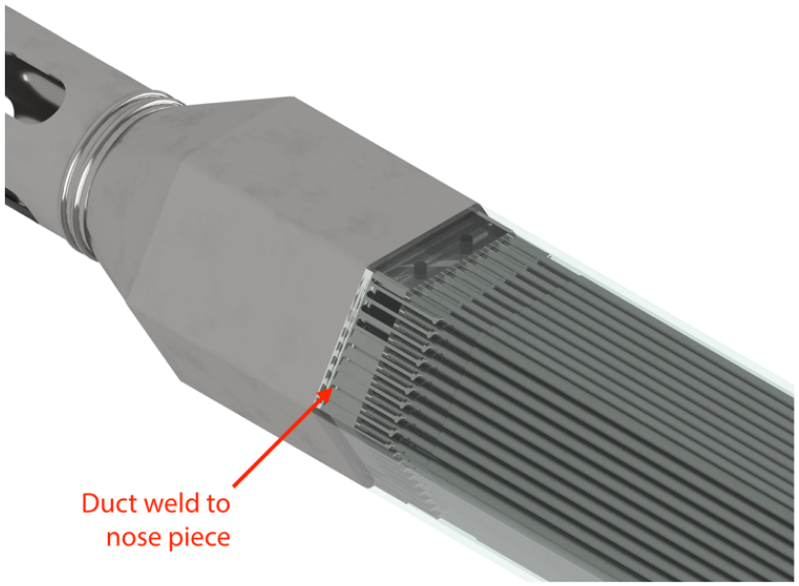

Figure 20: Step #4, The lower section of the duct is welded to the nose-piece.

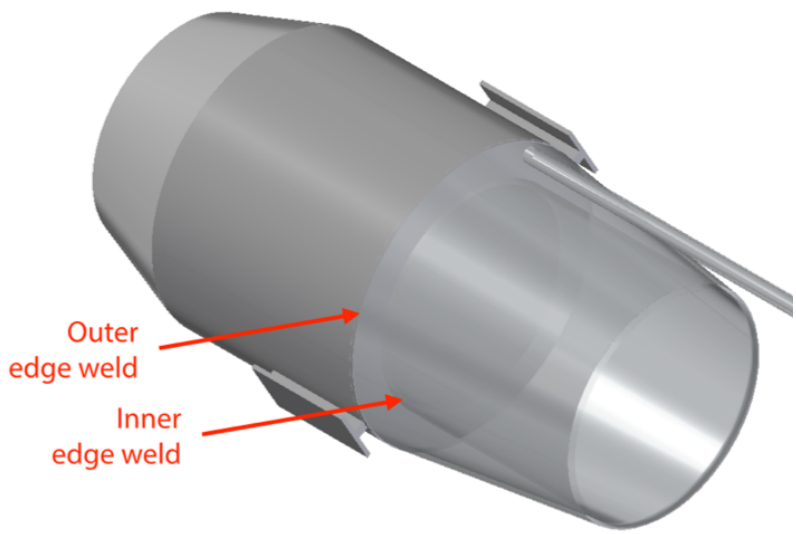

Figure 21: Step #5, The upper liquid is positioned on top of the gas reservoir, with the inner ARC tube inserted in to the outer ARC tub and the positioning fins inserted in to the duct slots. The liquid reservoir is welded on to the gas reservoir at the inner and outer edges.

- ARC causes less than 10% increase in the length of the fuel assembly
- τ of less than 5 s, based at 100% of coolant mass flow

4.2 Geometry and Numerical Modeling

Considering the functionality of the ARC system, it was established that an annular UR immersed in coolant flow will provide increased heat exchange area, in comparison to the original design in which the UR was placed at the outside of the fuel assembly (shown in Figure 2). This approach eliminates contraction of the top fuel assembly part, but in exchange the coolant flows around an annular UR placed in the center-top part of the assembly as shown in Figure 24.

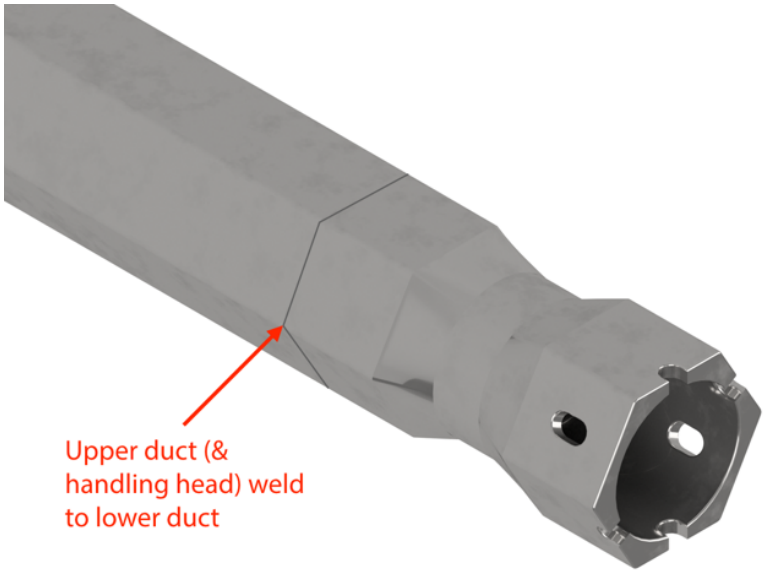

Figure 22: Step #6, The uppermost section, consisting of the upper duct section and the handling head, is welded on to the lower duct section.

Figure 23: Iso-view of final assembly (with transparent ducts and handling head).

The UR is installed in the fuel assembly using six vertical ribs, which extend from the top of the UR to the bottom of the potassium reservoir (but not along the gas reservoir). In this study the ribs are solid, although the ribs could be designed as hollow if crossflow is desired. The amount and thickness of the ribs has been selected using engineering judgment and may be reduced after carrying out stress analysis of the final design.

The solid model of includes only the UR (potassium volume, steel casing and steel ribs), part of the coolant flow, and the assembly shroud. The tubes connecting the UR and LR are not included in the model, but instead an outlet on the bottom wall of the UR is applied. The simulations are carried out in a transient mode to account for velocity instabilities that may occur as the flow attaches and detaches from the top of the UR. Additionally, symmetry is utilized so that only a half of the geometry was used for the simulations. In the conceptual ARC design, the gas reservoir (GR) is placed under the UR and is filled with inert gas that does not appreciably take part in the heat exchange (thermal conductivity of argon 0.02 W/m/K) and is therefore omitted from the simulation. The walls of the model are set to be

Figure 24: Example of the advanced UR design.

smooth with no-slip condition. The outer walls of the geometry are modeled as insulated, apart from the coolant inlet and outlets, which is valid as long as heat loss to the bypass flow or surrounding assemblies is not significant.

The simulation physics consists of two non-isothermal liquid flows and conjugate heat transfer through a solid. The primary sodium flow is upward through the top part of the fuel assembly, and is expected to be highly turbulent. A solid steel domain thermally couples both flows. The secondary flow is driven by natural convection, where temperature-based density differences trigger potassium flow in the upper reservoir. The boundary and initial conditions in the upper ARC reservoir and fuel assembly are summarized in Table 1.

Table 1: Initial and boundary conditions for the CFD simulations.

Parameter	Value	Units
Mass flow rate	52.28	kg/s
Initial temperature	510	°C
Temperature increase	50	°C
Coolant pressure	160	kPa
UR pressure	200	kPa

4.3 Results

The optimization efforts are carried out in stages. The aim of the first stage is to determine the relationship between height and thickness of the UR at a constant volume. Then, the volume of the UR is gradually

decreased from 1 to 0.5 L to determine if it is possible to achieve the desired expansion rate with a smaller amount of potassium. In the final stage, the geometry of the UR is modified to achieve an even lower pressure drop while preserving the rate of the heat exchange. The dimensions of parameters which were not changed during the optimization process are listed in Table 2.

Table 2: General dimensions of the ARC geometry consistent over the optimization efforts.

Parameter	Value	Units
Added assembly height	0.6	m
Assembly flat-to-flat	15	cm
Assembly shroud thickness	3	mm
UR steel thickness	2	mm
Coolant mixing volume length	30	cm

4.3.1 Geometry of Upper Reservoir at Constant Volume

The optimization efforts were first carried out at constant volume of 1 L to determine the relationship between the pressure drop and the rate of the heat exchange, both of which depend on the relationship between thickness and height of the UR. Table 3 lists design details of three geometries G1, G2 and G3, which occupy 26%, 31% and 40% of the X-Y cross-section area of the assembly, respectively.

Table 3: General dimensions of the ARC geometries considered in the constant-volume stage of the optimization.

Design Name	Dimension	Value	Unit
G1	D1	10.0	cm
	D2	6.0	cm
	H	25.0	cm
G2	D1	11.0	cm
	D2	6.6	cm
	H	20.0	cm
G3	D1	11.5	cm
	D2	5.8	cm
	H	15.0	cm

A consistency check of the results can be done by monitoring a variable of significance and checking for a stable solution. Oscillating values may indicate that a convergence has not been reached or that the setup needs to be modified. The variables selected for the consistency check were maximum velocity magnitude at the coolant outlet boundary and average pressure at the coolant inlet boundary. The maximum velocity magnitude and pressure are plotted against time in in Figures 25 and 26, respectively, for G2. Both variables converge to constant values, although the velocity magnitude converges at a slower rate with small velocity oscillations that are typical of flow around a blunt body.

The temperature field of G2 is plotted in Figure 27 in a Y-Z plane located at 1 cm offset from the Y-Z symmetry plane and at the surface of the UR for a range of time steps. The temperature in the UR reaches 555°C within 5 seconds.

Figure 28 shows the mass fraction of expander fluid in the upper reservoir as a function of time for the three different designs. In this context, a smaller mass fractions are better, as it indicates a faster system actuation. In comparison to both G1 and G3, the performance of G2 is superior. For all geometries, 1.65% of the potassium inventory was expelled from the upper reservoir.

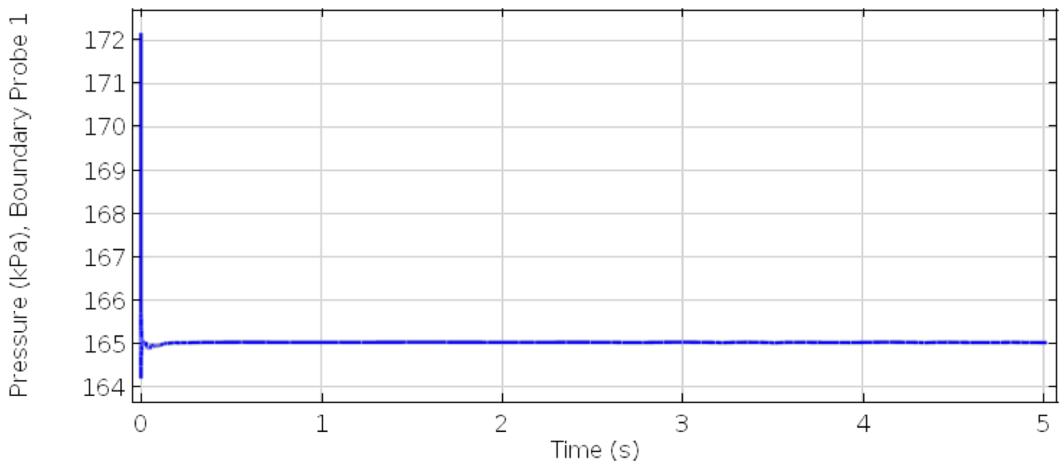

Figure 25: Monitor of the surface averaged pressure at the coolant inlet boundary.

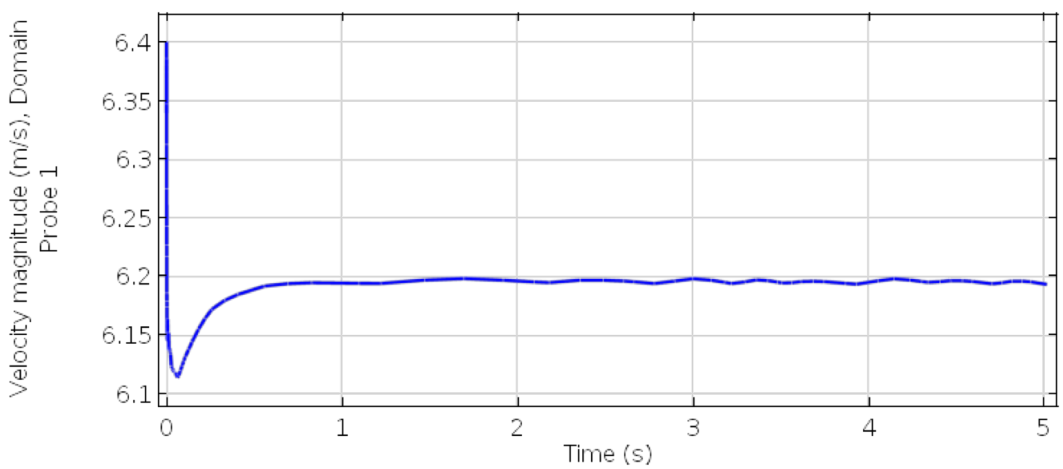

Figure 26: Monitor of the surface maximum velocity magnitude at the coolant outlet boundary.

Figure 29, shows a performance summary for geometries G1-G3. τ is smallest and largest for G2 and G3, respectively. The thinnest design, G1, resulted in the lowest pressure drop, with pressure drop increasing as the upper reservoir thickness increases. τ reaches a local minimum between geometries G1 and G3, where the competing effects of decreasing UR thickness and increasing steel volume fraction trade places as the dominant effect. Because G2 has the best combination of characteristics, it is selected for further optimization in the following study.

4.3.2 Reduced Volume Upper Reservoir

Three geometries were compared to investigate the temperature response for the UR at reduced volume, with the first geometry, G2, being drawn from the previous section. The essential dimensions are summarized in Table 4. Designs G4 and G5 vary from G2 by the dimensions and volume of the UR. When the volume of the UR is reduced, the relationship between volumes and heat transfer areas of steel and potassium will change, which will affect τ.

Using these new geometries, a similar study as before was performed to quantify the impact on pressure drop and τ, as shown in Figure 30. It is seen that as the volume of the upper reservoir is decreased, both the pressure drop and τ are reduced. This implies that the upper reservoir should be made as small as possible, while still containing enough volume of expander fluid, to minimize the pressure drop and τ

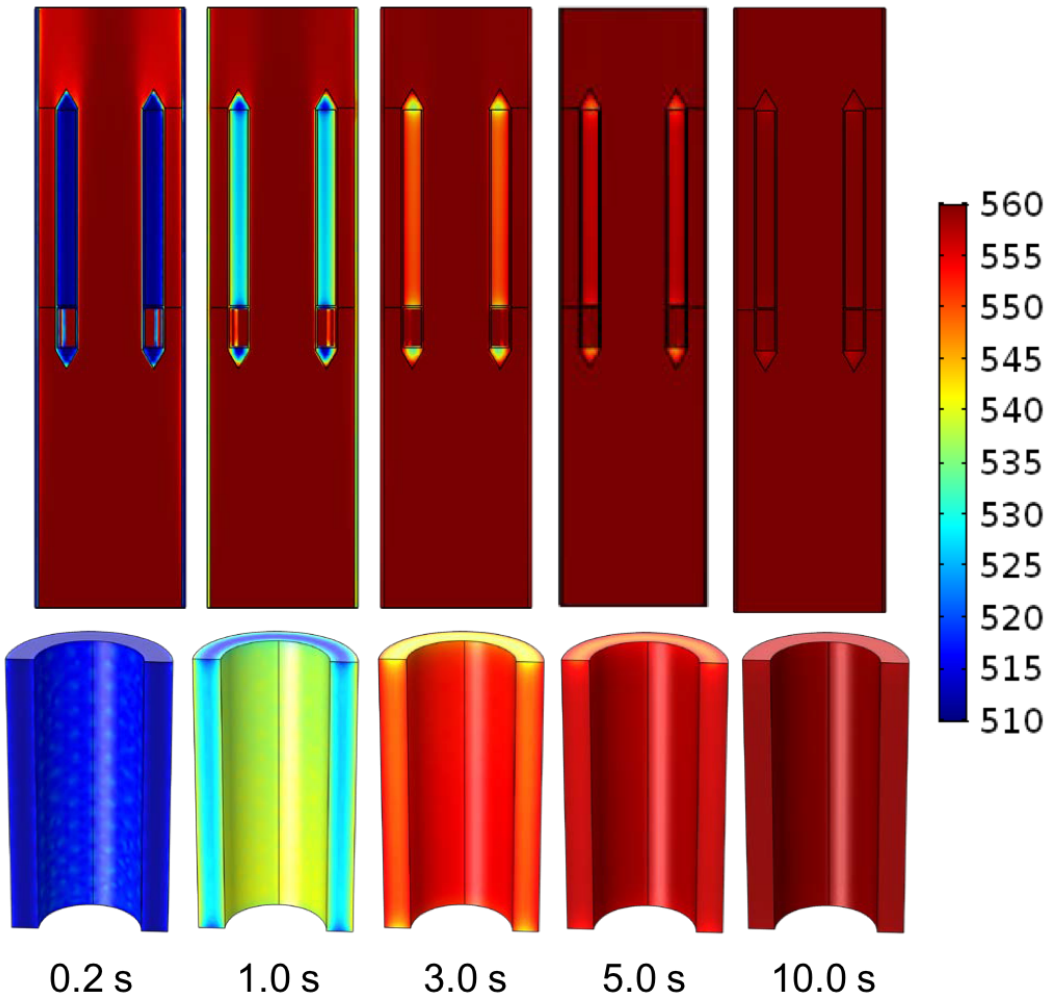

Figure 27: Temperature (°C) contour of the G2 design 1 cm away from the Y-Z symmetry plane.

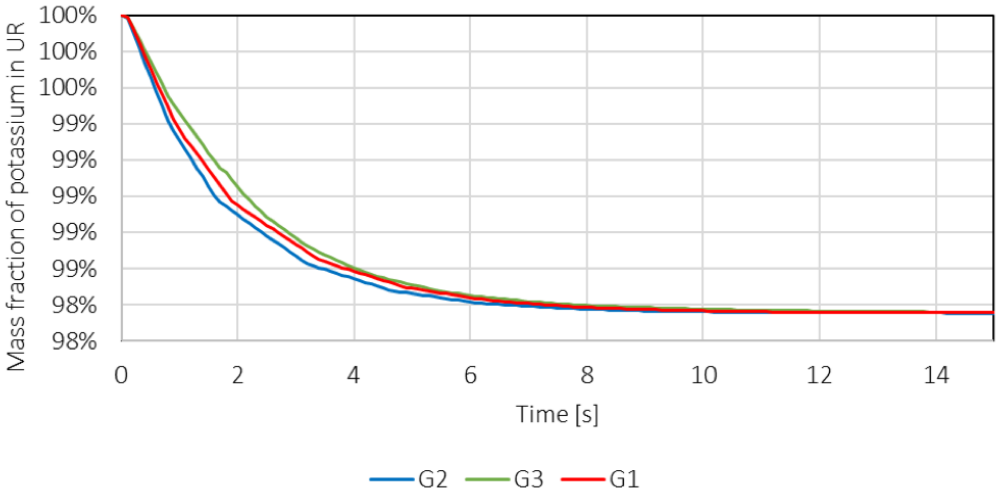

Figure 28: Comparison of mass fraction of potassium in UR for designs G1-G3.

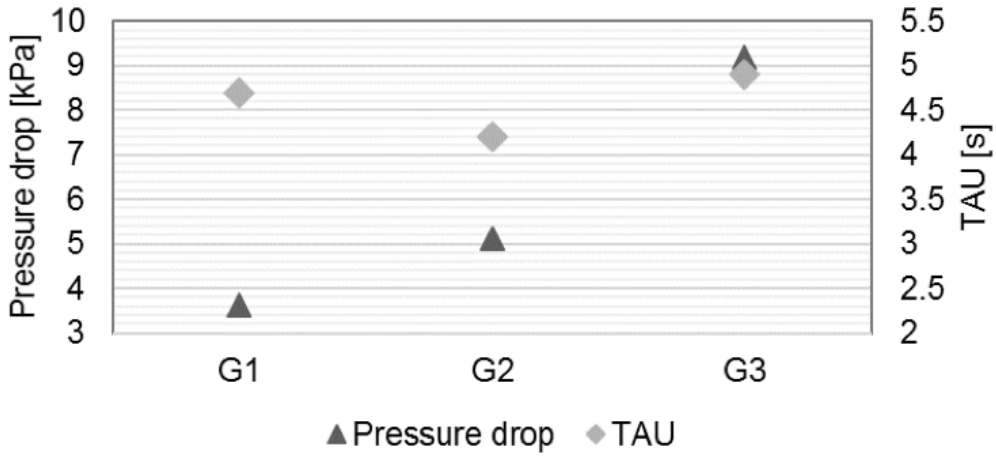

Figure 29: Summary of performance for designs G1-G3.

values.

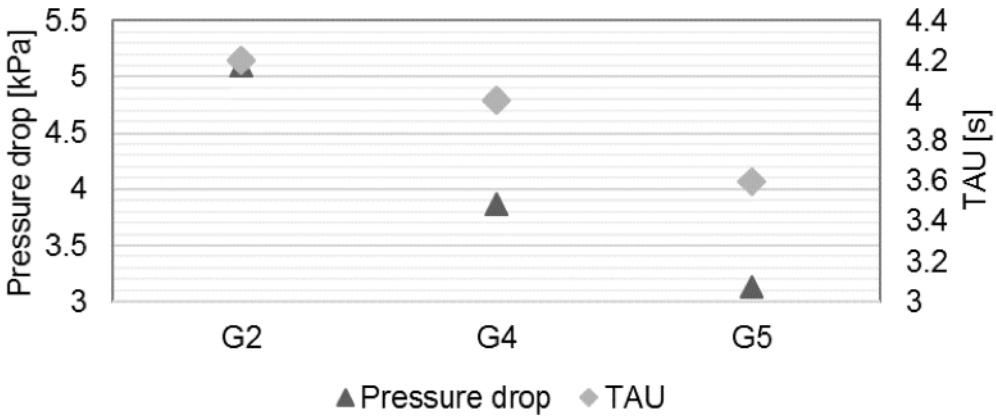

Figure 30: Summary of performance for designs G2, G4, and G5.

4.4 Impact of Coolant Flow Rate on Time Response

Because the rate of heat transfer between the coolant and the upper reservoir is strongly dependent on the core flow rate, the value of τ will change during a transient that involves varying core flow rates. This impact has been quantified through the detailed COMSOL analysis as shown in Figure 31 for the case of the ABR core. This data has also been fit to a curve as given in Equation 24, where F is the fractional core flow. It is seen that as F reduces from 1 down to roughly 0.25, the increase in τ is approximately linear. However a sharp increase is seen as τ is reduced further. Because core flow is expected to decrease down to close to 10% during a Loss of Flow (LOF) accident, this strong dependence of τ on flow rate needs to be considered during whole-core transient calculations.

$$\tau(F)\ [s] = \tau(F=1)(4.24\exp(-26.44F) + 2.074\exp(-0.729F)) \tag{24}$$

Table 4: General dimensions of the ARC geometries considered in the reduced-volume stage of the optimization.

Design Name	Dimension	Value	Unit
G2	D1	11.0	cm
	D2	6.6	cm
	H	20.0	cm
	Volume	1000	cm^3
	$V_{steel}/V_{potassium}$	1.41	-
G4	D1	9.0	cm
	D2	4.6	cm
	H	19.8	cm
	Volume	754	cm^3
	$V_{steel}/V_{potassium}$	1.77	-
G5	D1	7.9	cm
	D2	4.0	cm
	H	17.3	cm
	Volume	500.8	cm^3
	$V_{steel}/V_{potassium}$	2.5	-

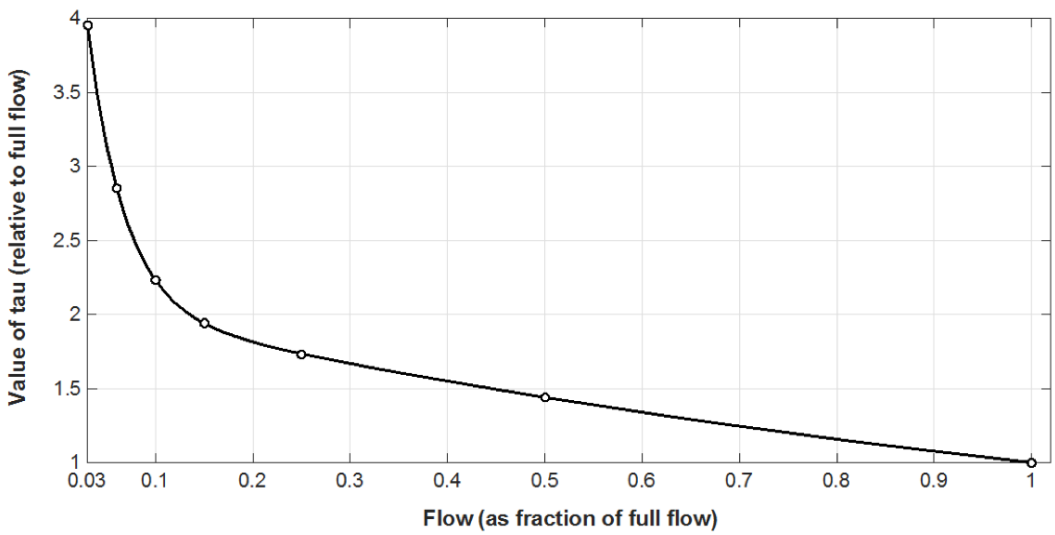

Figure 31: The impact of flow rate on the value of τ as calculated by COMSOL for the ABR core.

4.5 Effect of Wall Thermal Expansion

The temperature change in the UR causes the walls to expand, which can lead to buckling of the UR. The effect of buckling can enhance the performance of the ARC system if it exceeds the competing effect of linear expansion of the UR walls. In this section, a few UR designs are simulated to investigate to what degree steel buckling can positively contribute to ARC system performance.

Due to the complexity of the physics, the model is simplified to a 2D axisymmetric geometry. The axisymmetric model consists of a vertical cross section through the upper part of the fuel assembly and a rectangular section of the UR, as shown in Figure 32. The UR volume is not attached to the assembly wall to allow for coolant flow in the 2D geometry. Instead, the UR is fixed to an artificial vertical edge, as can be seen in Figure 32. The model includes turbulent coolant flow, heat transfer, thermal stress,

and thermal expansion. The calculations are carried out in steady-state mode to achieve results in a reasonable amount of time. This simplification is justified, since the rate at which the UR volume changes is of secondary importance in comparison to the magnitude of the volume change.

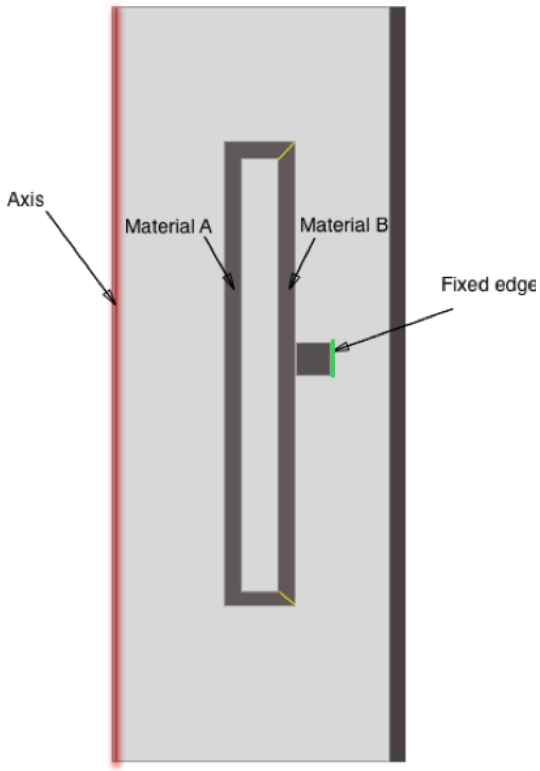

Figure 32: 2D axisymmetric geometry used to evaluate the impact of UR wall thermal expansion.

The study was carried out using four different models:

1. The thermal expansion module is deactivated so that the densities of the liquids change with the temperature but the solids remain unaffected. This provides a baseline for performance comparison.
2. A thermal expansion model is used and the UR is made completely of stainless steel.
3. The UR is made of two different materials, A and B as shown in Figure 32, where A is set to have nearly zero expansion and B is stainless steel. Such arrangement of materials was selected to promote non-uniform expansion of the UR leading to inward buckling one of the UR walls.
4. The UR is made of two different materials, A and B as shown in Figure 32, where A is stainless steel and B is set to have nearly zero expansion.

The amount of potassium pushed out of the upper reservoir in each of the cases is provided in Table 5. By taking into account thermal expansion of the inner surface of the UR, the amount of expelled potassium was increased by roughly 19%. This is a considerable improvement, however, it was achieved using a fictional material that has no thermal expansion at the outer wall. Conversely, when expansion of both walls is allowed at similar rates, the amount of potassium expelled decreases because the UR uniformly increases in volume. Therefore, while it may be possible in principle to design an upper reservoir to have the required differential expansion, more detailed analysis is required to determine the feasibility of such a scheme.

Table 5: Amount of potassium expelled from the upper reservoir using different thermal expansion models for the UR walls.

Expansion Model	Potassium Expelled (g)
1	5.45
2	4.97
3	4.57
4	5.89

4.6 Summary of Results

Many different possible configurations for the upper reservoir geometry have been considered and analyzed. A thin and tall annular reservoir minimizes the time delay of actuation of the system while maintaining added pressure drop and length-addition to the fuel assembly within acceptable limits. From this optimization, τ was able to be reduced down to as low as only a few seconds, representing a very short time delay for ARC system actuation. Further quantifications were performed to determine how τ may change with decreasing coolant flow rates. It was found that a strong dependence exists, with τ increasing nearly threefold as core flow is reduced down to 10% of nominal. Finally, the potential impacts of thermal expansion of the UR walls were investigated, although more detailed analysis is required to determine if the proper differential expansion can be achieved in realistic designs.

5 ARC System Simulation Capabilities

Previous versions of the safety analysis code system SAS4A/SASSYS-1 [21] were not capable of simulating the ARC system response in transients with variable flow rates. This is due to the fact that the reactivity inserted by the ARC system is modeled using a lag-compensator from the control system module of SAS4A/SASSYS-1. The control system samples the reactor coolant temperature at the elevation of the ARC system upper reservoir and passes this temperature to a lag-compensator. The lag-compensator uses this coolant temperature in conjunction with a user-supplied value for τ to calculate the temperature of the UR. Then, a table of reactivity versus UR temperature is used to determine how much reactivity should be inserted into the system. This value is then sent to the point reactor kinetics module, which calculates the power evolution. The equations for the lag-compensator are as follows, where $y(t)$ is the calculated UR temperature, g is a user-supplied constant (typically 1.0), $u(t)$ is the coolant temperature, and τ is a user-supplied constant delay parameter (calculated as shown in Section 4).

$$y + \tau \frac{dy}{dt} = gu \quad y(0) = y_0 \tag{25}$$

The issue with this formulation as it relates to simulating the ARC system response is that τ cannot vary with time. As was shown in Section 4, the heat transfer to the upper reservoir is severely degraded when the reactor is at low flow conditions. During a LOF, the coolant flow rate may reduce by 10x as the pumps coast down and the core transitions to natural circulation. This period of the LOF sequence is of critical importance, and therefore it is important to be able to model the changing heat transfer with decreasing flow.

The solution to this problem is to implement into SAS4A/SASSYS-1 a 'variable lag-compensator', as described by Equation 26.

$$y + \tau(t) \frac{dy}{dt} = guy(0) = y_0 \tag{26}$$

Although τ may vary between timesteps, it is assumed to remain constant within a timestep to avoid issues with the numerical approximations involved. As long as the simulation timesteps are small enough, this approximation should not be a significant limitation. The general analytic solution to Equation 26 is

$$y(t) = y_0 e^{-\int_0^t \frac{dt'}{\tau(t)}} + e^{-\int_{t_0}^t \frac{dt'}{\tau(t)}} \int_0^t \frac{u(t')}{\tau(t')} e^{\int_{t_0}^{t'} \frac{dt''}{\tau(t'')}} dt' \tag{27}$$

This expression can be numerically approximated as in Equation 28, where $\delta = \frac{\Delta t}{\tau_0}$, u_0 is the driving function at the start of the timestep, and u_1 is the driving function at the end of the timestep. The approximation in Equation 28 makes use of two Taylor expansions to avoid numerical round off errors and the use of exponential function evaluations.

$$y_1 \approx y_0[1 - \delta(1 - \delta\frac{1}{2})] + u_o[\delta(\frac{1}{2} - \delta\frac{1}{3})] + u_1[\delta(\frac{1}{2} - \delta(\frac{1}{6})] \tag{28}$$

This formulation is implemented into SAS4A/SASSYS-1 version 5.2 as a new control system function that is now available to all users. Existing checks within the control system and associated routines of the input and convergence are applied to the new feature as a quality control measure.

Figure 33 shows the results of using the implemented variable lag-compensator in SAS4A/SASSYS-1. For this test, a sine wave is passed in as the value of τ, and another sine wave of smaller amplitude is passed in as the driving function. This test gives the expected results, as it shows that with a small time delay, the lagged-signal is nearly equal to driving function. Further, it shows that with long time delays, the lagged-signal is reduced in magnitude compared to the driving signal, which is to be expected with a sine wave driving function.

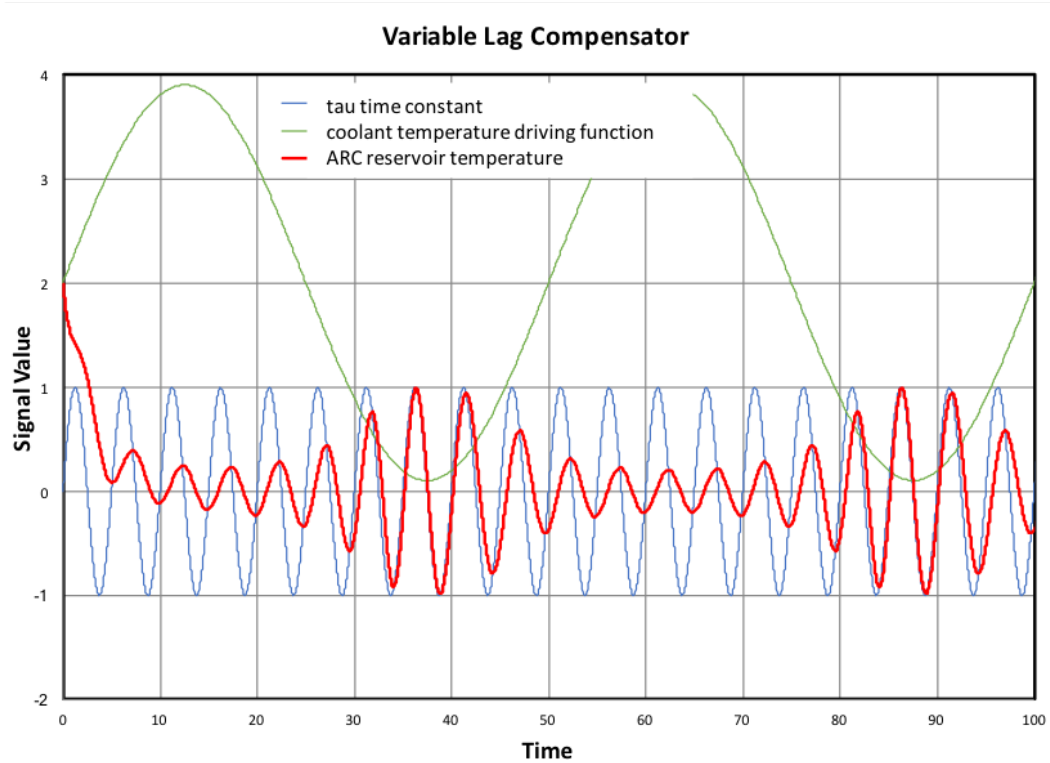

Figure 33: Test of the variable lag-compensator implemented into SAS4A/SASSYS-1 with a sine wave for the value of τ and a sine wave driving function.

Figure 34 shows a comparison between the solution from SAS4A/SASSYS-1 and a solution from Wolfram Mathematica for the test case shown in Figure 33. The relative error between the two is essentially zero, except at points where the exact solution passes through zero (where the expression for relative error blows up). This comparison gives validation that the variable lag-compensator implementation is working correctly.

To get a sense that the new capability works for reactor transient simulation, a transient model was set up for an Unprotected Transient Overpower (UTOP) beginning at 11 s where the signal controlling τ, typically representing the coolant flow rate, is reduced to nearly 0% at 30 s. In this case, the coolant flow rate is not actually reduced, but the variable lag-compensator is tricked into believing that coolant flow has essentially stopped, forcing τ to quickly jump up. Although this is not physically feasible, it is a good test case for seeing the impact of the variable-lag compensator. The coolant outlet and reservoir temperatures begin to change a few seconds after control rod withdrawal due to the time it takes for coolant to reach the outlets and the thermal inertia of structures above the active core. Figure 35 shows the response of τ and the resulting ARC reservoir temperature during the first 100 s of this transient. It can be seen that when τ makes a sudden jump, a cusp in the reservoir temperature occurs. Immediately after this, the difference between coolant and reservoir temperatures is much larger, indicating that the variable lag-compensator is accounting for the changing value of τ.

An example of the variable lag-compensator as used in a ULOF accident scenario is shown in Figure 36. This scenario is for an oxide-fueled ABR design from Argonne National Laboratory (introduced later in Section 6) with an ARC system installed, where the power to the primary and secondary coolant pumps is lost at 11 s. The time constant supplied to the variable lag-compensator can be seen to increase smoothly as the flow rate decreases, and the ARC reservoir temperature lags behind the coolant outlet temperature accordingly. The peaks in coolant temperature arise from the ARC system injecting and removing reactivity as the reactor power responds to the ARC system actuation. This example is another

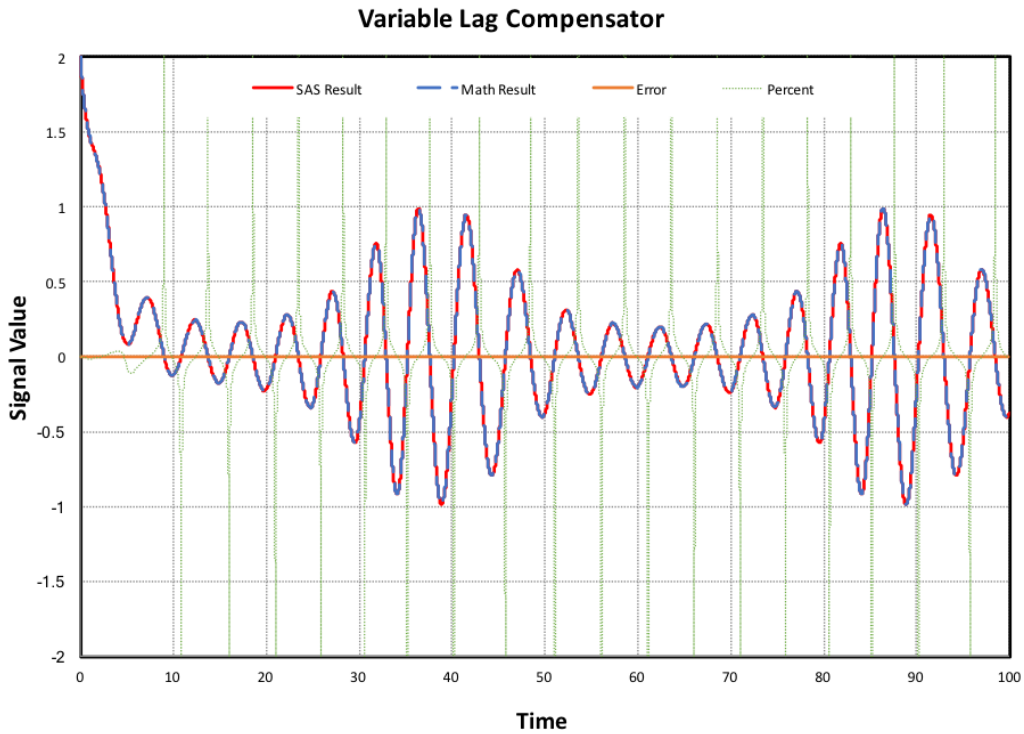

Figure 34: Comparison between the SAS variable lag-compensator result and Wolfram Mathematica result for the test case shown in Figure 33.

confirmation that the implementation of the variable lag-compensator is working as intended.

With the addition of the variable lag-compensator, SAS4A/SASSYS-1 is now able to capture the phenomenon of retarded heat transfer at low flow rates during a LOF accident scenario.

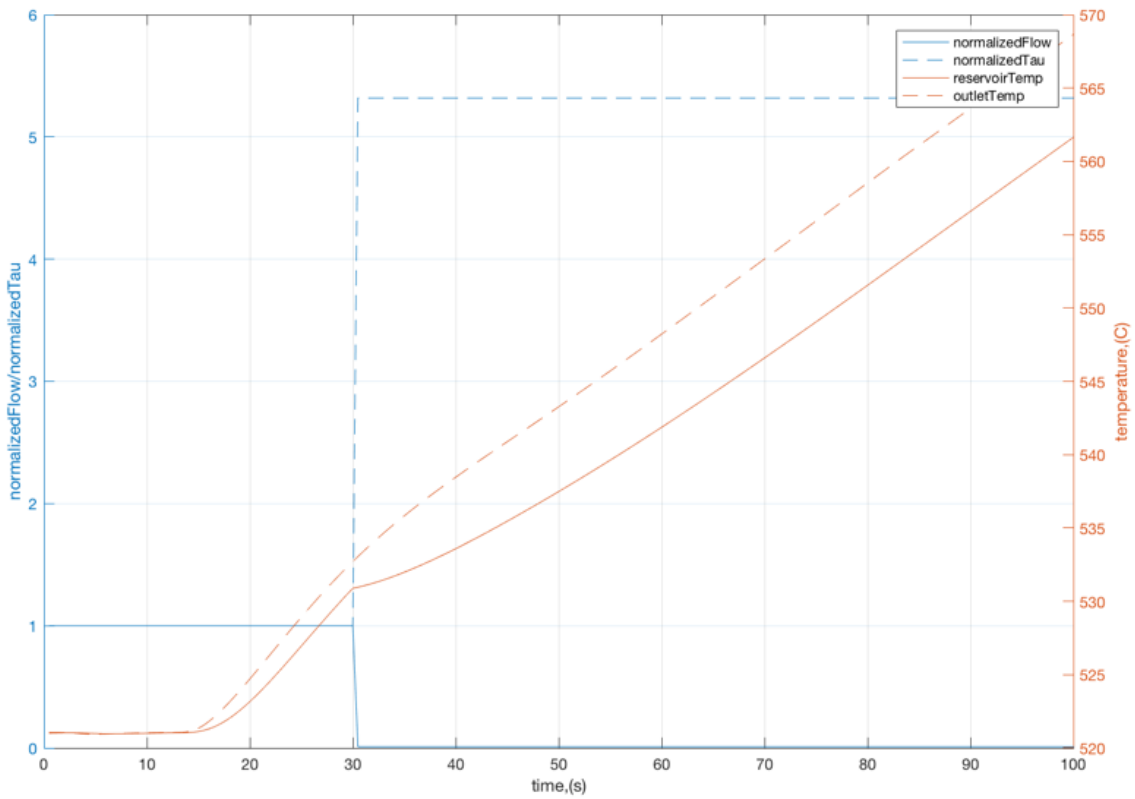

Figure 35: Coolant and reservoir temperatures during a UTOP event in the metallic ABR with a step change in τ showing that the curvature of the reservoir temperature curve changes with τ.

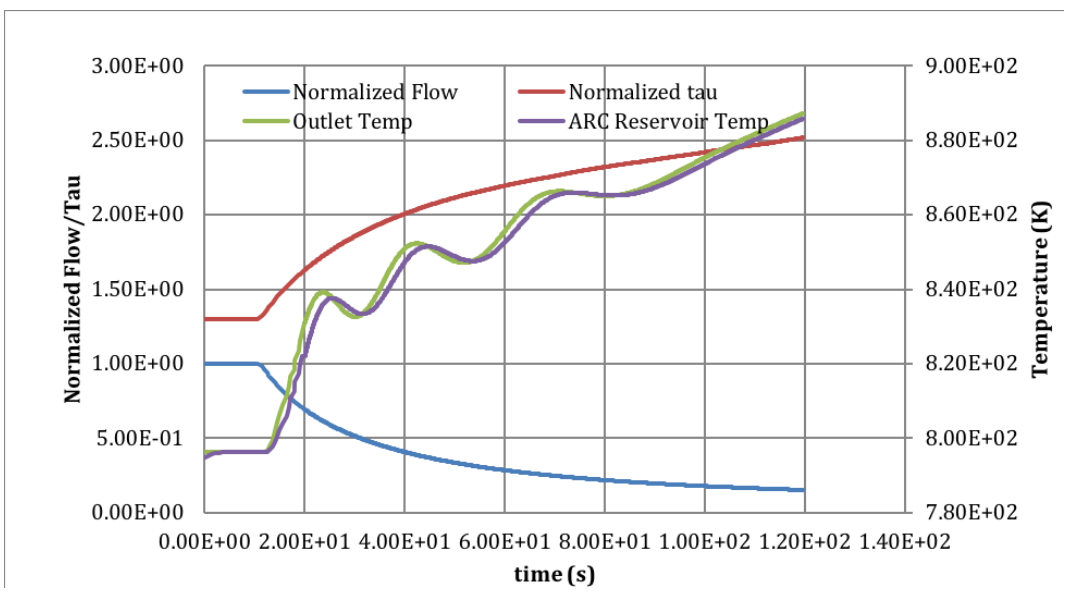

Figure 36: Flowrate, tau, outlet temperature, and ARC reservoir temperature during the first two minutes of a ULOF transient in the oxide ABR with an ARC system installed.

6 Reference Cores

In order to examine the potential benefits of ARC system inclusion in different SFR designs, two different cores were examined in this study. The two cores have different missions and different fuel types, and thus widely varying characteristics. This section provides the details of each reference core along with a comparison of important characteristics.

6.1 Oxide ABR Core

The first reference core is selected to be a medium-sized oxide-fueled Advanced Burner Reactor (ABR) designed by Argonne National Laboratory and outlined in the study by Kim et al. [1]. The core, whose layout is provided in Figure 37, utilizes a batch fuel management scheme, with one sixth of the core discharged after every cycle. The ABR takes as charge fuel natural uranium enriched with recycled TRU, with a core-average enrichment of 28%. The equilibrium TRU vector is provided in Table 6.

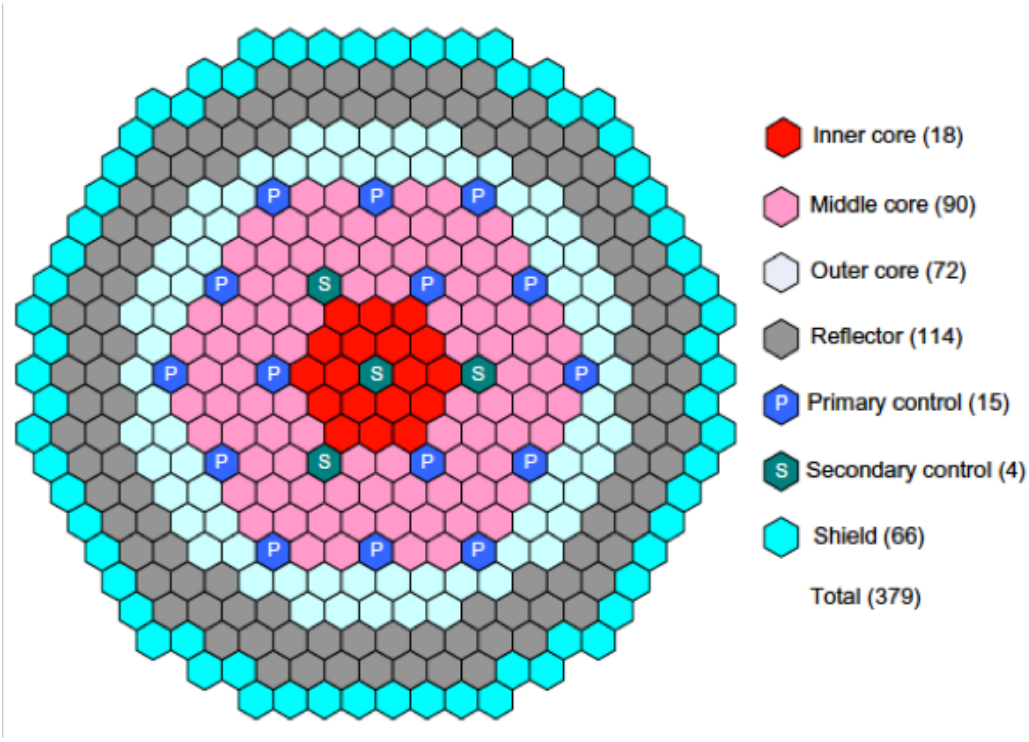

Figure 37: Core layout for the reference ABR core [1].

The distribution of fuel, cladding, coolant, and fuel doppler worth at the Beginning of Equilibrium Cycle (BOEC) are provided in Figures 38-40, as calculated by VARI3D [22]. In these figures, 'outer core' refers to both the 'middle core' and 'outer core' regions of Figure 37. Values are provided for BOEC because this is the point in the cycle with the largest excess reactivity held down by the control system, making it the most challenging in the case of a TOP. The core was orificed into a handful of orifice groups, although the detailed distribution of these groups are not provided. The flowrates allocated to each group were determined so that the average outlet temperature equals the desired value of 510°C.

6.2 B&B Core

The second reference core was selected to be a large, low-leakage B&B SFR. The B&B reference design is derived from studies of optimal fuel shuffling performed by Hou et al. [23]. The core layout and shuffling scheme are provided in Figure 42.

Table 6: TRU vector of the charge fuel of the ABR core [1].

Isotope	Percent
Np-237	1.5
Pu-238	3.1
Pu-239	41.1
Pu-240	31.3
Pu-241	5.7
Pu-242	8.1
Am-241	3.6
Am-242m	0.2
Am-243	2.6
Cm-243	0.0
Cm-244	1.8
Cm-245	0.5
Cm-246	0.3

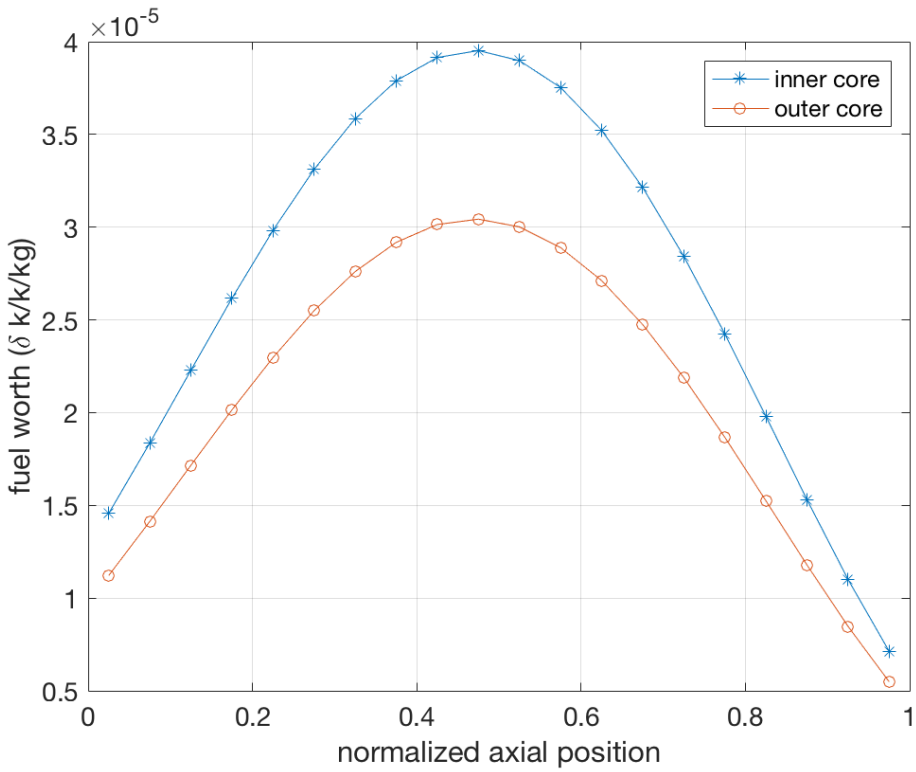

Figure 38: Distribution of fuel worth in the ABR core.

While the design of the oxide ABR is more or less standard, the B&B core incorporates a number of unique design choices. In order to achieve breed-and-burn operation, neutron leakage needs to be very low so that the required burnup and associated cladding damage is not too great. This forces most breed-and-burn designs to be very large cores. Additionally, breeding is more effective at high neutron energies, and so the lattice pitch must be kept as small as possible to reduce parasitic absorption and moderation in the coolant. To allow for a tight lattice pitch, the fission gas plenum is removed to reduce the coolant pressure drop, necessitating the use of fission gas venting. Finally, the need for high fuel

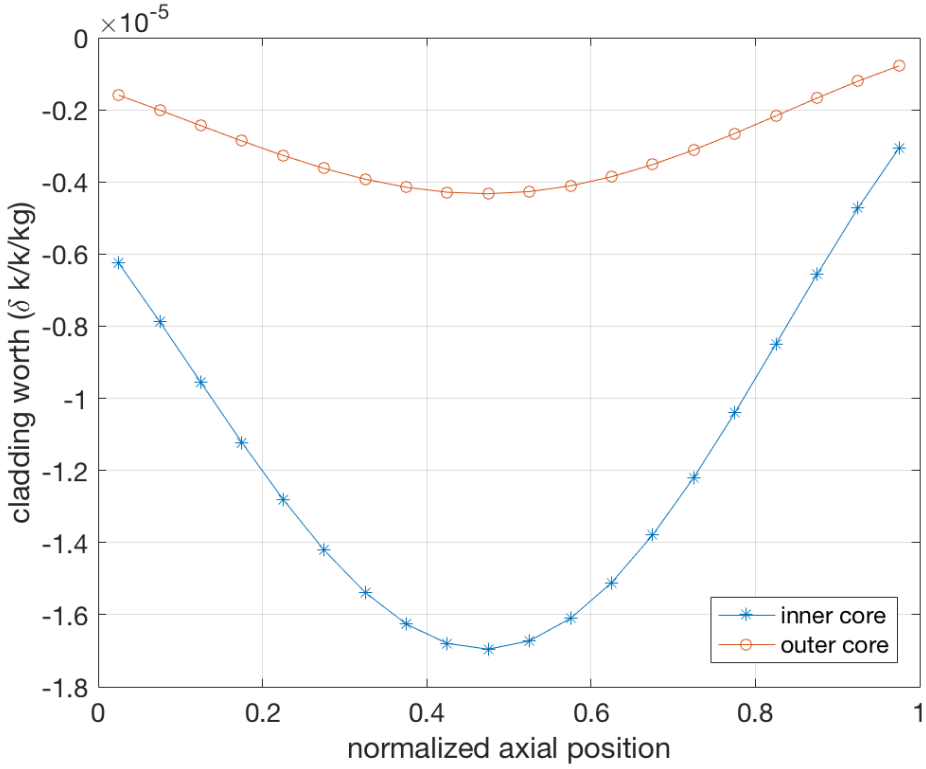

Figure 39: Distribution of cladding worth in the ABR core.

inventory necessitates metallic fuel, which as well avoids the thermalization that takes place with oxide fuel and enables a very hard spectrum. These design choices lead to a strongly positive coolant void reactivity feedback, which when combined with the small doppler resulting from metallic fuel, can be challenging from the perspective of passive safety. More details on the fundamental design choices and their justifications for the B&B core can be found in [23].

Each batch of fresh fuel is composed of depleted uranium (DU), with fissile material being bred as fuel is shuffled inwards. Fuel assembly volume fractions are provided in Table 8. Radially surrounding the core is one row of steel reflector assemblies followed by one row of B_4C shield assemblies, both of which are approximated as smeared-composition annular cylinders. Below the core is a 5 cm thick B_4C shield, while above the core is a 10 cm gas plenum followed by a 5 cm B_4C shield. Each shield is composed of 90 weight% enriched B_4C (smear density of 98%) clad in HT9, with volume fractions of 50.8%, 11.9%, 25.3%, 7.0%, and 4.1% for shield, clad, active coolant, duct, and inter-assembly coolant materials, respectively.

The power distribution of this core, as shown in Figure 43 at the End of Equilibrium Cycle (EOEC), was calculated with Serpent 2 [24] using the coupled neutron-photon transport mode to account for energy deposition in fertile assemblies by photons. The reactivity worth of fuel, cladding, and coolant, provided in Figures 44-46, were calculated using the Generalized Perturbation Theory (GPT) capabilities of Serpent 2 [25]. The doppler feedback worth was calculated using the Extended Generalized Perturbation Theory (XGPT) capabilities [26] by manually doppler broadening the fuel cross-sections for a 5°C temperature increase and using the energy-dependent difference between the broadened and un-broadened cross-sections as a perturbation function. The doppler worth distribution in given in Figure 47. In these figures, Channels 1, 2, 3, and 4 correspond to Batches 1, 2-3, 4-6, and 7-12, respectively, as will be discussed when the whole-core transient model is introduced in Section 8.

As opposed to the simple orificing that was assumed in the ABR core, the situation is more complicated in the B&B core. The combination of large assembly power swings, assembly shuffling, and the significant

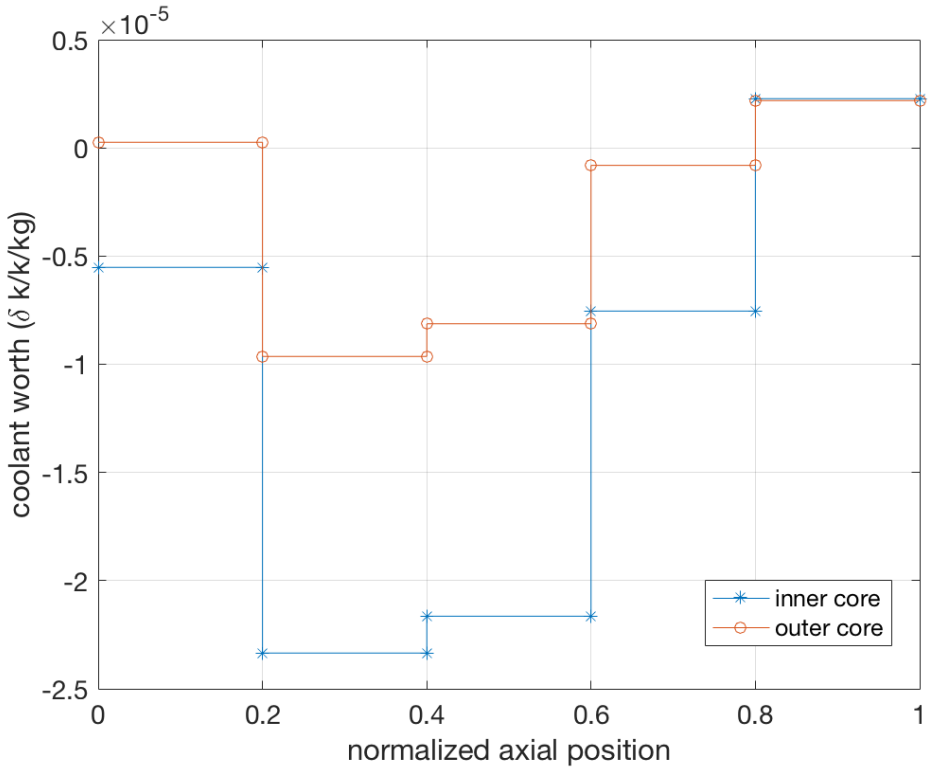

Figure 40: Distribution of coolant worth in the ABR core. Values on the fine mesh of Figures 38 and 39 were not available for the coolant worth.

gradient in power across the core make it difficult to develop acceptable orificing schemes. Therefore orificing of assemblies was performed using an optimization method developed during the course of this project, outlined in detail by Keckler et al. [27]. This method attempts to minimize the number of orifice groups while determining the allocated flow rates so as to satisfy the constraints outlined in Table 7. The resulting flow distribution is provided in Figure 48, where 14 unique orifice groups were used. Although fewer orifice groups have been shown to be possible using the same core and constraints, the analysis in this project stopped the optimization procedure before reaching optimality due to computational expense.

Table 7: Nominal constraints used for the orificing optimization in the B&B core.

Parameter	Value	Units
Maximum assembly-average coolant temperature rise	210	$°C$
Average mixed core outlet temperature	510	$°C$
Tolerance on the mixed core outlet temperature	5	$°C$
Maximum assembly-average coolant velocity	12	m/s
Maximum difference in average outlet temperature between adjacent assemblies	50	$°C$

6.3 Comparison of the Reference Cores

A summary of key characteristics of each core is given in Table 8. The cycle length of the B&B core is nearly 3 times that of the ABR, while the number of batches is also double, making the fuel residence time in the B&B core nearly 6 times longer than in the ABR core. Because the ABR is a burner core while the B&B is a breeder, the reactivity swings are opposite in sign, although similar in magnitude.

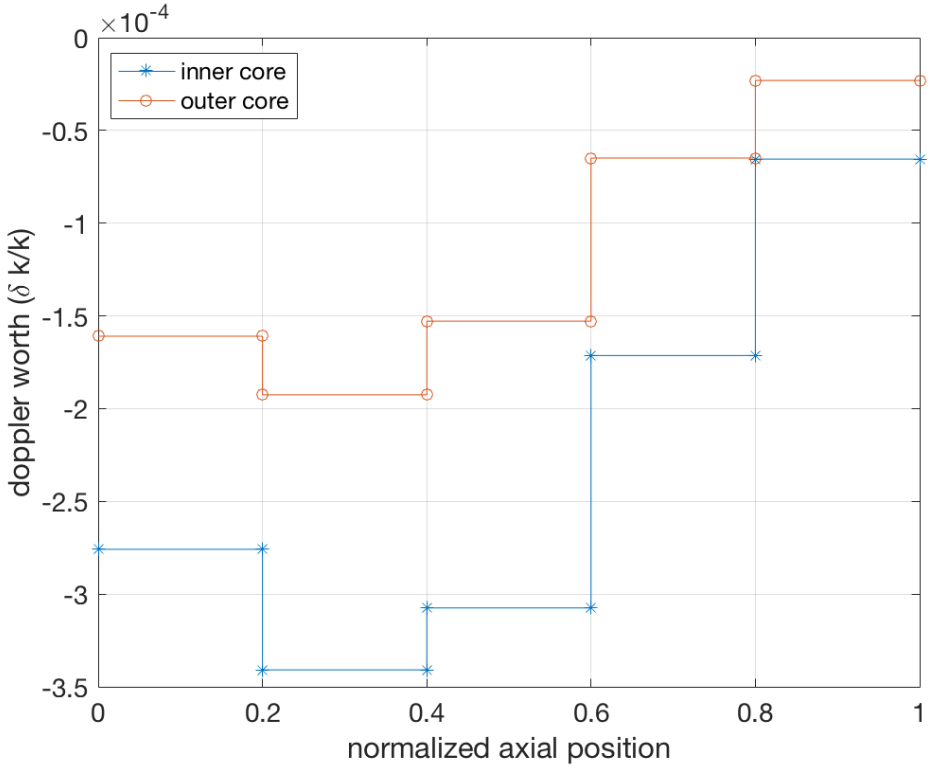

Figure 41: Distribution of fuel doppler worth in the ABR core under flooded conditions. Values on the fine mesh of Figures 38 and 39 were not available for the doppler worth.

This difference makes the point of highest excess reactivity at BOEC for the ABR, while excess reactivity is greatest at EOEC in the B&B core. This impacts when the UTOP is simulated, as the worst case will be when the core has the largest excess reactivity held down by the control system.

The ABR core is smaller in size than the B&B core and has a smaller height-to-diameter ratio. This leads to a lower leakage probability in the B&B core, with a corresponding larger coolant void reactivity. When comparing the distribution of sodium worth (the inverse of void worth) between the two cores in Figures 40 and 46, the ABR has regions near the axial periphery where coolant worth turns positive, whereas coolant worth is always negative in the B&B core due to its very low leakage. The coolant void reactivity is further exacerbated in the B&B core due to the harder spectrum resulting from the use of metallic fuel and larger fuel volume fraction. The different fuel type also has an impact on doppler coefficients, although the difference is smaller than that between the coolant void reactivities. However the strength of the doppler feedback is also impacted by transient fuel temperatures, which tend to increase more strongly in the ABR due to the use of oxide fuel that has significantly lower thermal conductivity.

The control rod driveline feedback in the ABR core is much stronger than that in the B&B core due to the shorter height of the ABR, although the feedback in the B&B core is well approximated by a linear relation, whereas the ABR control rod driveline is not. This weaker feedback is partially compensated by the higher thermal conductivity of metallic fuel, which allows for the control rod driveline feedback to act more quickly.

Because the ABR is enriched with TRU, it has a slightly smaller delayed neutron fraction than the B&B core, whose primary fissile isotope is Pu-239. Conversely, the prompt neutron lifetime in the B&B core is less than half of the ABR core due to differences in spectrum. These differences affect the kinetics of the transients in each core, and especially the small neutron lifetime of the B&B core can make passive safety challenging.

Table 8: Design parameters of the oxide ABR and metallic B&B cores.

	ABR	B&B	units
Thermal Power	1000	3500	MW
Cycle Length	365	916	days
Number of Batches	6	12	-
Reactivity Swing	-2.3	3.05	%
Conversion Ratio	0.66		-
Active Fuel Height	114.3	300.0	cm
Core Diameter	321.1	453.0	cm
Gas Plenum Height	160.0	- [a]	cm
Clad Thickness	0.056	0.061	cm
Pin Diameter	0.626	1.222	cm
Fuel Volume Fraction	35.0 [b]	50.8 [c]	%
Fuel Type	UO_2-$TRUO_2$	DU-10Zr	-
Fuel Thermal Conductivity [d]	4.0	30	W/m-K
Fuel Specific Heat Capacity [e]	0.26	0.12	kJ/kg-K
Coolant Void Worth [f] [g]	1.253E-02	4.597E-01	δ k/k
Doppler Coefficient [h]	-3.33E-03	-4.79E-04	δ k/k
Control Rod Driveline a [i]	-43.86	-12.49	\$/m
Control Rod Driveline b [j]	-42.84	0.00	\$/m^2
Delayed Neutron Fraction	0.00316	0.00359	-
Prompt Neutron Lifetime	0.48	0.19	μs
Pump Coast Down Time	20	20	s

[a] Fission gas is vented, and therefore there is no gas plenum.
[b] Volume fraction before swelling takes place. An 85% smear density is used.
[c] Volume fraction before swelling takes place. A 75% smear density is assumed.
[d] Values used in transient model are complicated functions of temperature and porosity. Values listed are representative.
[e] Values used in transient model are complicated functions of temperature and porosity. Values listed are representative.
[f] Values are for fully voided core, including reflector and shield.
[g] At BOEC and EOEC for the ABR and B&B cores, respectively.
[h] Values are for flooded core.
[i] Control rod driveline feedback is calculated as $a * dx + b * dx^2$, where dx is the insertion depth
[j] Control rod driveline feedback is calculated as $a * dx + b * dx^2$, where dx is the insertion depth

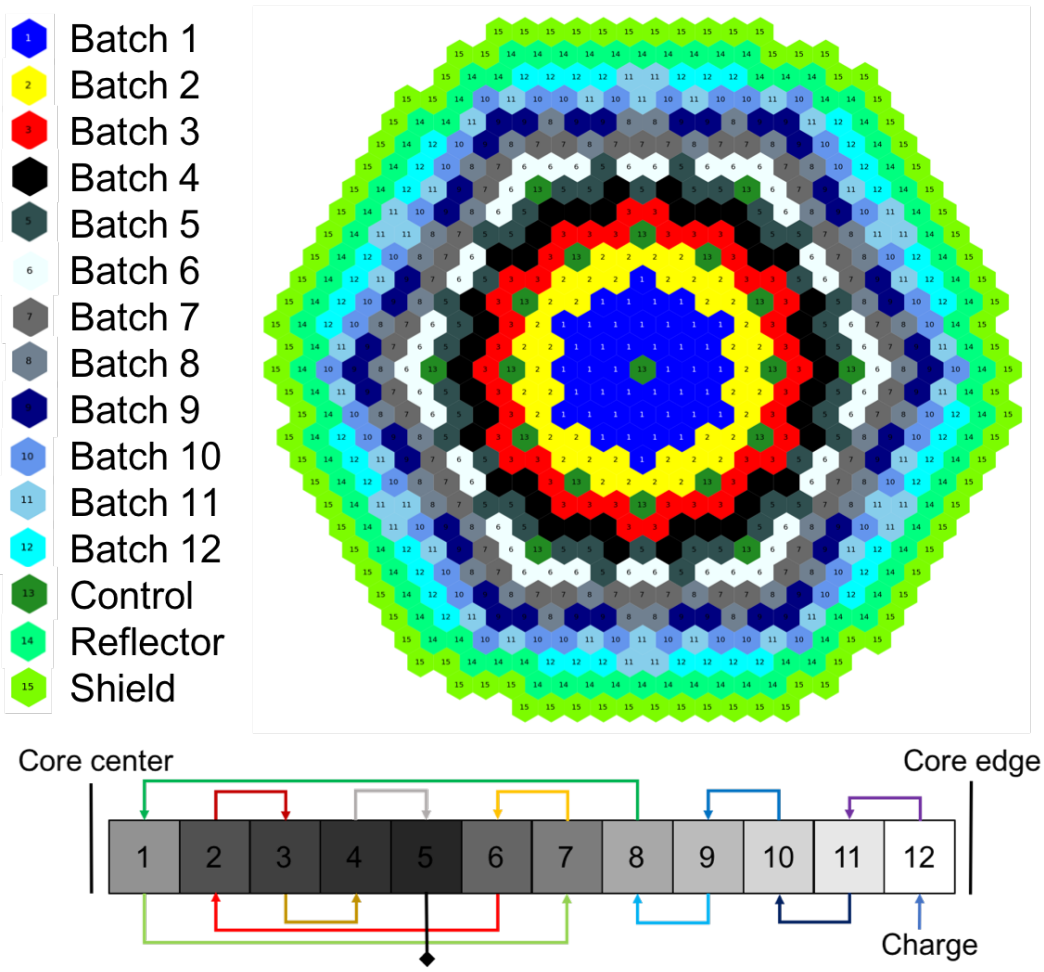

Figure 42: Core layout and shuffling scheme for the reference B&B core.

As shown in Figures 38 and 44, the material worth distributions are much more sharply peaked in the B&B core. Additionally, the majority of worth is concentrated in a relatively small fraction of assemblies. This is consistent with the highly peaked power profile depicted in Figure 43, whereas the power profile of the ABR is much more smoothly varying. This localization of worth impacts distribution of control assembly worth, with each of the control assemblies in the B&B core holding down a relatively large amount of reactivity. This has important implications on the results of a TOP scenario.

Finally, the strong radial power gradients in the B&B core coupled with the fuel management scheme make it so that the high-powered assemblies in the B&B core have higher outlet temperatures than the corresponding high-powered assemblies in the ABR core. This puts the B&B core at somewhat of a disadvantage because it leads to smaller thermal margins even during steady-state operation, making peak temperature constraints harder to meet during transient scenarios. This may be especially important because metallic cores are generally more thermally constrained than oxide cores due to the relatively low temperature of fuel-cladding eutectic formation.

6.4 Plant Systems

Despite their differences, both reactors utilize the same heat transport and balance-of-plant systems, with that for the B&B core simply a scaled-up version of the ABR's to match the higher thermal output. An overview of the plant systems is presented in Figure 49. The primary loop consists of four pumps taking suction from the cold pool and directing the flow through the core, where it is heated. Core flow exits

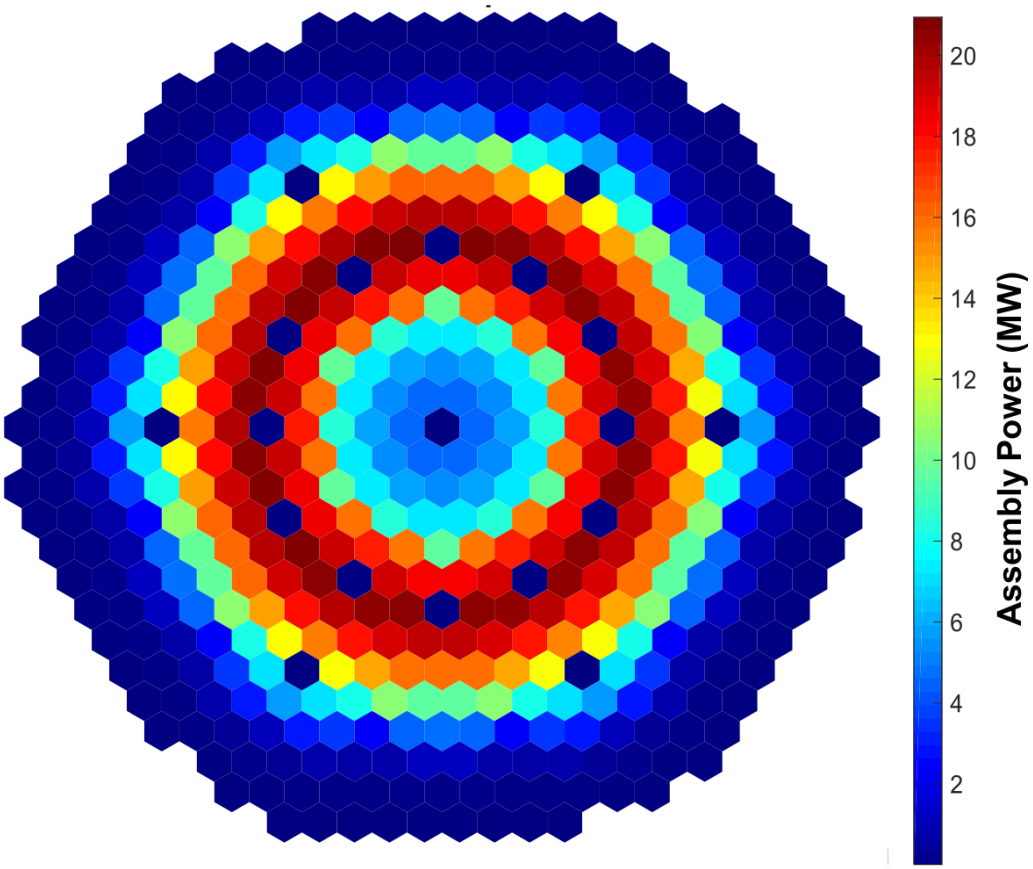

Figure 43: Assembly-wise power profile of the B&B core at EOEC.

into the outlet plenum and then flows through the shell-side of the Intermediate Heat Exchangers (IHXs) before again entering the cold pool. While Figure 49 only shows a single intermediate loop, in actuality there are four identical loops. These four loops provide the primary heat removal capability to the core. As the intermediate loop flow traverses through the IHXs, it accepts heat from the primary loop flow. The intermediate flow is then pumped up and out of the pool to the steam generators, where it gives up its heat to produce steam before being pumped back down to the IHXs.

In the absence of forced circulation in the intermediate loops, reactor heat is removed through the Direct Reactor Auxiliary Cooling System (DRACS). Again, although only one DRACS loop is depicted in Figure 49, there are actually two independent DRACS loops. Each DRACS loop is designed to remove 0.5% of core power at nominal conditions when operating at full capacity. The DRACS loops operate similarly to the intermediate loop, with primary flow traversing through the shell-side of the DRACS Heat Exchangers (DHX) as it moves from the outlet plenum back to the cold pool. However, unlike the intermediate loop, the DRACS loop utilizes NaK as the working fluid. While the DRACS loops are only meant to remove heat during an accident scenario, they operate continuously via natural circulation of the NaK working fluid. To minimize losses during normal operation, dampers are placed on the air-side of the NaK-to-air heat exchangers that act as the ultimate heat sinks for the DRACS loops. In the case of an accident scenario, these dampers may be opened to allow the DRACS loops to operate at full capacity.

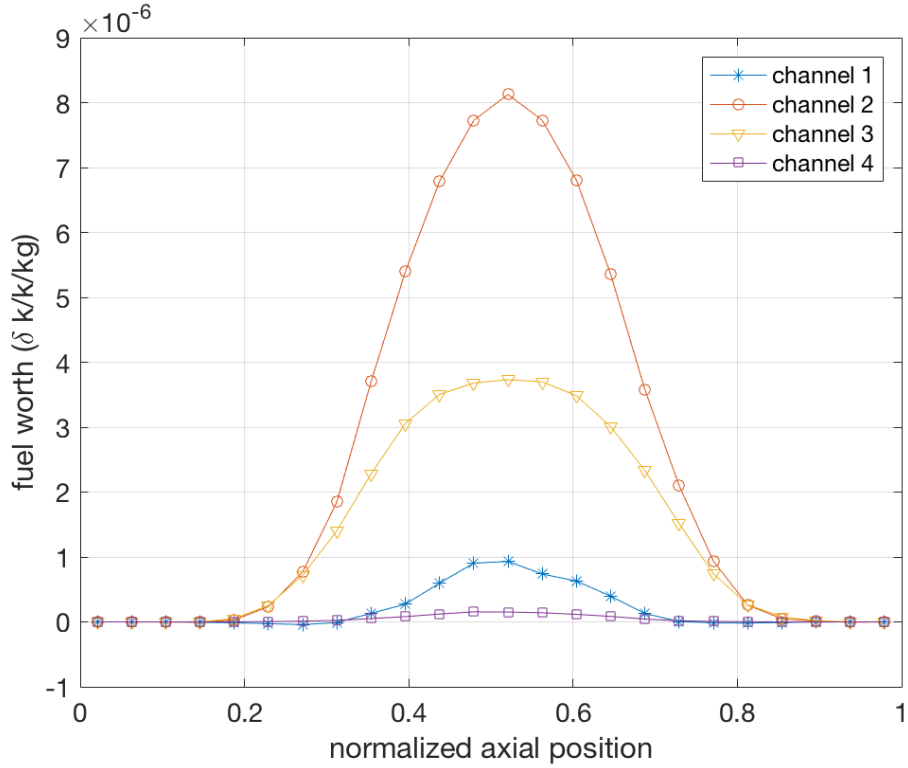

Figure 44: Distribution of fuel worth in the B&B core at EOEC.

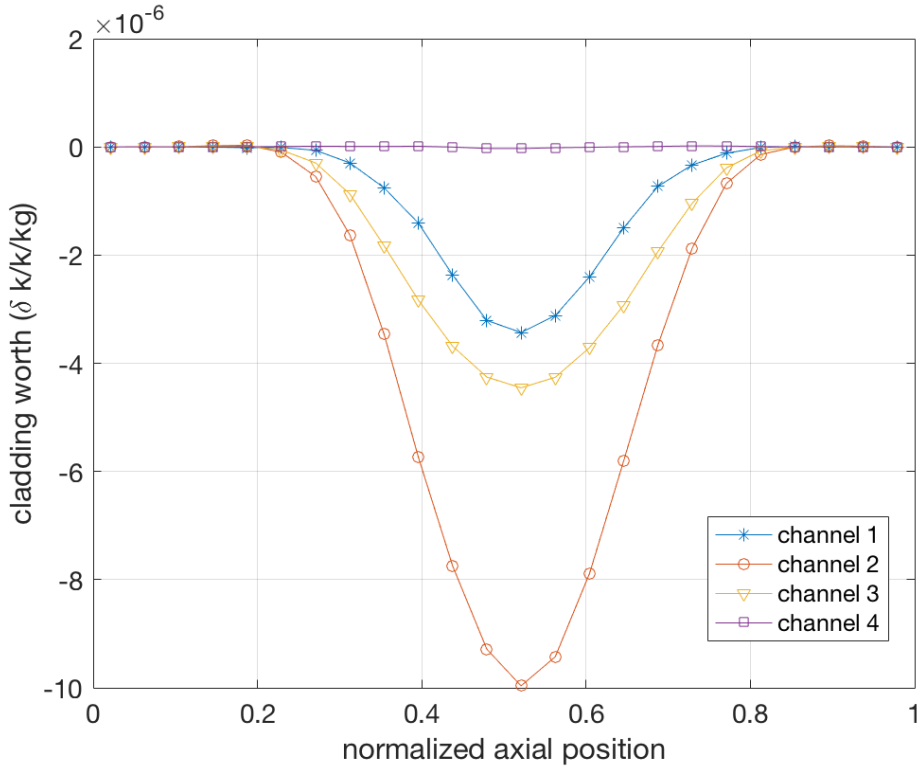

Figure 45: Distribution of cladding worth in the B&B core at EOEC.

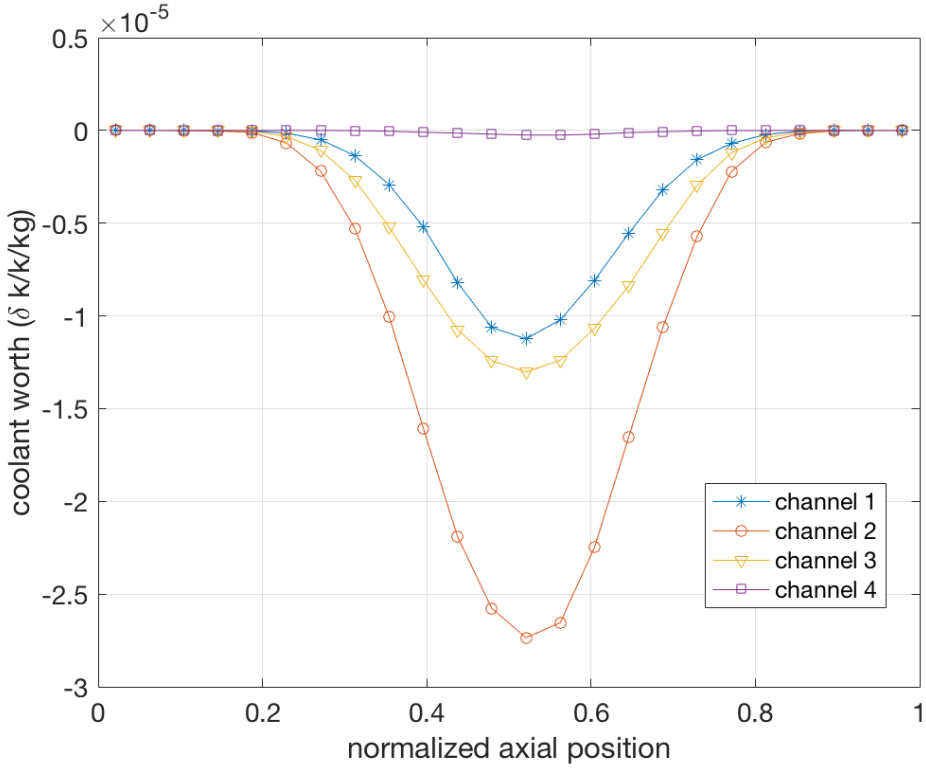

Figure 46: Distribution of coolant worth in the B&B core at EOEC.

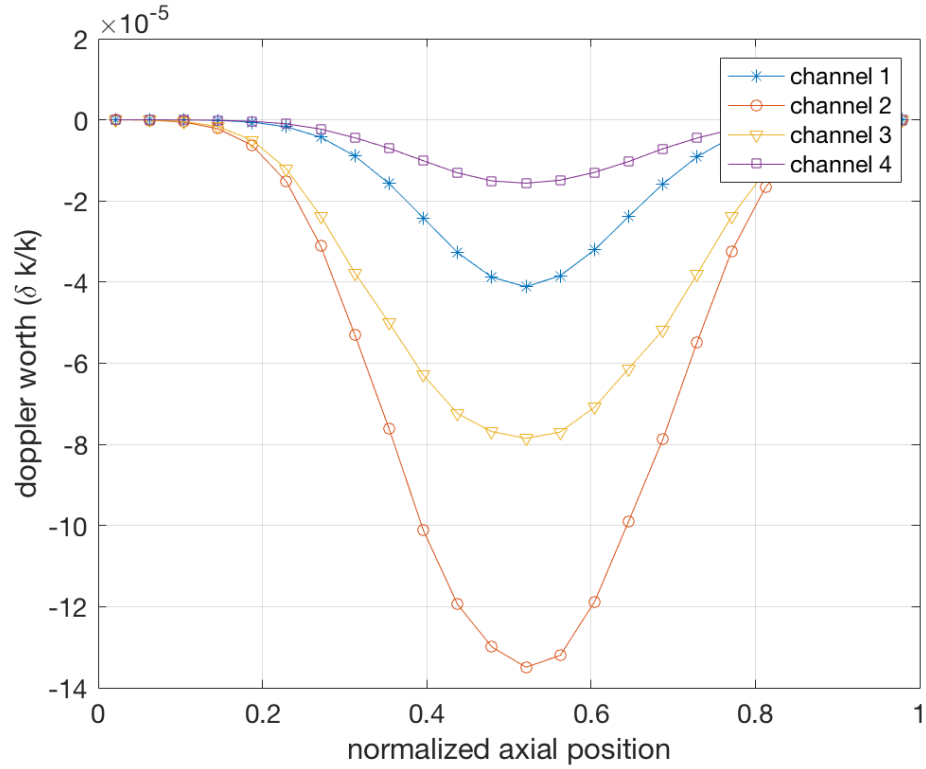

Figure 47: Distribution of doppler worth in the B&B core at EOEC under flooded conditions.

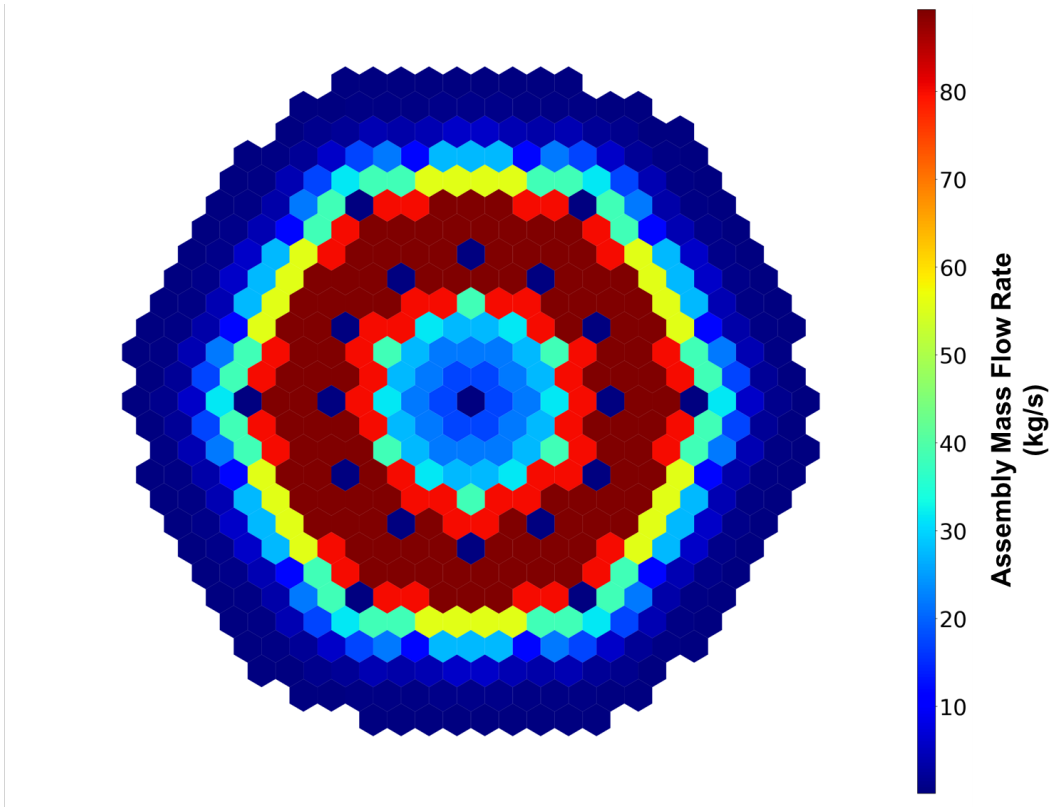

Figure 48: Assembly mass flow rates in the B&B core resulting from the orificing procedure and constraints outlined in Table 7.

7 Performance of the Oxide ABR core

7.1 Transient Model

For the modeling of transient behavior, the SAS4A-SASSYS-1 code system is used. The complete transient model for the oxide ABR without ARC system installation was obtained from the collaborator at Argonne National Laboratory.

The core assemblies were grouped into 4 channels – two representing the driver assemblies, one representing the peak power-to-flow assembly, and one representing the control and shield assemblies. A diagram of the channel allocation is provided in Figure 50.

Each channel represents the average behavior of the constituent assemblies by using a single flow channel model, as depicted in Figure 51. In this model, all fuel pins are smeared into a single average fuel pin, with representative amounts of cladding, coolant, and structure. Additionally, the wire-wraps are smeared into the cladding. As heat is generated in the fuel, 1D conduction is allowed to the radially-adjacent nodes from the fuel, through the cladding, and into the coolant. Further conduction is allowed into the structure material, which is represented by a 1D slab. As the coolant flows upward, conduction is allowed back to the solid components, allowing for a psuedo-2D treatment within each channel. Although the model allows for heat generation in the cladding and coolant, all power was assumed to be generated in the fuel. Below and above the fueled region are reflectors and plena, which are treated in a similar manner as the fueled region, except without any heat generation. For the ABR model, the number of radial and axial nodes in each axial segment of the core are provided in Table 9.

The core power evolution is calculated using a point reactor kinetics approach. The transient model accounts for reactivity feedback from axial expansion of the fuel, cladding, and structure; radial expansion of the grid plate; doppler broadening with fuel temperature; coolant density with coolant temperature;

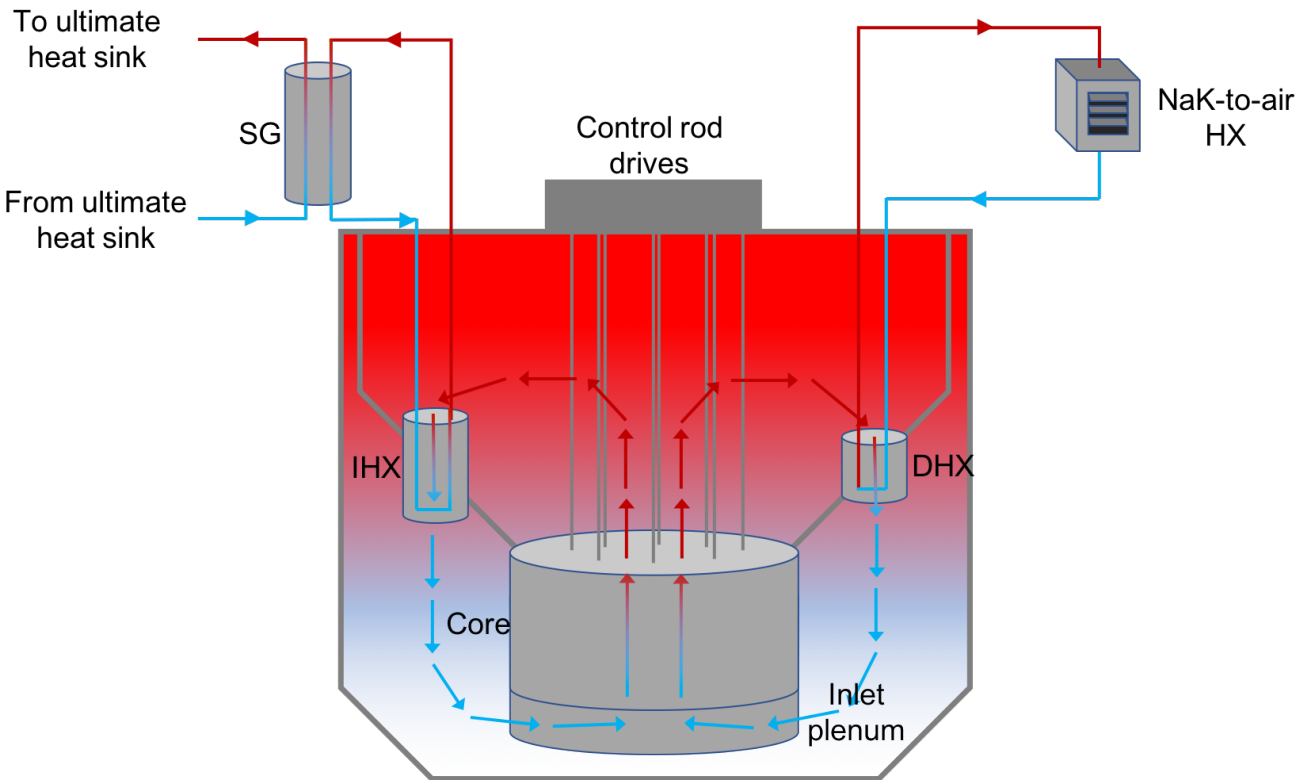

Figure 49: General plant layout for both reference cores.

and thermal expansion of the control rod drives. The axial expansion feedbacks are calculated by using the temperature of each axial node to thermally expand the fuel, cladding, and structure. Then, the worth curves for each constituent are used to calculate a reactivity response. Because the constituent worths in each channel may vary, the spatial-dependence may be partially accounted for. Similar methods are used to calculate the radial expansion feedback, where a 0D temperature for the grid plate is combined with the temperature of the upper load pads to determine how far the core has expanded. The control rod driveline feedback is determined according to the differential expansion of the control rod drivelines and the core barrel. As core flow washes over the control rod drivelines, a 0D temperature is calculated and the drivelines are thermally-expanded. Similarly, a 0D model is used to determine the temperature of the core barrel, from which the grid plate is suspended. The differential expansion determines how far the control rods are inserted into the core during a transient, which is used in conjunction with a control rod worth curve to determine a reactivity impact. The assembly bowing feedback mechanism is not accounted for.

For cases with the ARC system included, a few modifications to the transient model are made. First, the core channel model is expanded to include regions above and below the core for the upper and lower reservoirs, respectively. During a transient, the outlet temperature is sampled and the upper reservoir temperature is calculated using the lag-compensator formulation of Equation 23,where τ is taken from the CFD calculations of Section 4. Initially, all simulations including the ARC system used $\tau = 1.3$ s, as this was the smallest value that was found to be feasible through COMSOL simulations. The ARC system feedback is simulated using the control system module in conjunction with a reactivity versus upper reservoir temperature curve. These curves, in principle similar to differential rod worth curves, are generated by using the CFD results of Section 4 and curves of reactivity versus lithium insertion height built with Serpent 2. As the upper reservoir heats up, a reactivity signal is sent to the point kinetics model to represent the impact of the ARC system.

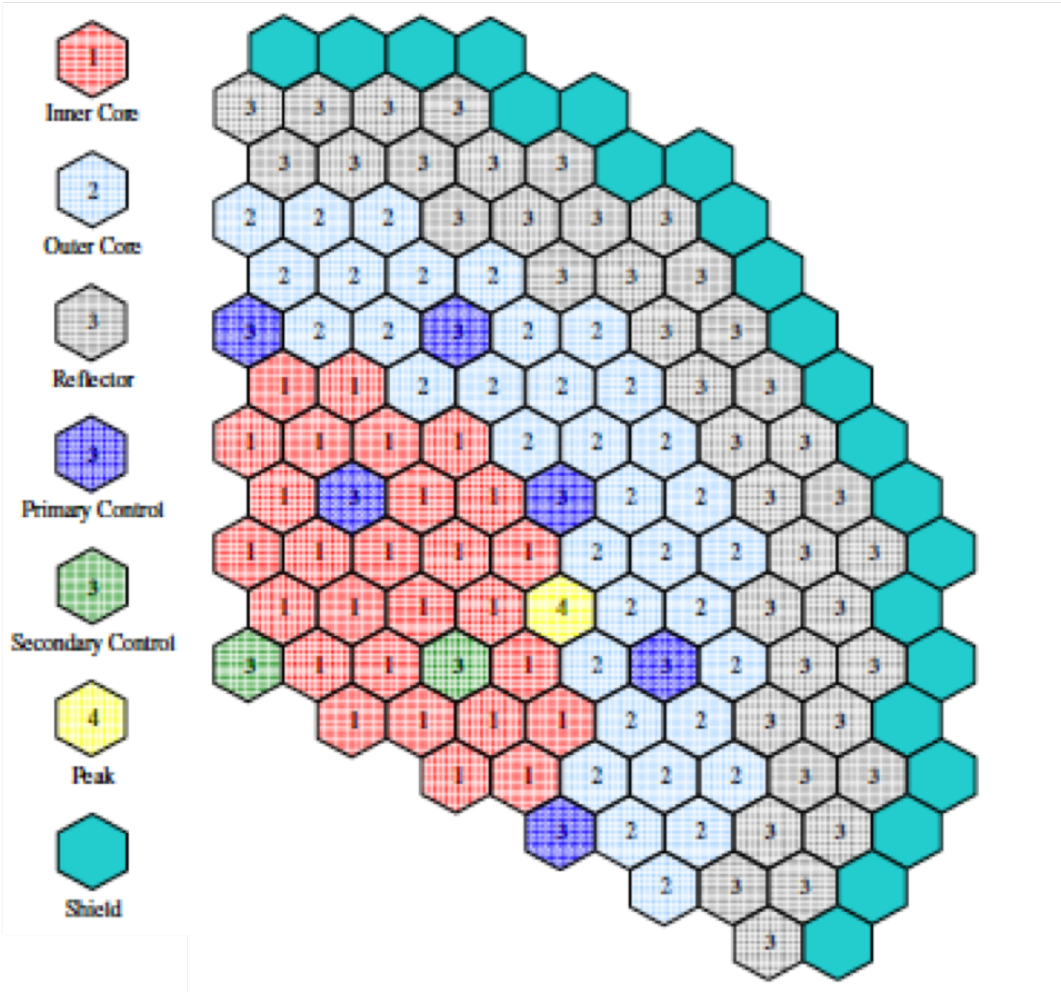

Figure 50: Grouping of assemblies into channels for the transient model of the ABR core.

7.2 Transient Initiators and Assumptions

Three different transients are examined in this study – the (1) Unprotected Loss of Heat Sink (ULOHS), (2) Unprotected Loss of Flow (ULOF), and (3) Unprotected Transient Overpower (UTOP). For all three transients, the core begins at its initial steady-state conditions, as outlined in Section 6. The assemblies in Channels 1 and 3 are assumed to have a closed fuel-clad gap due to their high power, while the gap in Channel 2 is still open at the start of the transient. The core shutdown system is assumed to fail and a single DRACS loop designed for capacity of 0.5% of core power is passively engaged by opening the dampers on the NaK-to-air heat exchanger immediately upon transient initiation. The ambient air temperature for the heat exchanger is assumed to be 27°C. The second DRACS loop is assumed to fail. The assumptions that differ between the three transient scenarios are outlined in Table 10.

In the ULOHS, heat rejection through the steam generators is assumed to immediately cease, with core flow remaining at nominal and thermal stratification assumed to be negligible. In the ULOF, the pump motors are assumed to trip and core flow decreases with the impeller inertia until reaching a lower threshold value, at which time the rotors are assumed to lock in place and the transition to natural circulation occurs. The same flow halving time of 20 s is assumed for all pumps, both primary and intermediate. Because of the severe decrease in flow as the transient progresses, thermal stratification models for the cold and hot pools are used. In the UTOP, a reactivity insertion equivalent to the worth of an average-rod is withdrawn, with full flow and no thermal stratification assumed. The rate of control rod withdrawal is assumed to be 0.005 $/s, as was used in the safety analysis for the IFR [28]. In both the

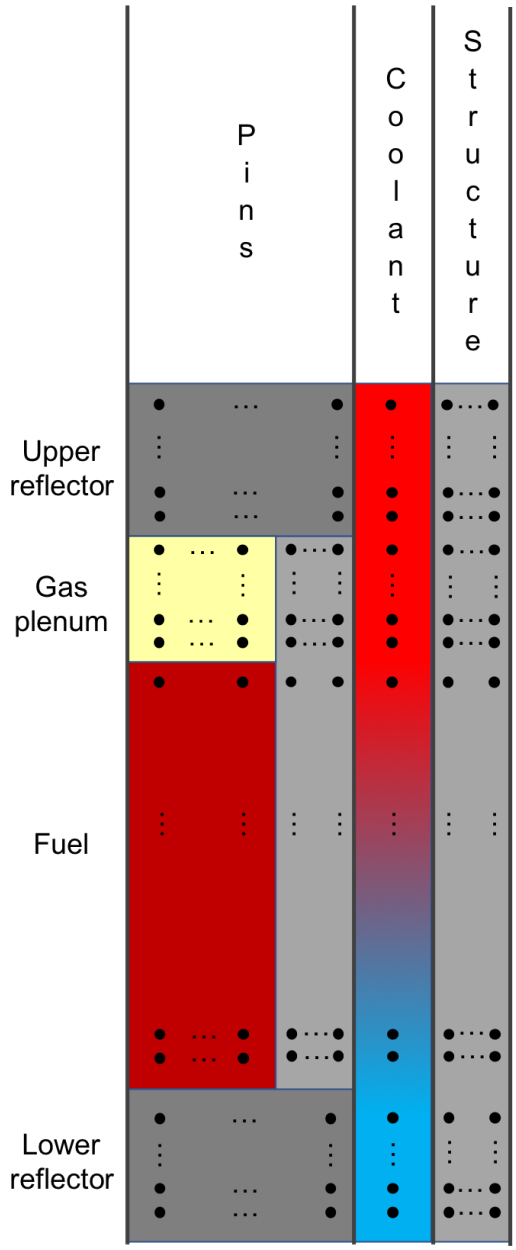

Figure 51: Channel model used to represent the core heat transfer in the transient model.

ULOF and UTOP, the steam generator outlet temperature is assumed to remain constant.

7.3 Nominal performance

Transient performance is shown in Figures 52-54 for all three accident scenarios in the ABR. It can be seen that all three scenarios display acceptable performance, with no coolant boiling or fuel melting experienced. In general, the transient behavior is seen to be smooth and slowly-varying.

The ULOHS scenario monotonically approaches a new low-power steady-state with elevated coolant temperatures resulting from the increase in coolant inlet temperature. Because the ULOHS is driven by coolant temperatures, strong radial expansion and control rod driveline feedbacks provide rapid negative reactivity insertions, which are adequate to overcome the positive coolant void and doppler reactivity insertions for the entire duration of the transient.

Table 9: Nodalization of the core channel model for the ABR.

Region	Axial Nodes	Radial Nodes
Upper Reflector	5	2
Gas Plenum	4	1
Fuel	20	10
Cladding	20	3
Coolant	34	1
Structure	34	2
Lower Reflector	5	2

Table 10: Assumptions specific to each of the three transients examined in the ABR core.

	ULOF	ULOHS	UTOP
Primary Loop Heat Rejection	Nominal	Zero	Nominal
Pump Speed	20 s halving time	Nominal	Nominal
Control System	No scram	No scram	\$0.75 inserted at 0.005 \$/s
Thermal Stratification	Cold and hot pools	None	None

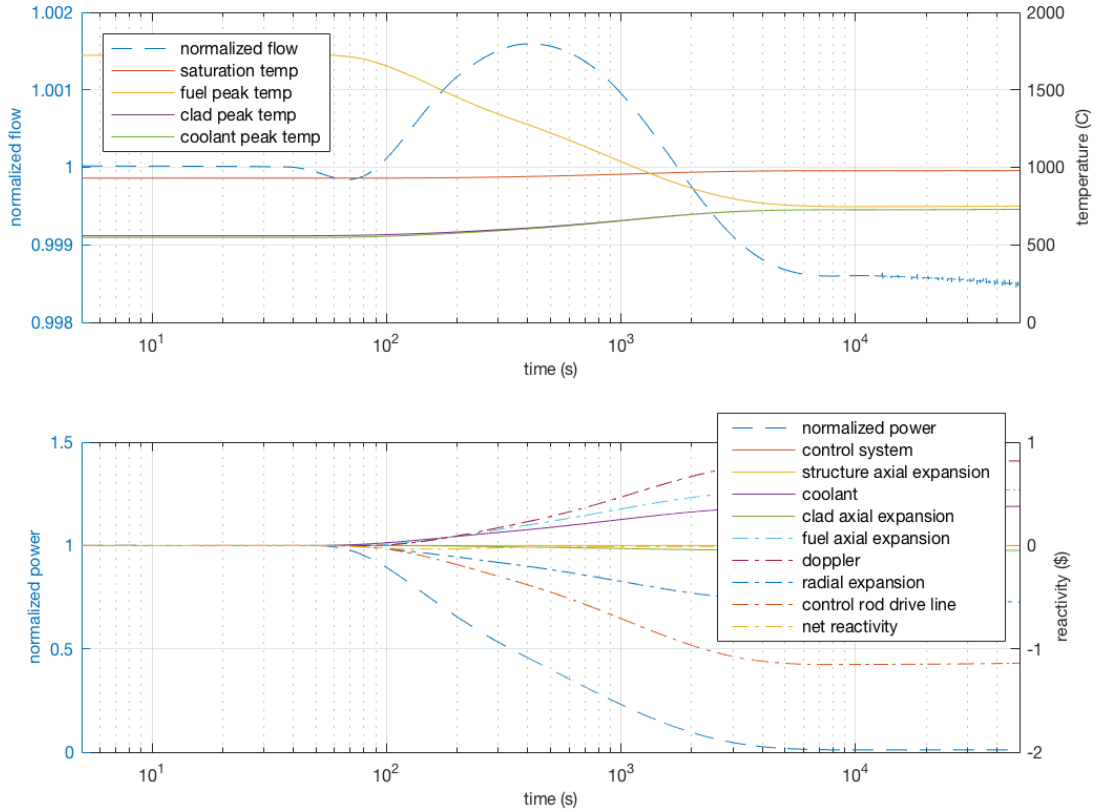

Figure 52: Response to a ULOHS accident in the nominal oxide ABR core.

The UTOP scenario is initiated by a sudden constant withdrawal of an average-worth rod, which

ends at approximately 160 s. During the initial transient phase, the behavior is monotonically increasing power up to nearly 150%, with fuel doppler and axial expansion feedbacks providing the main negative reactivity insertions and coolant feedback providing the only positive insertion apart from the control rod withdrawal. Initially control rod driveline feedback is slow to act, as the UTOP scenario is driven by fuel temperatures which must be communicated through the fuel to the coolant and then to the control rod drives themselves. Because the thermal conductivity of oxide fuel is low, the high fuel temperatures are slow to be communicated to the control rod drives. However, when the rod withdrawal sequence is complete, the other feedbacks are able to catch up and provide enough negative reactivity to turn the net reactivity temporarily negative. Eventually as the core barrel heats up, the control rod driveline feedback decreases, which allows power to again increase until leveling off at near 150%. Because coolant flow rates remain at nominal levels, this increased power causes a strong increase in fuel temperature, although no fuel melting is seen to occur.

The ULOF behavior is initially smooth and monotonic as well. As the flow decreases, net reactivity immediately turns negative as radial expansion and control rod driveline feedbacks easily overcome the coolant and sluggish doppler insertions. This leads to a strong power decrease as flow is decreasing. However, small oscillations in the ULOF scenario are seen to occur as a result of the transition from forced flow to natural circulation, which causes a sudden drop in flow rate and resulting temperature-reactivity oscillations. These oscillations are damped, however, and no negative impacts result from this period of oscillations. Throughout the ULOF, the mismatch between power and flow is significant, leading to an increase in coolant and cladding temperatures.

A summary of peak temperatures for all three scenarios is given in Table 11. It is seen that, although fuel melting does not occur, the UTOP scenario is likely very close to fuel melting. Given the uncertainties in thermal conductivity of oxide fuel that has seen significant burnup, it is desirable to increase this margin if possible. Additionally, while no coolant boiling is seen to occur, the ULOF scenario is closest, with only 130 °C margin. This margin should also be increased, if possible, to allow for higher confidence in the passive safety characteristics of the ABR core.

Table 11: Peak transient temperatures in the nominal transients of the ABR reference core.

	Peak coolant temperature (°C)	**Peak fuel temperature (°C)**	**Margin to boiling (°C)**	**Margin to fuel melting (°C)**
ULOHS	728	1723	251	1027
UTOP	657	2702	298	48
ULOF	894	1722	130	1028

7.4 Performance with ARC inclusion

With the baseline performance established, the transient models were altered to include the ARC system response. This entailed extending the core channel heights to include the lower and upper ARC system reservoirs, the addition of thermal inertia to represent the additional mass of the ARC system reservoirs, and the addition of control system logic to represent heat transfer from the coolant to the ARC system upper reservoir and subsequent actuation of the ARC system.

With these modifications made, a parametric study over the ARC system design variables was performed. To tune the performance of ARC systems, a number of parameters may be modified including: lithium enrichment, ARC tube diameters, distances between system reservoirs and the active core, volumes of reservoirs, and pressures of system fluids. These different design choices combine into three parameters which can be modified for a particular ARC system, over which the parametric study is performed: (1) the total system worth (w), (2) the coolant temperature difference above nominal at which the ARC system begins to actuate (ΔT_{act}), and (3) the coolant temperature span over which the ARC system is

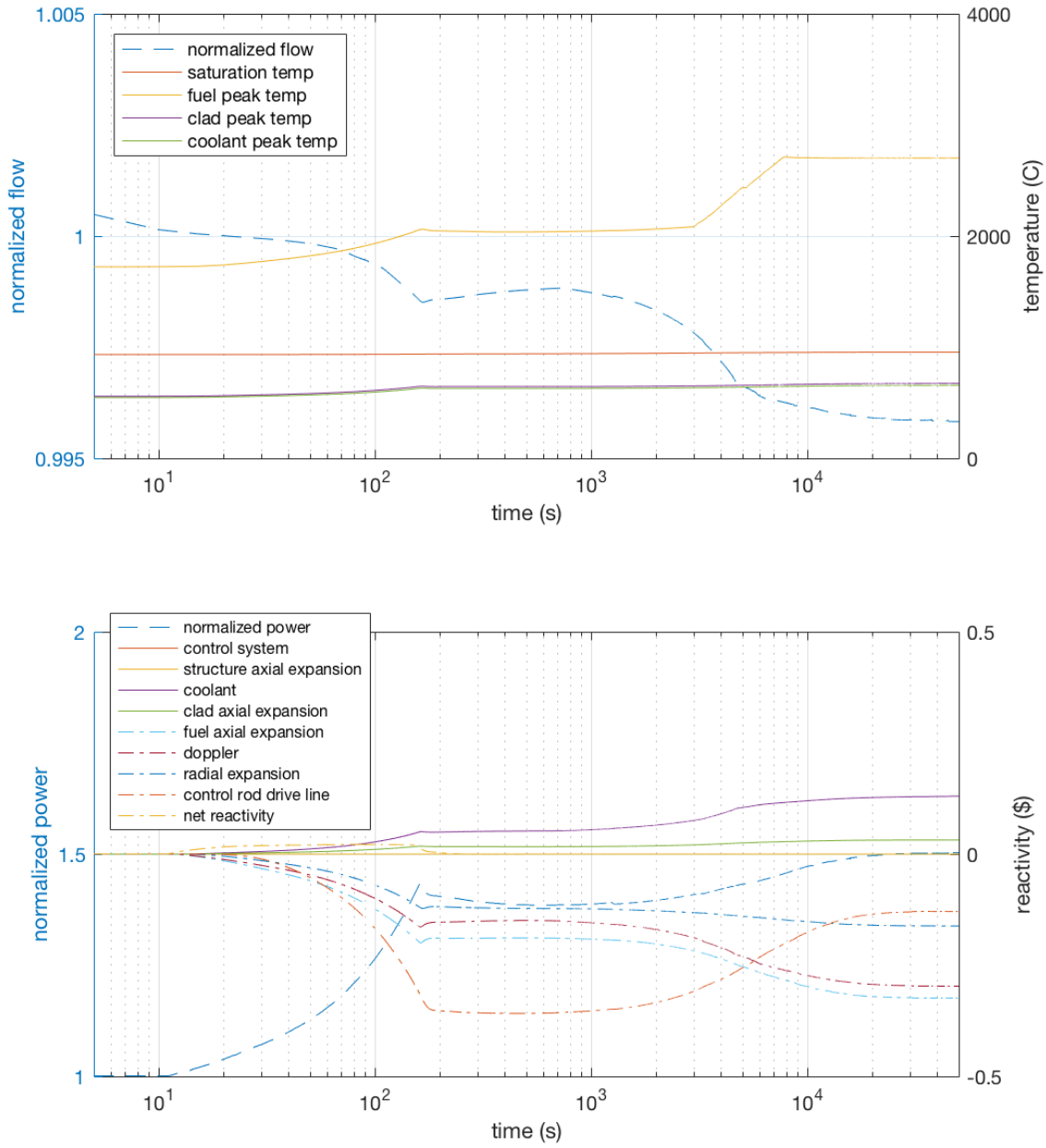

Figure 53: Response to a UTOP accident in the nominal oxide ABR core.

fully actuated (S). The impact of each design choice can span more than one of the three parameters. For instance, the ARC tube diameters, distances between reservoirs and active core, and system pressure may all impact S, but they also may have impacts on ΔT_{act}. The relation between these variables is outlined in [29].

Results of the parametric study are shown in Figure 55 for the case of $S = 65°\text{C}$ in terms of the margin to coolant boiling that is gained over the nominal transient case. From Figure 55 it can be seen that the greatest margin gained is in the ULOF scenario, which initially had the worst performance in the

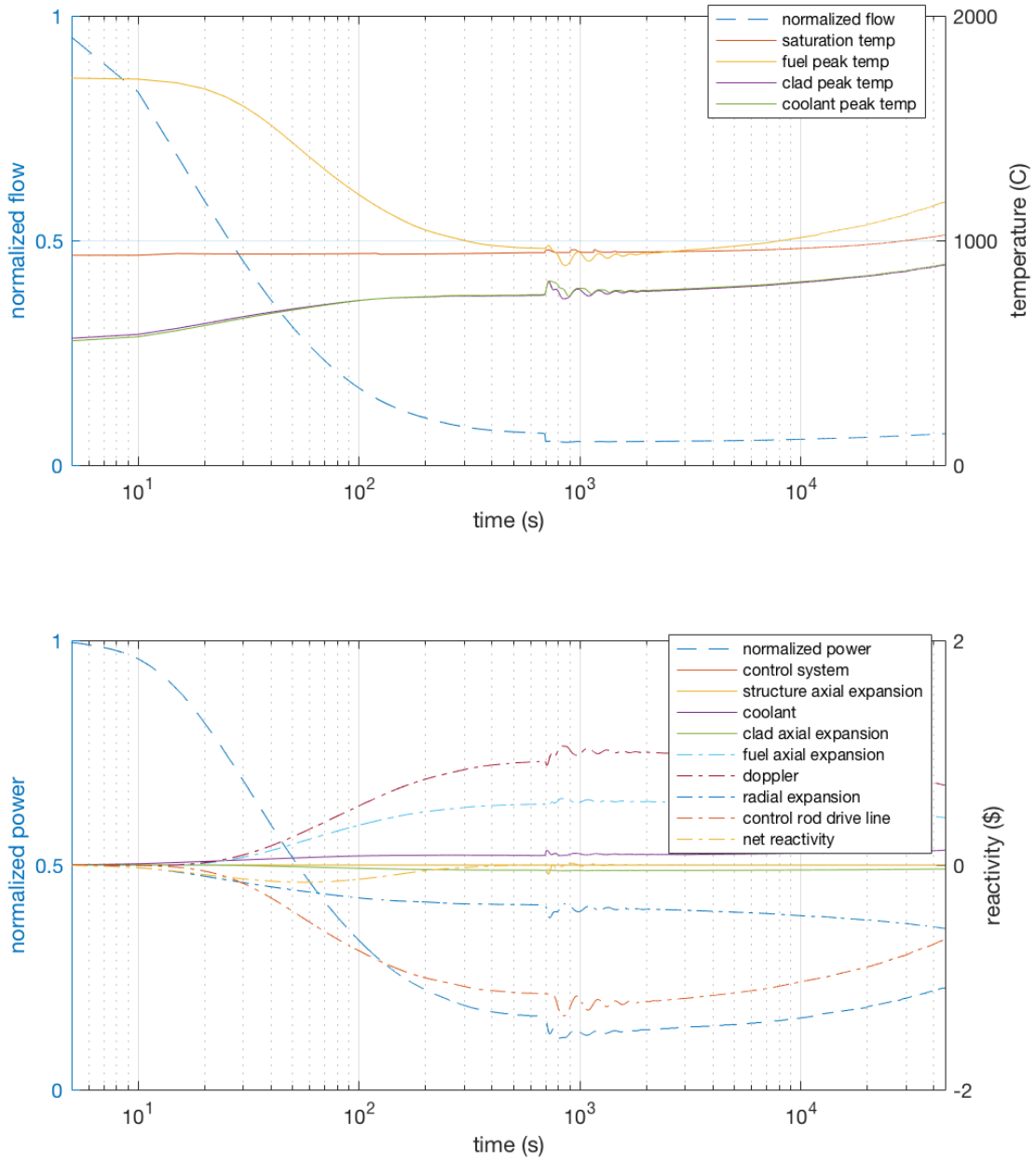

Figure 54: Response to a ULOF accident in the nominal oxide ABR core.

transient without ARC system inclusion. The smallest gains are for the UTOP scenario, although still substantial gains of more than 60°C are realized. The response surfaces are generally smooth for all three transient scenarios except at high w, where the ARC response is so strong that oscillations are induced, which eventually leads to coolant boiling in the ULOF and UTOP. In order to maximize the transient benefits, it is apparent that the ARC system should be designed to have high worth, although not so high as to induce oscillations. Figure 55 also shows that the ARC system design is most sensitive to increasing w, while the results do not change appreciably with increasing ΔT_{act}. Because ΔT_{act} may be lower-bound

limited by capillary forces in very small diameter tubes, it may be necessary to increase ΔT_{act} slightly, although this should not be detrimental to the ARC system performance due to the small sensitivity.

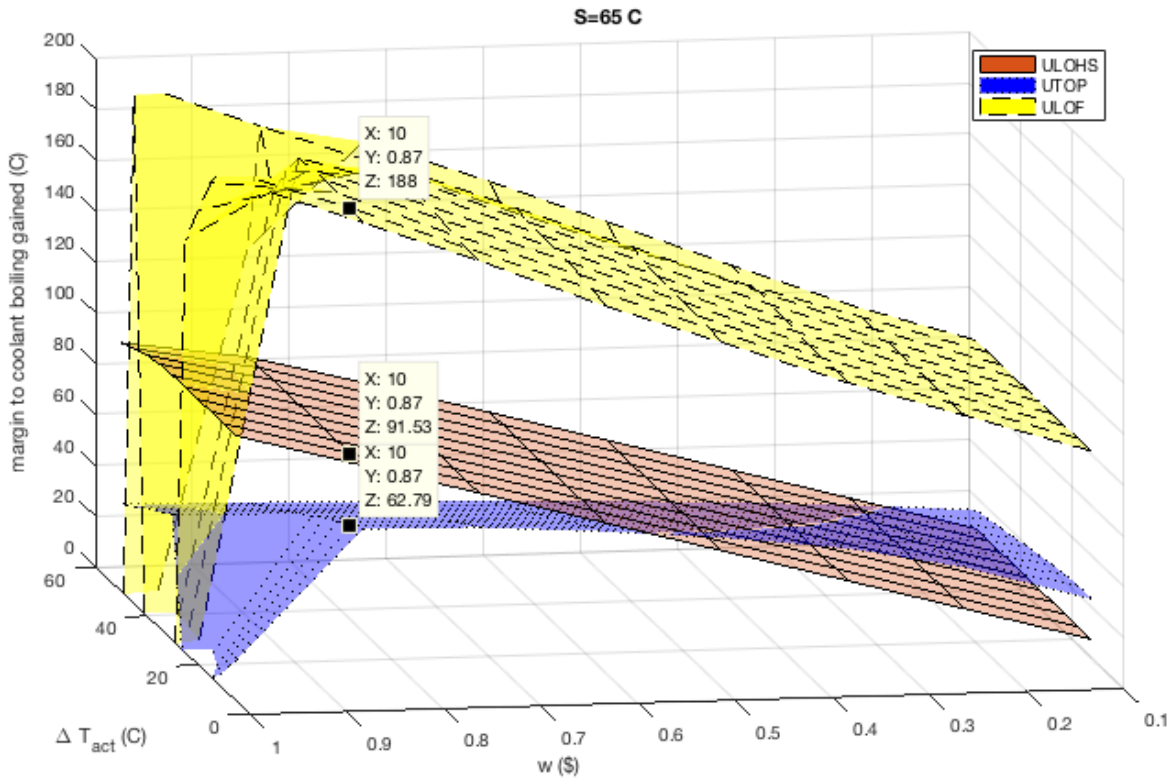

Figure 55: Margin to coolant boiling gained during each transient as a function of w and ΔT_{act} for $S = 65°C$.

While Figure 55 shows the parametric study for the slice at $S = 65°C$, the parametric study was performed at other values of S as well. Figure 56 shows a summary of the variation with S for the specific case of $w = \$0.87$ and $\Delta T_{act} = 10°C$. The sensitivity to S in the ULOHS and ULOF is very slight, but the UTOP shows a much stronger trend. A local maximum is seen to occur at $S = 65°C$, and therefore the optimal ARC design for the oxide ABR is chosen to be $S = 65°C$, $w = \$0.87$, and $\Delta T_{act} = 10°C$.

A summary of the results with this specific ARC design is given in Table 12. Substantial gains in margin to coolant boiling are gained in all three transient scenarios, with the largest gains of nearly 200°C in the ULOF. Still, however, the highest coolant temperatures occur in the ULOF as a result of the power-to-flow mismatch. Large margin to fuel melting is gained in the UTOP as well, with fuel temperatures brought down to be more on par with those of the other transients. These results demonstrate significant safety benefits of including ARC systems into the oxide ABR core.

7.5 Suppression of Oscillations in the ULOF

Although the behavior of the ULOF scenario is greatly improved by including ARC systems, a set of oscillations are induced in addition to those which result from the transition from forced to natural circulation. Figure 57 shows the ULOF response with the optimal ARC system included during the early phase of the transient as flow is rapidly reducing, where a set of three oscillations are seen in the temperature-reactivity response. These oscillations are not excessively large and do not grow, and are therefore deemed as acceptable. However, the rapid changes in temperature could introduce stress in

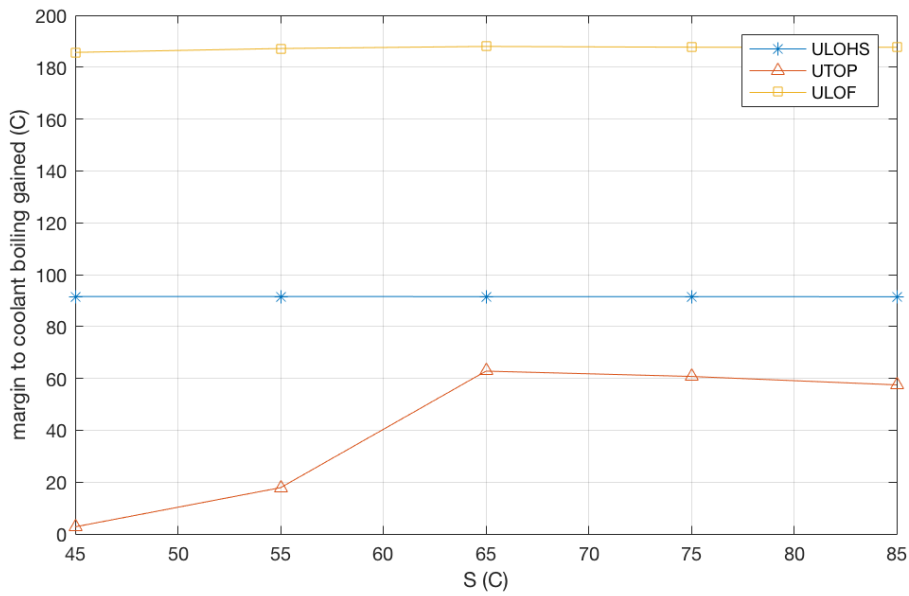

Figure 56: Margin to coolant boiling gained as a function of S with $w = 0.87\$$ and $\Delta T_{act} = 10°\text{C}$.

Table 12: Margin to coolant boiling gained over the reference design through optimal ARC system inclusion.

	Peak coolant temperature with ARC (°C)	**Peak fuel temperature with ARC (°C)**	**Margin to boiling gained (°C)**	**Margin to melting gained (°C)**
ULOHS	636	1724	92	0
UTOP	593	1910	63	792
ULOF	707	1724	188	0

core components, and therefore the source of the oscillations should be understood so that they may be avoided.

The strongest reactivity oscillations are seen in the ARC component, implying that the ARC system is the source of the temperature oscillations. To investigate what aspect of the ARC response leads to the oscillations, a study was performed where different parameters of the ARC system are successively increased to decrease the sensitivity of the ARC system to small fluctuations in temperature. Figure 58 depicts the ARC reactivity as a function of time for increasing values of S. It is seen that as S is increased, the oscillations smooth out and eventually are avoided altogether. This modification results in a slower, smoother reactivity insertion, allowing for temperature oscillations to be avoided while still providing the safety benefits of including the ARC system.

Figure 59 shows a similar plot, where τ is successively increased. A similar smoothing effect is seen as τ is increased, and eventually the oscillations can be eliminated completely.

The reason for this behavior is that increasing S or τ allows for the the ARC system to be less strongly coupled to fluctuations in core temperature. Too strong of coupling leads to strong ARC system response, and subsequently overcompensation by the other feedbacks. But as the coolant flowrate continues to decrease, the driving force for the transient continues, causing another strong actuation. This process repeats, leading to temperature oscillations if the ARC system response is too tightly coupled to core temperatures. Therefore, if it is desired to remove the oscillations, some method of dampening the feedback

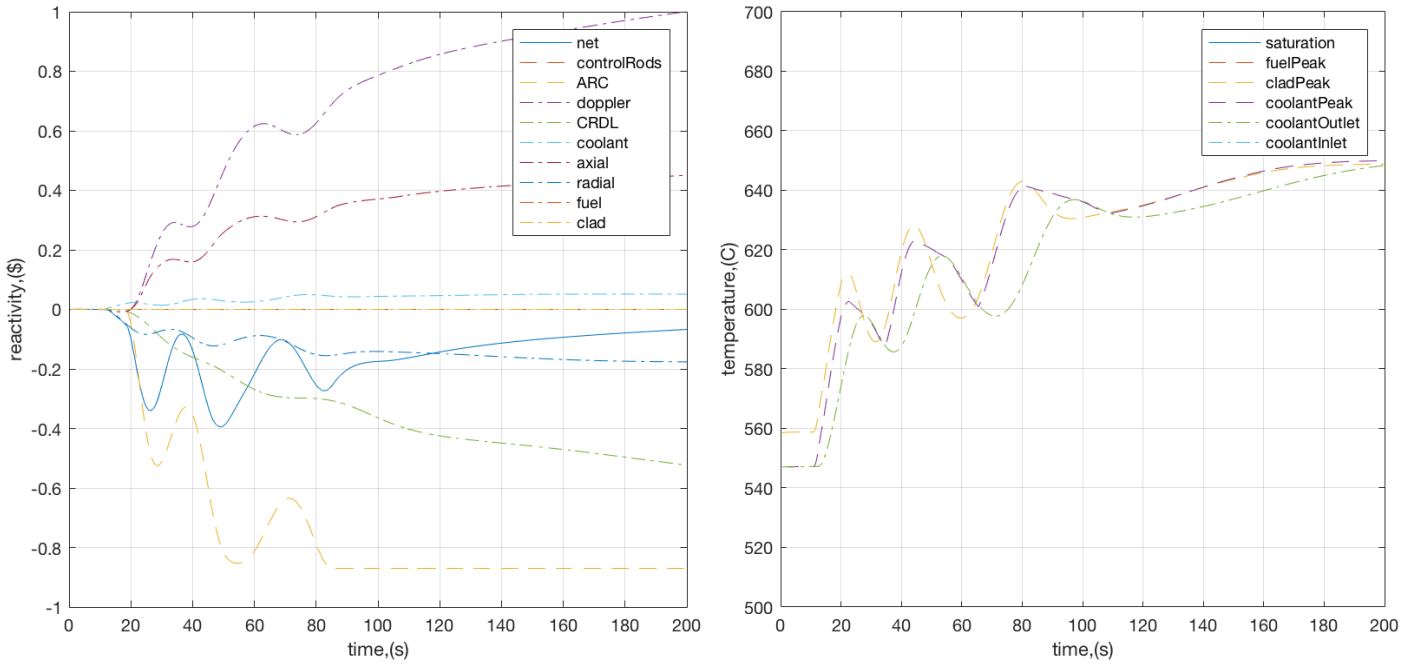

Figure 57: Transient response during the early phase of a ULOF accident in the oxide ABR equipped with an ARC system of $S = 65$ C, $w = \$0.87$, and $\Delta T_{act} = 10$ C.

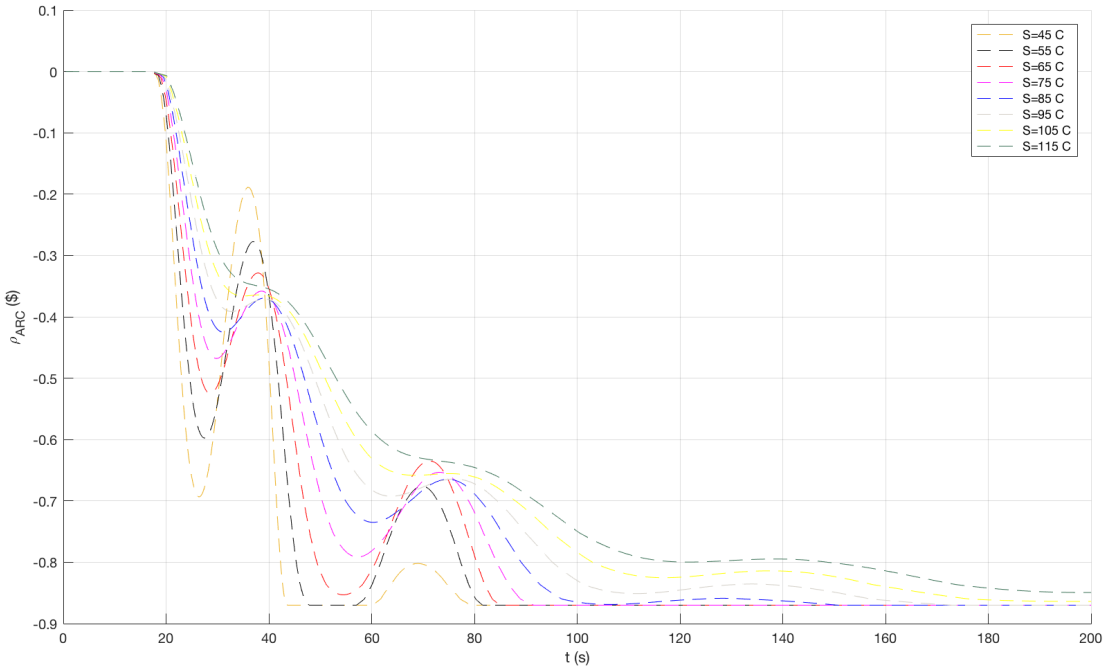

Figure 58: Reactivity inserted by the ARC system into the oxide ABR during the ULOF transient with increasing actuation span, S. $w = \$0.87$ and $\Delta T_{act} = 10$ C.

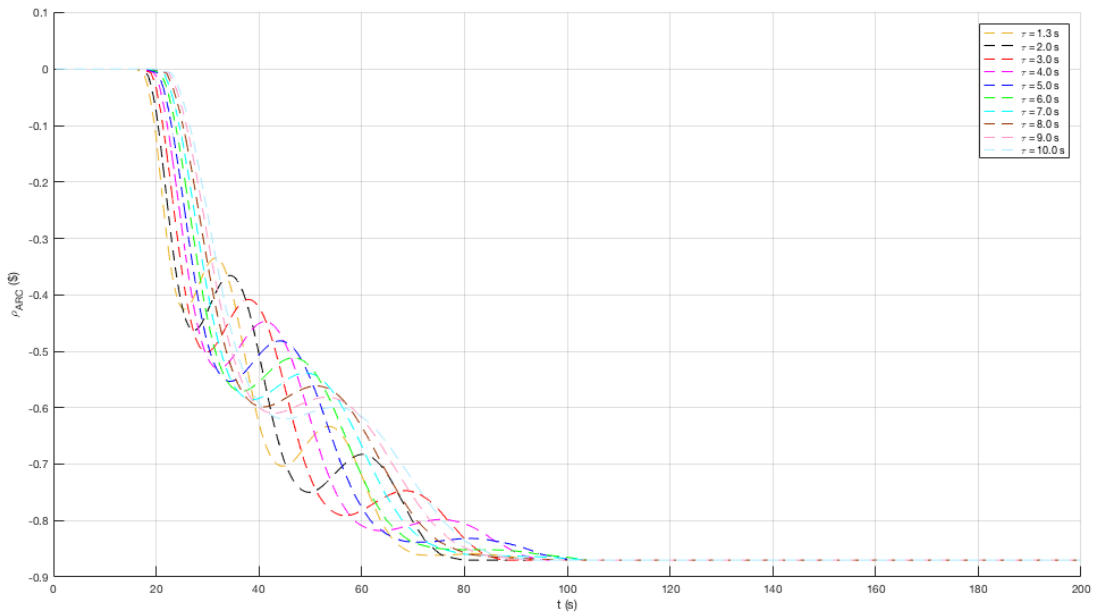

Figure 59: Reactivity inserted by the ARC system into the oxide ABR during the ULOF transient with increasing heat transfer resistance from coolant to upper reservoir. $w = \$0.87$, $S = 65$ C, and $\Delta T_{act} = 10$ C.

loop between core temperatures and ARC response should be employed, such as increasing S or τ as demonstrated above. However, the system should not be completely decoupled, as then the ARC system actuation will be too slow to be effective in arresting the transient. Ideally, the coupling should be only in one direction, from the coolant temperatures to the ARC system reservoir. This insight is utilized in Section 8 in the analysis of ARC systems for the second reference core.

7.6 Summary of Results

Although the ABR core was able to achieve passive safety without ARC system inclusion, the addition of the ARC system allowed for significant safety margin to be gained. By incorporating the ARC system, all three transients were improved, with the largest gains obtained for the peak coolant temperature in the ULOF and the peak fuel temperature in the UTOP. Although small temperature-reactivity oscillations were observed in the ULOF response when the ARC system was added, methods for mitigating this potential issue were proposed and found to be effective. Therefore the inclusion of ARC systems into the oxide ABR is viewed as potentially very beneficial.

8 Performance of the B&B core

8.1 Transient Model

The transient model of the B&B core was created by modifying the ABR model to reflect the differences between the two cores. Assemblies were grouped into 7 representative channels for the simulation, as depicted in Figure 60. Fuel assemblies were grouped into 4 channels to capture the power gradient across the core, with two additional channels devoted to the peak-power and peak power-to-flow assemblies to capture peak temperatures during the transient. A final channel was allocated for reflector and control assemblies.

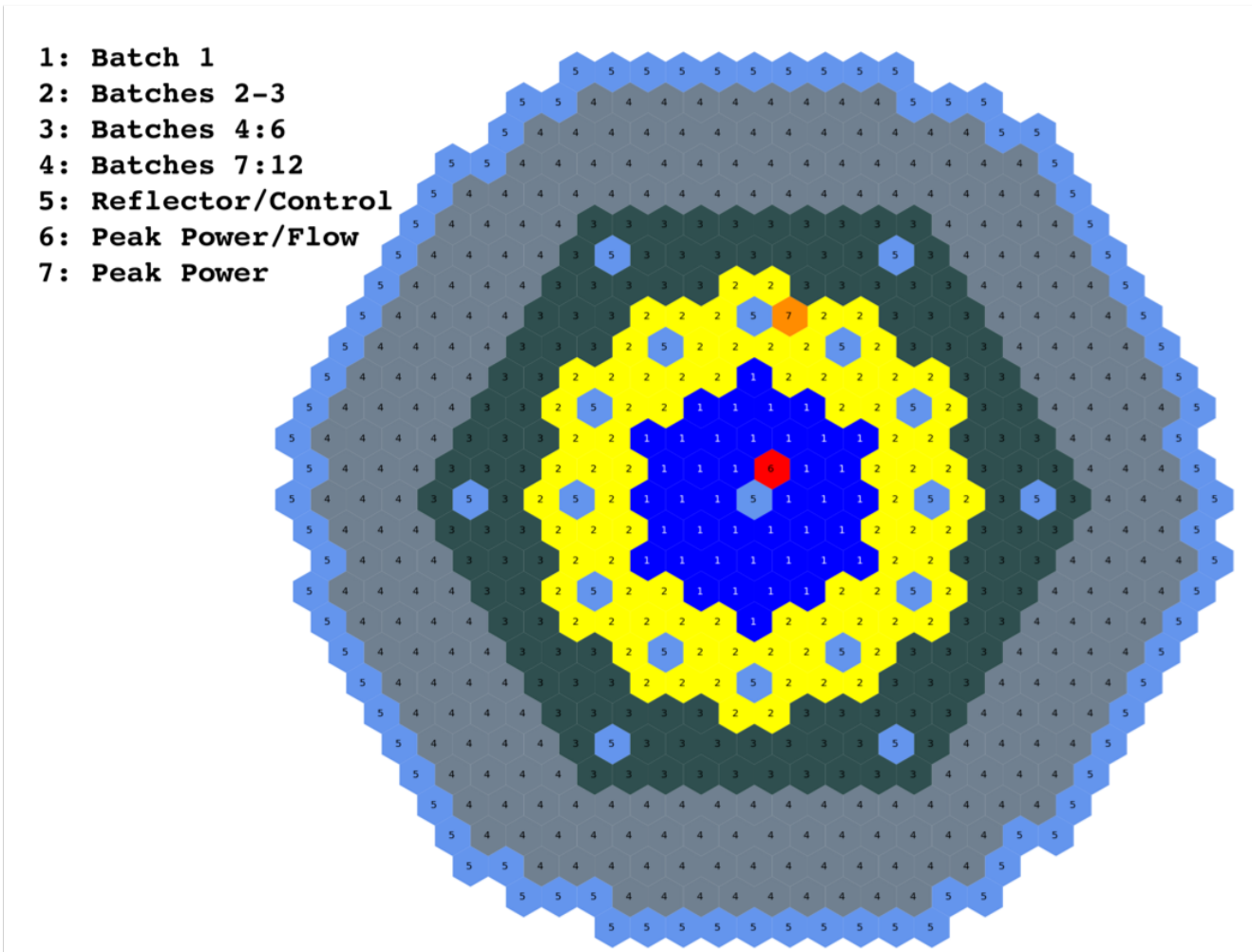

Figure 60: Grouping of assemblies into channels for the transient model of the B&B core.

The core channel model for the B&B core is very similar to that used for the ABR as shown in Figure 51, with more axial segments added to capture the sharper gradients in core characteristics. Table 13 provides the nodalization used.

The reactivity feedback models are the same as outlined in Section 7. Although calculated for the ABR geometry, $\tau = 1.3$ s was again assumed for the B&B core.

8.2 Transient Initiators and Assumptions

The same three transients are again studied for the B&B core. Due to the rapid swelling of metallic fuel at low levels of burnup, all channels are assumed to have closed fuel-clad gaps. The core shutdown system is

Table 13: Nodalization of the core channel model for the BnB core.

Region	Axial Nodes	Radial Nodes
Upper Reflector	5	2
Gas Plenum	4	1
Fuel	26	10
Cladding	26	3
Coolant	40	1
Structure	40	2
Lower Reflector	5	2

assumed to fail and a single DRACS loop designed for capacity of 0.5% of core power is passively engaged by opening the dampers on the NaK-to-air heat exchanger immediately upon transient initiation, with an ambient air temperature of 27°C. The assumptions specific to the three transient scenarios are similar to those of the ABR, and are outlined in Table 14.

Table 14: Assumptions specific to each of the three transients examined in the B&B core.

	ULOF	ULOHS	UTOP
Primary Loop Heat Rejection	Nominal	Zero	Nominal
Pump Speed	20 s halving time	Nominal	Nominal
Control System	No scram	No scram	$1.66 inserted at 0.005 $/s
Thermal Stratification	Cold and hot pools	None	None

8.3 Nominal Performance

Due to a very strong positive coolant reactivity feedback, the transient performance in the B&B core without ARC system inclusion is poor. Both the ULOF and UTOP transients are seen to boil within 20 minutes. Results of the ULOHS are given in Figures 61 - 63. From examining the reactivity feedbacks of Figure 62, it can be seen that the coolant feedback dominates the response and keeps the net reactivity near zero for much of the transient, even as the majority of feedbacks are negative.

The other transients are similarly hindered by the strong coolant feedback. The reactivity evolution in the ULOF and UTOP scenarios are presented in Figures 64 - 65. In the ULOF, the transition from forced- to natural-circulation at 1000 s leads to a sudden spike in coolant temperature, which is reflected in the large positive reactivity insertion which leads to boiling. In the UTOP, the coolant feedback acts nearly as strongly as the insertion due to the control rod withdrawal, resulting in a consistently positive net reactivity until boiling occurs around 150 s. A summary of the nominal transients is provided in Table 15. This transient performance is unacceptable from the perspective of passive safety, and therefore provides ample opportunity for improvement through the inclusion of ARC systems. As demonstrated, the main challenge for the ARC system will be to overcome the strongly positive coolant reactivity feedback.

Table 15: Time of boiling initiation in the B&B core without ARC system inclusion.

	ULOHS	**ULOF**	**UTOP**
Time of boiling (s)	-	1284	150

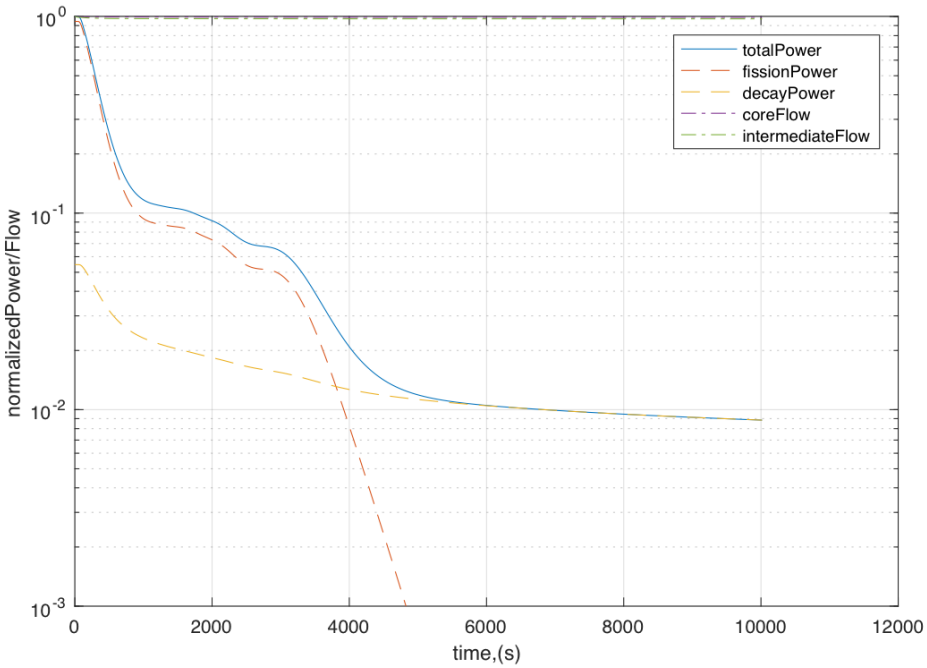

Figure 61: Power and flow with time for the ULOHS scenario in the B&B core without ARC system inclusion.

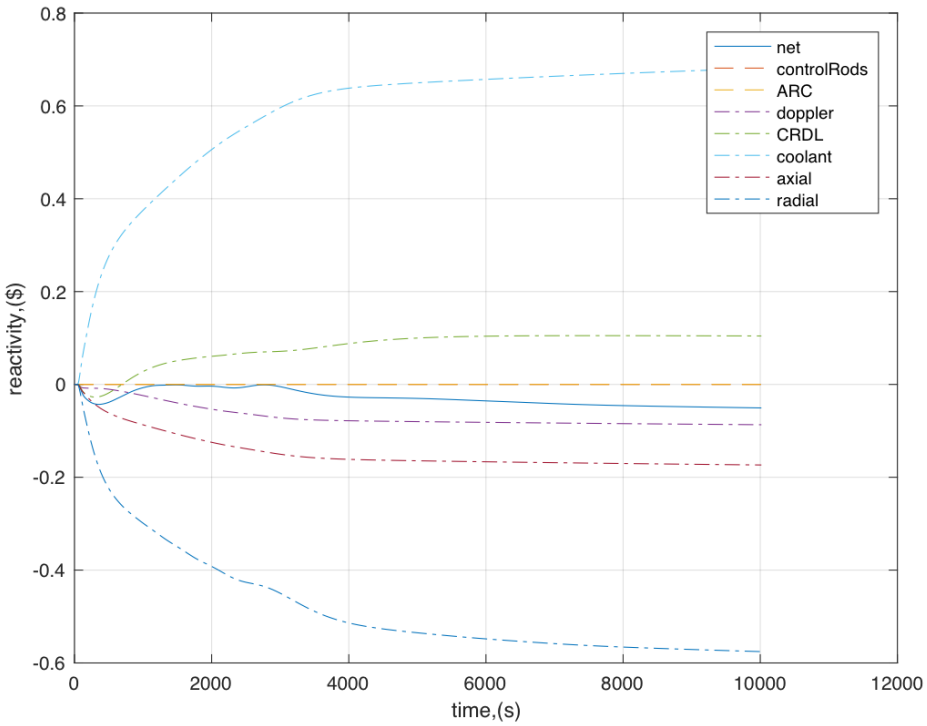

Figure 62: Reactivity feedbacks with time for the ULOHS scenario in the B&B core without ARC system inclusion.

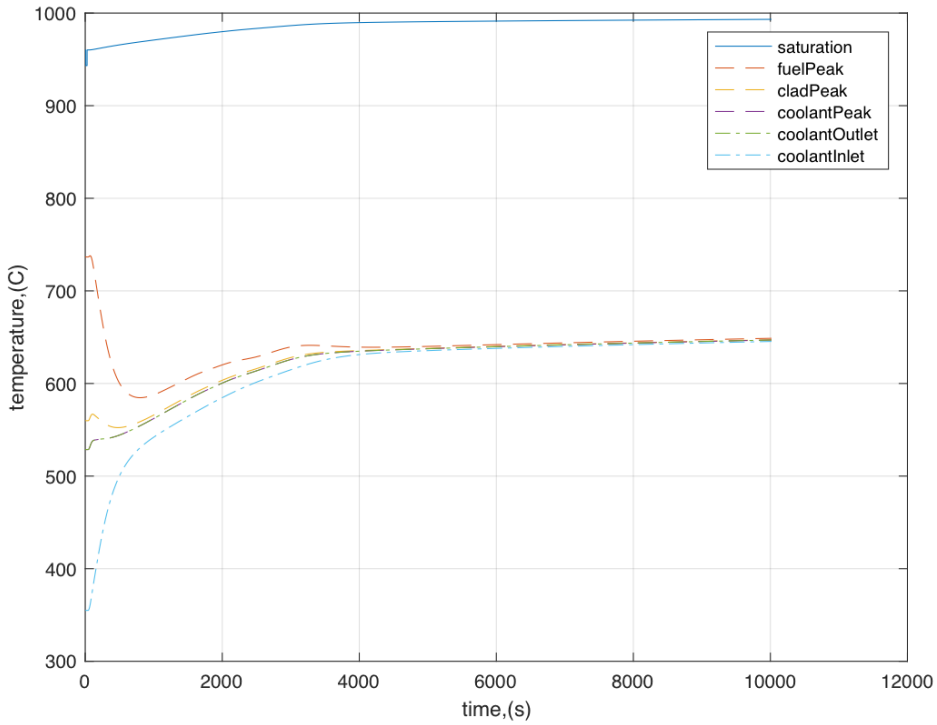

Figure 63: Core temperatures with time for the ULOHS scenario in the B&B core without ARC system inclusion.

8.4 Nominal Performance Sensitivity Studies

To evaluate the impacts of model assumptions on the transient performance, a few sensitivity studies were performed, as outlined in the following subsections.

8.4.1 Pump Coast Down Time

One assumption that has a large impact on the ULOF scenario is the inertia of the primary pumps, which impacts the flow halving time. The nominal scenario assumes the pump coast down halving time to be the same as that for the oxide ABR core, 20 s. This value could be changed in practice either by selecting a different pump or by modifying the pump with flywheels to increase their inertia. To evaluate the sensitivity to pump inertia, a study was performed in which the pump coast down time was parametrically varied away from 20 s. Figure 66 shows the time of boiling initiation in the ULOF scenario as a function of primary pump coast down time. It is noted that boiling is encountered with all of the examined coast down times. However, increasing the coast down time can push off boiling by a few minutes, if larger halving times are able to be physically realized. The two jumps shown in Figure 66 result from the transient progressing slowly enough for the control rod driveline and the radial expansion feedbacks to play effective roles in delaying the runaway boiling behavior. Regardless, the nominal ULOF performance is very poor even with increased coast down times due to the oscillatory behavior set off by the transition from forced- to natural-circulation.

8.4.2 Control Rod Driveline Feedback

Another uncertain parameter that has an impact on boiling time is the strength of the control rod driveline feedback. Figure 67 shows the time of boiling in the ULOF and UTOP as a function of the control rod

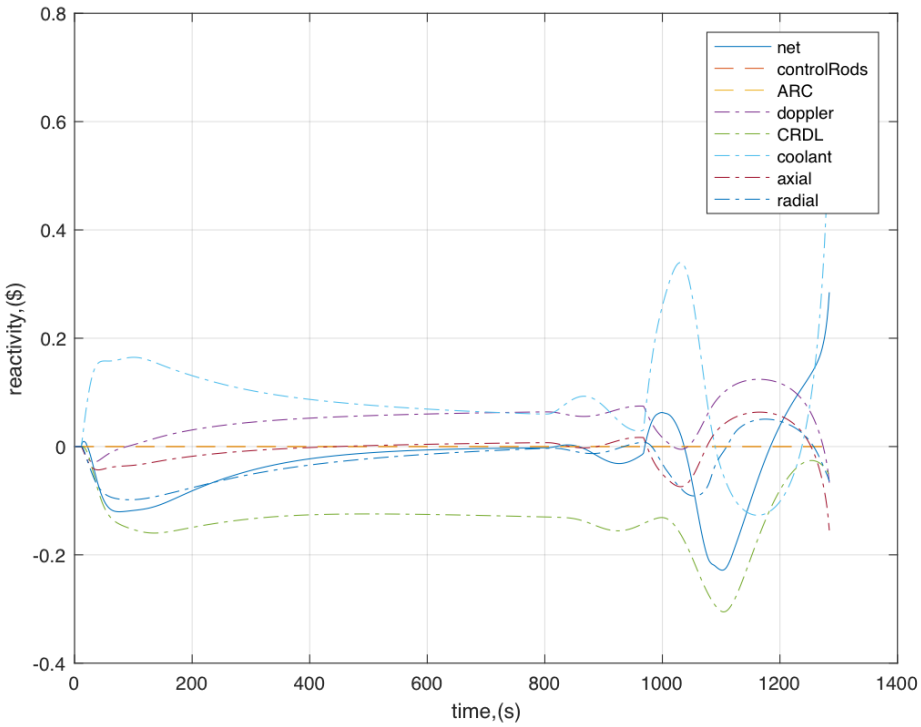

Figure 64: Reactivity feedbacks with time for the ULOF scenario in the B&B core without ARC system inclusion.

drive thermal expansion coefficient. As the expansion coefficient gets larger, the rods are inserted further into the core for a given change in outlet temperature, implying a stronger feedback mechanism. The trend for the UTOP scenario is similar to the sensitivity to the flow-halving time. As the control rod driveline feedback increases in strength, the time of boiling can be pushed off, although never by more than a few minutes. However the trend in the ULOF case is less clear, showing limited improvement by increasing the control rod driveline feedback. Again though, no realistic increases in control rod driveline are able to prevent boiling in either the ULOF or UTOP.

8.4.3 Rate of Reactivity Insertion

Another sensitivity study was performed on the rate of reactivity insertion in the UTOP event. Because sodium reactors are operated near atmospheric pressure, control rods are not rapidly ejected as in light water reactors. Instead, the speed of control rod withdrawal during a UTOP event is largely a result of the control rod drive motor design. The nominal value of 0.005 $/s was taken from studies of the Integral Fast Reactor (IFR) [28], although in reality this can be viewed as a psuedo design parameter. Figure 68 shows the time of boiling in the UTOP as the reactivity insertion rate is varied by 20%. The results indicate that reducing the insertion rate makes a minimal impact, with boiling pushed off by less than a minute. In addition, Figure 68 shows the impact of assuming a constant rate of reactivity insertion versus a constant rate of withdrawal. While many studies make the simplifying assumption that reactivity is added at a constant rate during a UTOP, in reality the velocity of rod withdrawal is constant and the rate of reactivity insertion varies according to the differential rod-worth curve. By considering the variation of reactivity insertion with time, the time of boiling worsens, but only marginally. No matter, boiling still occurs within only a couple of minutes of transient initiation with all examined reactivity insertion rates.

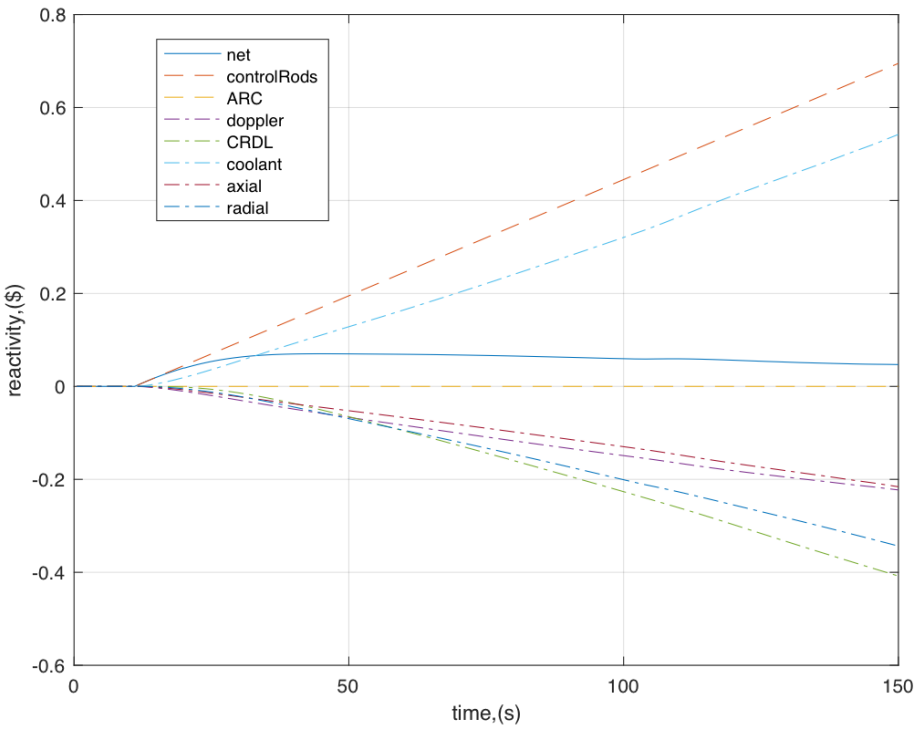

Figure 65: Reactivity feedbacks with time for the UTOP scenario in the B&B core without ARC system inclusion.

8.4.4 Locked Rotor Loss Coefficient

It was seen that boiling in the ULOF is caused by the transition from forced- to natural-circulation, when a sudden drop in flow rate is seen. This transition from forced- to natural-circulation occurs when the pump impellers have so little inertia that they suddenly lock in place due to friction. Following rotor-locking, flow through the pump must traverse past the locked rotor, which partially blocks the flow passage and causes a pressure loss. This added pressure loss is the cause of the sudden drop in flow during the flow transition, and the magnitude of the drop is dependent on the pressure loss induced by the pump. Because this induced pressure loss may vary in practice, a final sensitivity study was performed on the loss coefficient of the pump under locked-rotor conditions. Figure 69 shows the time of boiling as the loss coefficient of the primary pump is reduced from its nominal value of 2.5 (the same as the ABR). As the loss coefficient is reduced, the time of boiling increases significantly until eventually boiling is avoided altogether for coefficients of less than 0.9. Such low loss coefficients allows for the magnitude of the sudden flow decrease to be reduced, which then reduces the strength of the sudden coolant reactivity insertion, as shown in Figure 70. Although this study has shown that boiling can be avoided altogether by reducing the loss coefficient sufficiently, it is not clear that such small loss coefficients can be achieved in reality. However, this study has revealed one of the primary mechanisms by which boiling is induced in the ULOF scenario.

8.5 Performance with ARC inclusion

A similar parametric study as the one performed in the ABR core was repeated for the B&B core. The design space for improving the ULOHS without inducing oscillations was found to be very large. Figure 71 shows the results of the parametric study in the ULOHS in terms of margin to boiling gained over the case

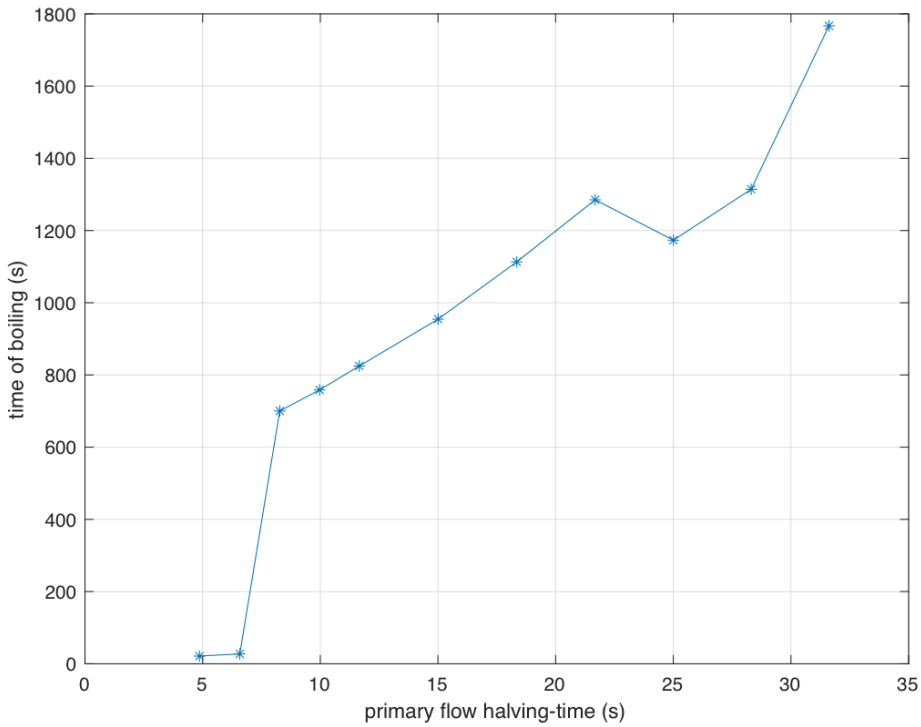

Figure 66: Time of boiling initiation in the ULOF transient of the B&B core with varying primary pump coast down halving times.

without ARC system. ARC designs which most improve the performance generally have small S, large w, and small ΔT_{act} – in other words the ARC designs which provide the fastest and strongest actuations. This results because a faster actuation causes core power to be decreased more rapidly. Because the ULOHS generally has peak coolant temperatures at the asymptotic state, bringing down the power more rapidly in the beginning of the transient allows for less power to be dumped into the coolant, and therefore asymptotic temperatures are reduced. It should be noted that an optimal point with increasing w exists, and in this case the largest gains were seen with $w = \$1.75$, beyond which gains again decrease. With this design, roughly 65°C of margin to coolant boiling is achieved.

Contrasting with the ULOHS results, the parametric study for the UTOP revealed no ARC designs which could avoid boiling. This is due to a series of oscillations induced by the ARC system response, as depicted in Figures 72 - 74 for the case with $w = \$2.0$, $S = 100$°C, $\Delta T_{act} = 10$°C. From examining the reactivity with time, the oscillations are caused by strong, rapid insertion of the ARC system in response to temperature increases, followed by rapid reductions in core temperatures and resulting un-actuation of most of the reactivity feedbacks. These rapid fluctuations in coolant temperatures are made possible by the high thermal conductivity of the metallic fuel in the B&B core, which leads to tight coupling between the fuel temperature and ARC system. However, because the ARC system is delayed in its response as compared to the coolant feedback, this coupled system leads to oscillatory behavior, which ultimately grows until boiling.

This oscillatory behavior was likely not seen in the oxide ABR due to oxide fuel's lower thermal conductivity, which impedes the communication of high fuel temperatures to the coolant, thereby reducing the coupling between fuel temperature and ARC system response. In order to reduce the coupling in the B&B core, a different method must be employed. It was seen in the ABR studies that increasing τ was able to remove oscillations from the ULOF response, and so this method was attempted for the

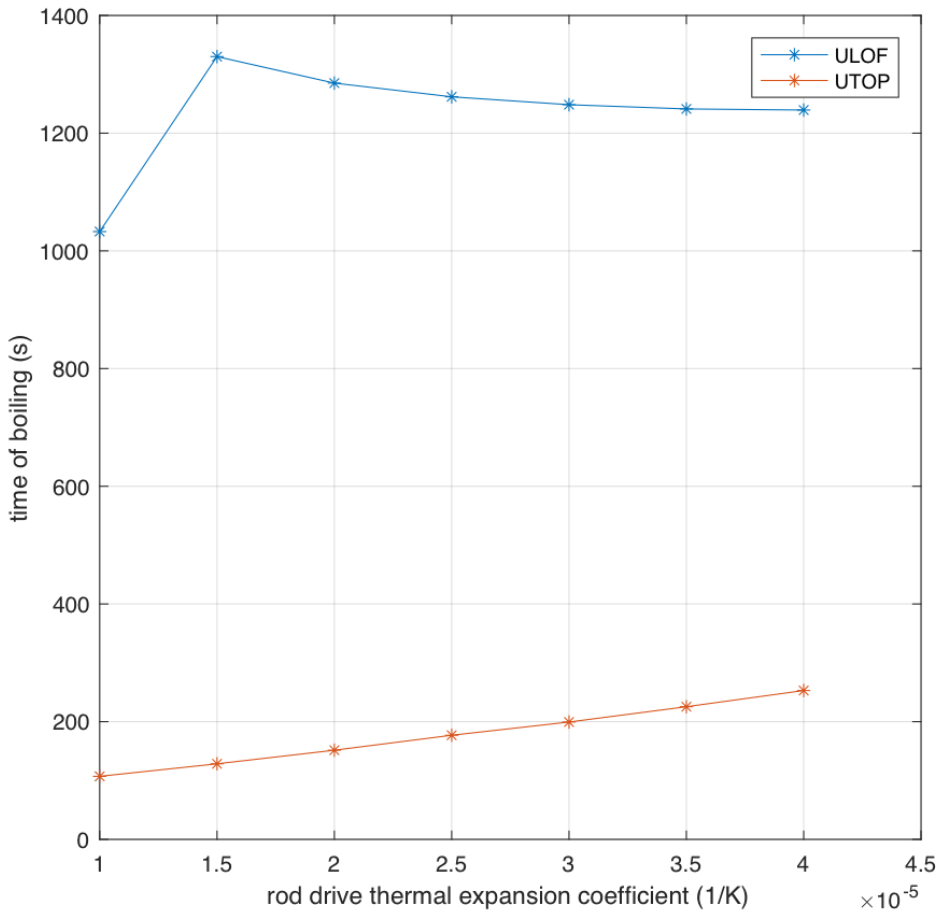

Figure 67: Time of boiling initiation in the B&B core with varying control rod drive thermal expansion coefficients for all three transients.

B&B core. Figure 75 shows the ARC system response in the UTOP scenario as τ is increased above its nominal value of 1.3 s. As τ is increased, the magnitude of the oscillations decreases until they are nearly removed with $\tau = 300$ s. At $\tau = 250$ s the transient progresses without boiling, indicating that this value of τ decouples the system enough for acceptable transient performance. Although no studies have been performed to determine how to make τ this large, it is assumed achievable by using a material with low thermal conductivity and/or altering the shape of the upper reservoir.

Using this larger τ, passive safety in the UTOP scenario is able to be realized, as depicted for the example case of $w = \$2.0$, $S = 100°\text{C}$, and $\Delta T_{act} = 10°\text{C}$ in Figures 76 - 78. Some oscillatory behavior still occurs in the first 500 s of the transient, however the oscillations are damped and eventually a new steady-state is reached with core temperatures less than 100°C above nominal. Attempting to completely remove the oscillations by further increasing τ is not effective, as it causes the ARC system actuation to be later and results in higher peak temperatures during the initial transient phase. Even with the oscillations, however, peak coolant temperatures are kept significantly far from boiling.

Figure 79 shows the parametric study for $\tau = 300$ s, the value at which the largest gains were achieved. The margin to boiling is maximized by ARC designs with high w and low S. Whereas in the ABR studies too high of S would lead to undesirable behavior, this is avoided in the B&B by making τ very large. Boiling is not able to be avoided if w is not greater than approximately \$1.0, implying that an aggressive ARC design is necessary to obtain passive safety in the UTOP.

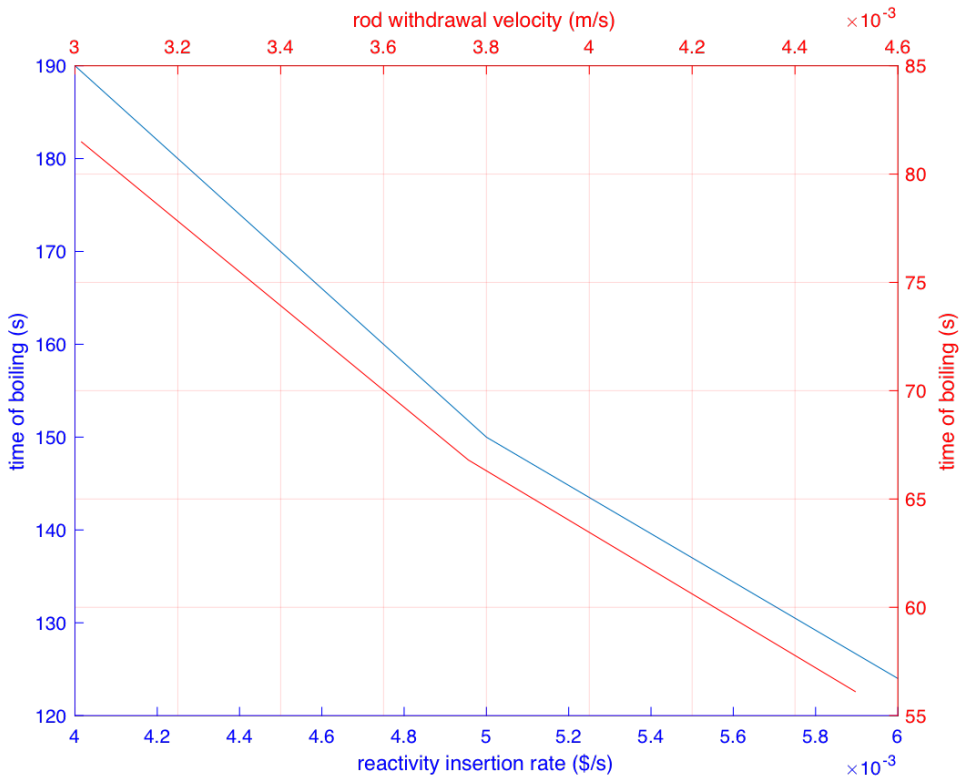

Figure 68: Time of boiling initiation in the UTOP of the B&B core with varying reactivity insertion rates.

Since τ needs to be increased to achieve acceptable UTOP behavior, a study was performed to determine the impact of higher τ on the ULOHS performance. Figure 80 shows that as τ is increased up to 300 s, the impact on peak temperatures in the ULOHS is negligible, and therefore the larger value should be acceptable from the perspective of ULOHS passive safety.

Similar to the UTOP, no ARC system designs with $\tau = 1.3$ s were able to prevent boiling in the ULOF. The cause of boiling was again oscillatory behavior at the transition from forced- to natural-circulation, which is not able to be mitigated by the ARC system. With the ARC system included, this oscillatory behavior is in fact worsened, as shown in Figure 81 for the case with $\tau = 1.3$ s, $w = \$2.0$, $\Delta T_{act} = 10°\text{C}$, and $S = 50°\text{C}$. No relaxation of either τ or S was able to eliminate the oscillations enough to avoid boiling.

Although increasing the pump coast down time showed ULOF gains over the nominal case, this method does not help to avoid boiling because it only delays the time of the flow transition, which ultimately leads to boiling. While the oscillations at the flow transition were avoided in the nominal case by sufficiently reducing the pump rotor loss coefficient, this method is not effective when the ARC system is added. The complicated interplay between feedbacks, primarily coolant and ARC, leads to oscillations and boiling even with the very small loss coefficients explored in Section 8.4.4. In light of this, the optimal ARC system design is identified as the one which most improves the ULOHS and UTOP performance: $w = \$1.75$, $S = 50°\text{C}$, $\Delta T_{act} = 10°\text{C}$, and $\tau = 300$ s.

8.6 Summary of Results

Transient performance without ARC system inclusion was poor, with both the UTOP and ULOF leading to boiling. To understand the sensitivity of these results to model assumptions, parametric studies were performed and it was found that boiling could be avoided in the ULOF if the locked rotor loss coefficient of the primary pump were significantly reduced, although oscillatory behavior is still seen. No parametric variation allowed for passive safety in the UTOP before ARC system inclusion. By including ARC systems,

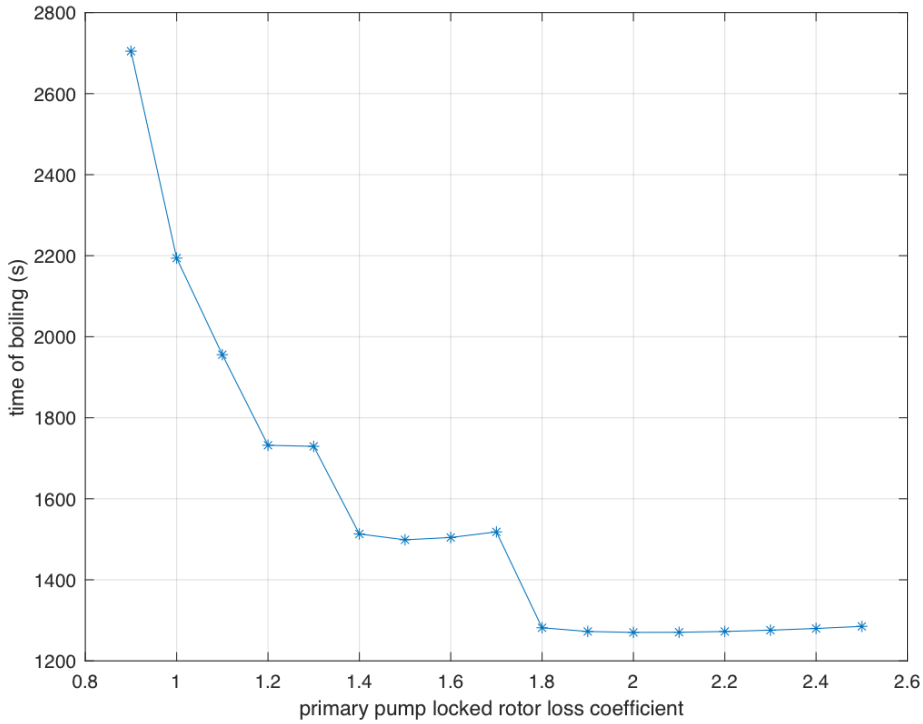

Figure 69: Time of boiling initiation in the ULOF of the B&B core with varying locked rotor loss coefficients.

significant gains were achieved. With aggressive ARC system designs, the margin to coolant boiling was increased by roughly 65°C. Additionally, by increasing τ to 300 s, oscillations could be damped and boiling was avoided in the UTOP as well, with more than 150°C margin to boiling. This increase in τ was shown to have negligible impact on the ULOHS performance. However, no ARC system design could be found to mitigate the oscillations in the ULOF at the transition from forced- to natural-circulation, and therefore complete passive safety was not enabled.

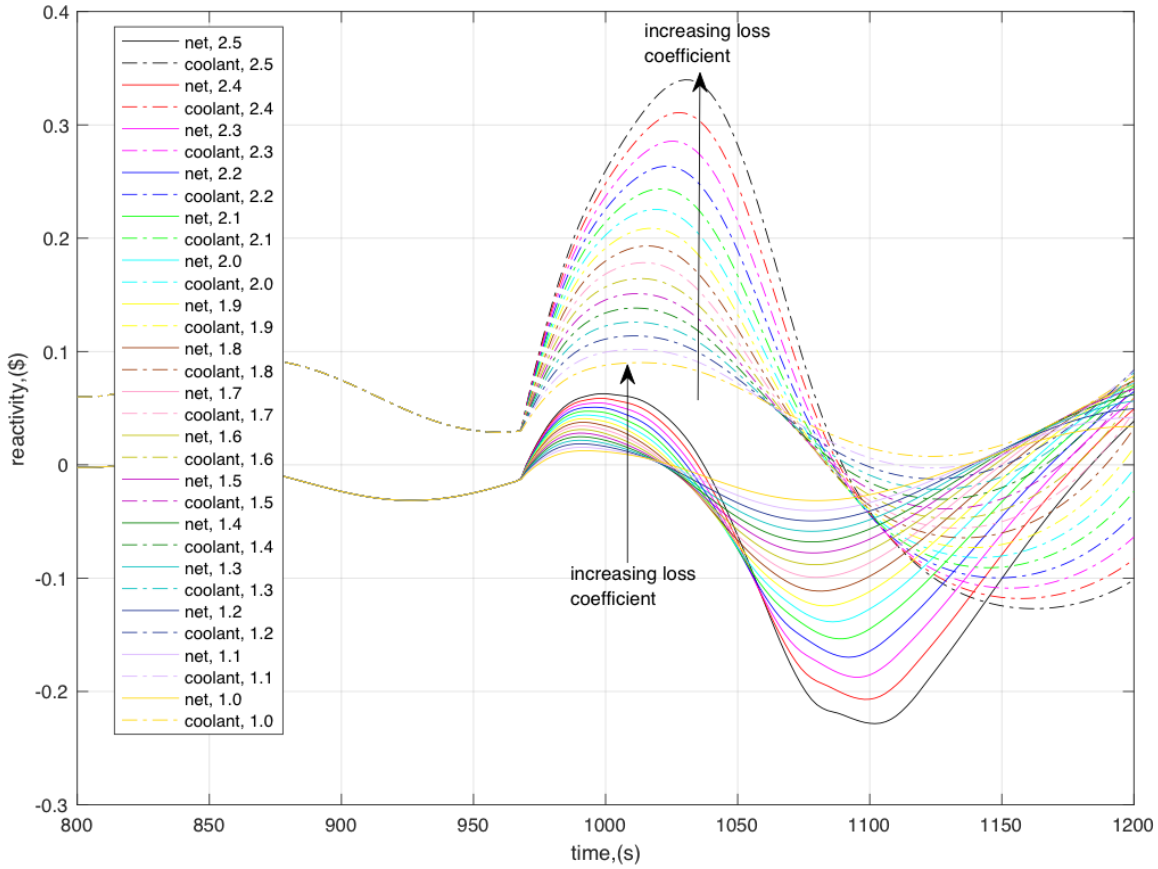

Figure 70: Net and coolant reactivity components in the UTOP of the B&B core with varying locked rotor loss coefficients.

9 Neutronic Impact of ARC System Inclusion

It has been shown that ARC system inclusion has the potential to enhance SFR performance. However it is expected that inclusion will also induce a neutronic penalty stemming from the removal of fuel and the addition of non-fuel in-core materials. The purpose of this section is to investigate this penalty, while also examining the amount of tritium produced in ARC system components and the amount of absorber depleted over the ARC system's residence time. To make this study general, a wide range of ARC system designs are investigated, allowing for sensitivities to ARC design parameters to be identified.

9.1 Methodology

9.1.1 Computational models

This section focuses exclusively on the B&B core. The B&B core was chosen due to the tight neutron economy required to achieve breed-and-burn operation. It is assumed that each fuel assembly is equipped with an ARC system of equivalent design. Therefore, it is not expected that a significant change in the radial flux profile will be induced, and impacts on the radial power profile are not examined. Instead, this study is interested in the quantification of k_{eff}. Previous studies have demonstrated the adequacy of r-z models at predicting k_{eff} for B&B cores [30], and therefore this study employs r-z models for all criticality calculations.

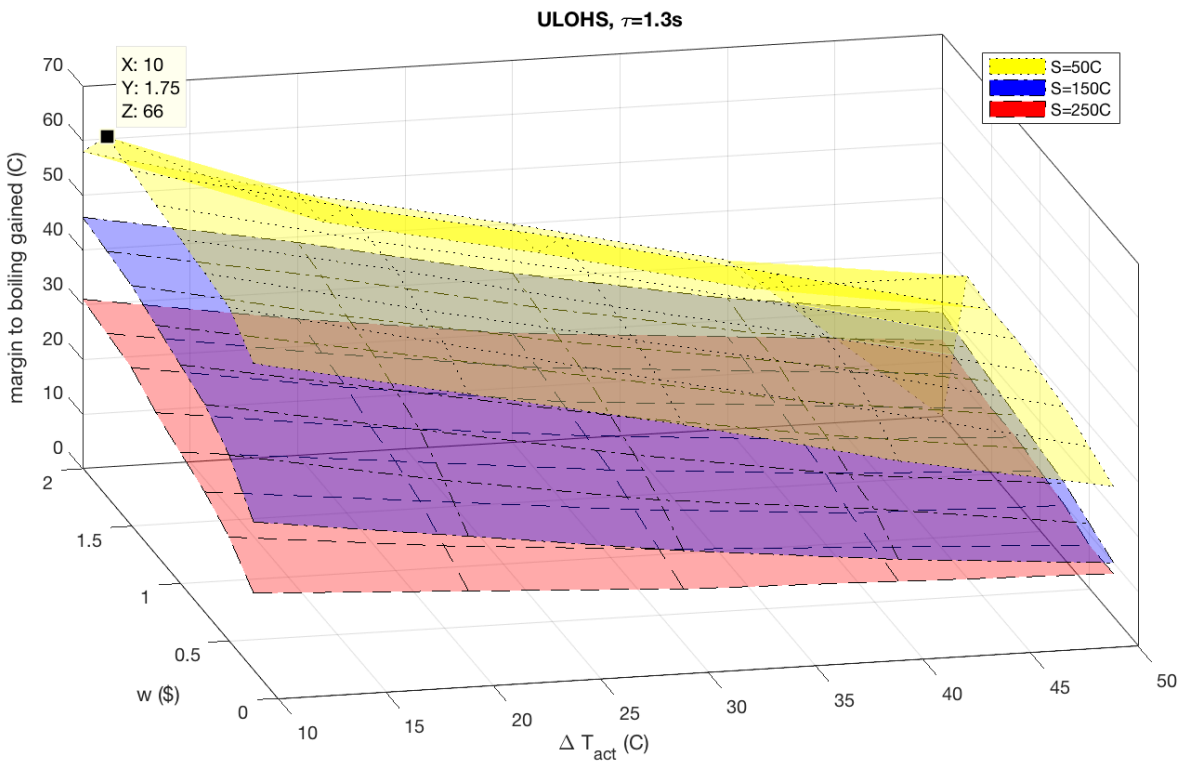

Figure 71: Margin to coolant boiling gained in the ULOHS scenario of the B&B core with ARC system inclusion as a function of ARC system design parameters.

The core is divided into 12 radial batches representing 41 assemblies each, with batch constituents smeared into volume-fraction-conserving cylindrical annuli located at the approximate average batch location. Each batch is split into 9 equal-volume axial segments. All models are built with the Serpent 2 monte carlo code. Equilibrium cycle burnup calculations are performed in three equal-length steps with the control system fully withdrawn. All calculations except those to quantify tritium production are performed with the ENDF/B-VII.1 cross-section library. Calculations to quantify tritium production are performed using the JEFF-3.1 library due to the lack of fission product yields for tritium in the ENDF library.

To quantify the various impacts, modifications are made to an equilibrium cycle model of the nominal core without ARC system inclusion. After making modifications to represent different aspects of ARC system inclusion, the model is run again using the equilibrium cycle characteristics of the nominal core. New equilibrium cycle calculations are not performed. It is natural to measure the neutronic penalty in terms of the increase in equilibrium cycle length, but because there is a direct relation between core excess reactivity and cycle length, quantifying the k_{eff} penalty is equivalent to finding the resulting cycle length increase. In light of this relationship and the longer run times of equilibrium calculations, the neutronic penalty is quantified in terms of k_{eff} evolution rather than equilibrium cycle characteristics.

9.1.2 Determination of soluble lithium distribution

Although the three ARC system fluids are largely immiscible, each fluid is soluble within the others to a small degree. This is especially important in the direction of lithium being dissolved in potassium or helium, as this allows for lithium to be present in the active core, which may lead to a neutronic penalty or the production of tritium. To quantify these impacts, first the steady-state distribution of soluble

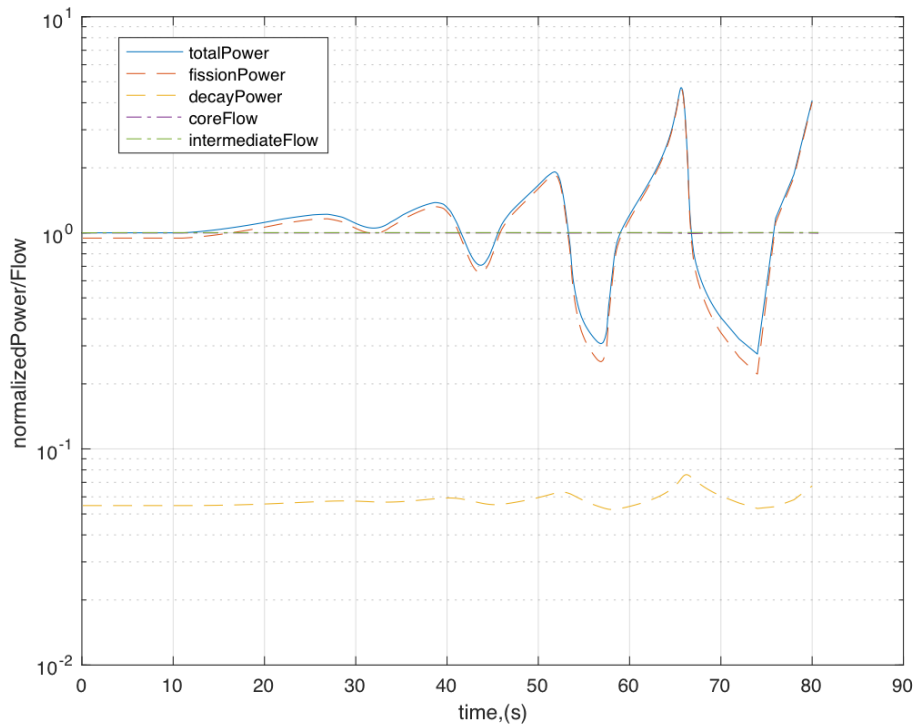

Figure 72: Power and flow with time for the UTOP scenario in the B&B core with ARC system inclusion.

absorber fluid within the core must be determined.

Within the ARC system, the absorber fluid (lithium) is in contact with both the expander fluid (potassium) and the inert gas (helium). The geometry near these interfaces is represented in Figure 82a. The lithium can take two paths to enter the active core region via diffusion: (1) upwards into the helium gas or (2) first downwards into the lower reservoir of potassium and then upwards through the inner concentric tube. Due to geometric uncertainties associated with path (2), a conservative assumption is employed: the distance of initial downward diffusion of lithium into potassium is negligible and the lithium is assumed to be located immediately below the inner concentric tube, only having to diffuse upwards to reach the active core. In reality, the downward diffusion step will act as a buffer delaying the poison from entering the active core. This assumption allows for both pathways to be treated as independent 1-dimensional diffusion problems of lithium into the active core, as depicted in Figures 82b and 82c.

During operation, the in-core lithium profile will reach a steady-state according to a balance of lithium sources and sinks. Including 1-dimensional diffusional fluxes and a volumetric neutron flux sink, this balance is represented by Equation 29, where N is the molar concentration of the mixture, N_{Li} is the molar concentration of lithium, $x_{Li} = N_{Li}/N$, D_i is the diffusion coefficient of lithium through either liquid potassium or gaseous helium, ϕ is the neutron flux, and σ is the microscopic cross-section for lithium depletion. Due to the small diameter of the ARC system tubes (a few millimeters), convective mass transport is assumed negligible.

$$\frac{dN_{Li}(z)}{dt} = -\frac{d}{dz}N(z)D(z)\frac{dx_{Li}(z)}{dz} - \phi(z)\sigma(z)N_{Li}(z) \tag{29}$$

For the case that the dissolved lithium fraction is very small, we can approximate $N \approx N_i$, where N_i is the molar concentration of either potassium or helium. Due to the low solubility of lithium in the other ARC fluids, the diffusion coefficient can be made independent of position if evaluated at an average system temperature. Neglecting time dependence, we then have a steady-state reaction-diffusion equation.

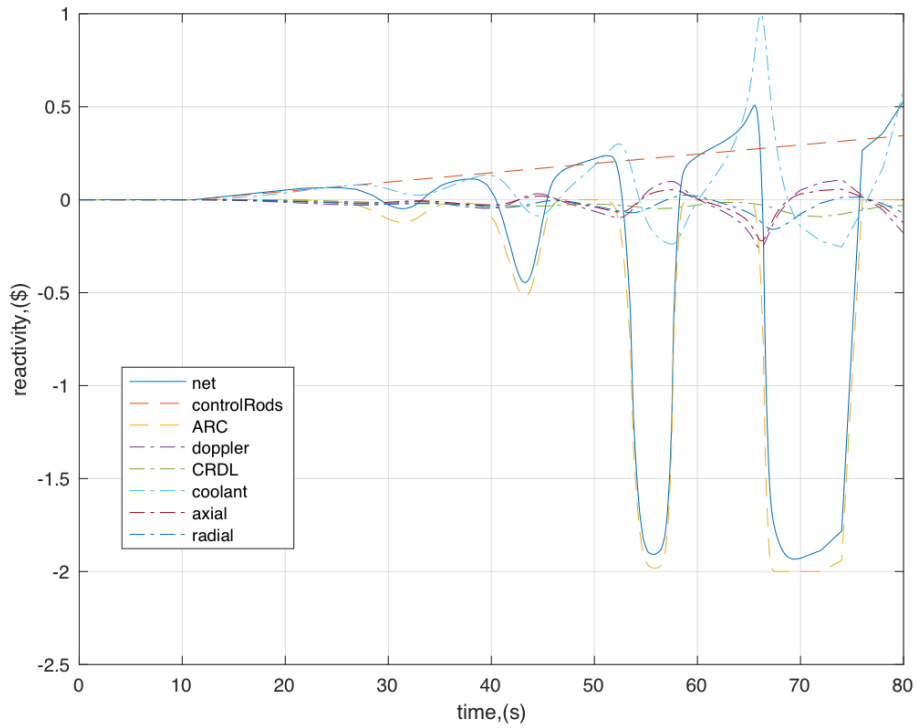

Figure 73: Reactivity feedbacks with time for the UTOP scenario in the B&B core with ARC system inclusion.

$$0 = -D\frac{d^2 N_{Li}(z)}{dz^2} - \phi(z)\sigma(z)N_{Li}(z) \tag{30}$$

To determine the relative magnitudes of the competing diffusion and depletion mechanisms, Equation 30 can be nondimensionalized by introducing dimensionless variables $\bar{N}_{Li} = N_{Li}AL$ and $\bar{z} = z/L$, where L and A are a characteristic length and area, respectively. Substituting these variables into Equation 30, the nondimensional equation is shown below:

$$0 = -\frac{d^2 \bar{N}_{Li}}{d\bar{z}^2} - \frac{\phi\sigma L^2}{D}\bar{N}_{Li} \tag{31}$$

In this equation, a dimensionless term similar to the Thiele Modulus is formed as $\frac{\phi\sigma L^2}{D}$. This term represents the ratio of lithium depletion via neutron transmutation to lithium replenishment via diffusion. Evaluating this dimensionless ratio with representative values gives an estimate of the relative strengths of the two competing processes.

The flux can be determined for the B&B core with Serpent 2. Doing so, one finds that the flux may vary from about 10^{13} 1/cm^2/s in the core periphery regions up to about 10^{15} 1/cm^2/s in the high fission-density region of the core.

The lithium depletion cross-section can be determined similarly. Natural lithium is composed of two isotopes. All transmutation pathways, with the exceptions of ^{6}Li(n,t)^{4}He, ^{7}Li(n,γ)^{8}Li, and ^{6}Li(n,γ)^{7}Li, are threshold reactions above roughly 5 MeV. As seen in Figure 83, the neutron flux at these high energies is comparatively little, implying threshold reactions can be ignored. Additionally, the ^{7}Li(n,γ)^{8}Li and ^{6}Li(n,γ)^{7}Li cross-sections are neglected because they are roughly 4 orders of magnitude smaller than that for ^{6}Li(n,t)^{4}He. Finally, assuming 100% enrichment in ^{6}Li leads to a conservative assessment, as

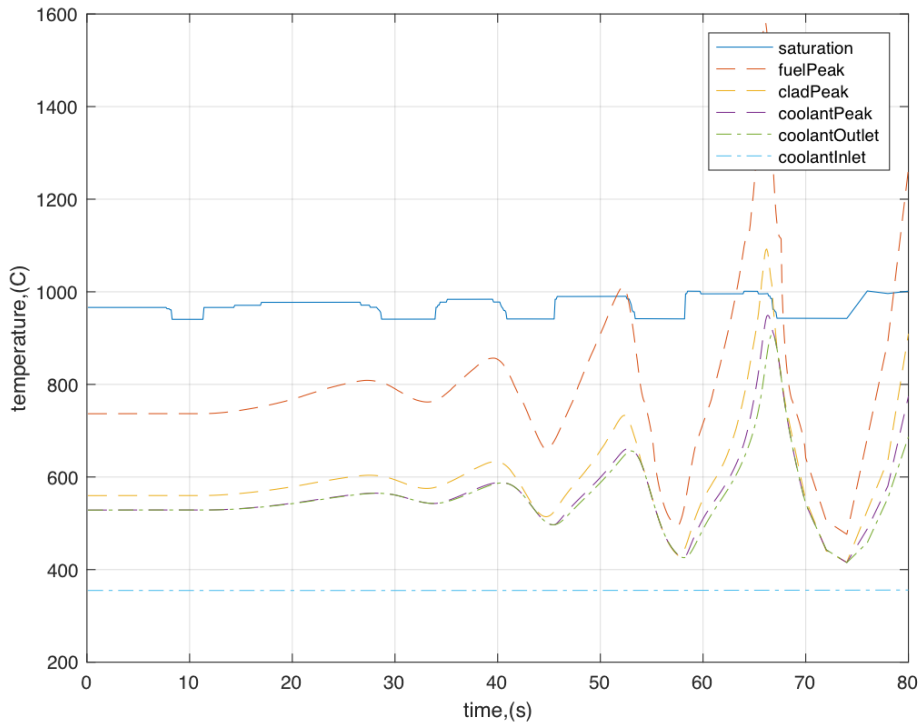

Figure 74: Core temperatures with time for the UTOP scenario in the B&B core with ARC system inclusion.

this isotope has both higher transmutation cross-section and will produce more tritium. Evaluating this cross-section over the spectrum of the B&B core, the transmutation cross-section is found to be roughly 1 b.

The characteristic length scale L is taken as the system diffusion length, $L = 2\sqrt{Dt}$, where t is the assembly in-core residence time. Making this substitution, it is found that the dimensionless ratio is independent of the diffusion coefficient, making the relative strength between flux depletion and mass diffusion dependent only on time, neutron flux level, and the transmutation cross-section.

Using the values determined above, a range for the dimensionless ratio is shown in Figure 84 for two different neutron flux levels representing positions of high flux (10^{15} 1/cm^2/s) and positions of low flux (10^{13} 1/cm^2/s). In regions of low flux, the steady-state profile is mainly governed by mass diffusion. For regions of high flux, the balance is dominated by mass diffusion in earlier times, but dominated by flux depletion at later times. However, for a B&B core, much of an assembly's lifetime is spent in regions of lower flux level as fissile material is being bred. Therefore, for much of an assembly's lifetime, the lithium concentration profile will be dominated by mass diffusion.

This analysis implies that the steady-state lithium profile is not dominated by flux depletion, meaning that there will be some amount of lithium present within the expander and inert gas ARC fluids. Although Equation 30 can be iteratively solved according to the specific flux profile of this particular B&B core, the nondimensional analysis implies that the neutron flux depletion can be neglected in many cases. Any lithium concentration profile derived under this assumption is conservative in the sense that it will over-predict the amount of lithium in the core, giving upper bounds on both the neutronic penalty and the amount of in-core tritium produced. Making this assumption, Equation 30 becomes:

$$0 = \frac{d^2 N_{Li}(z)}{dz^2} \tag{32}$$

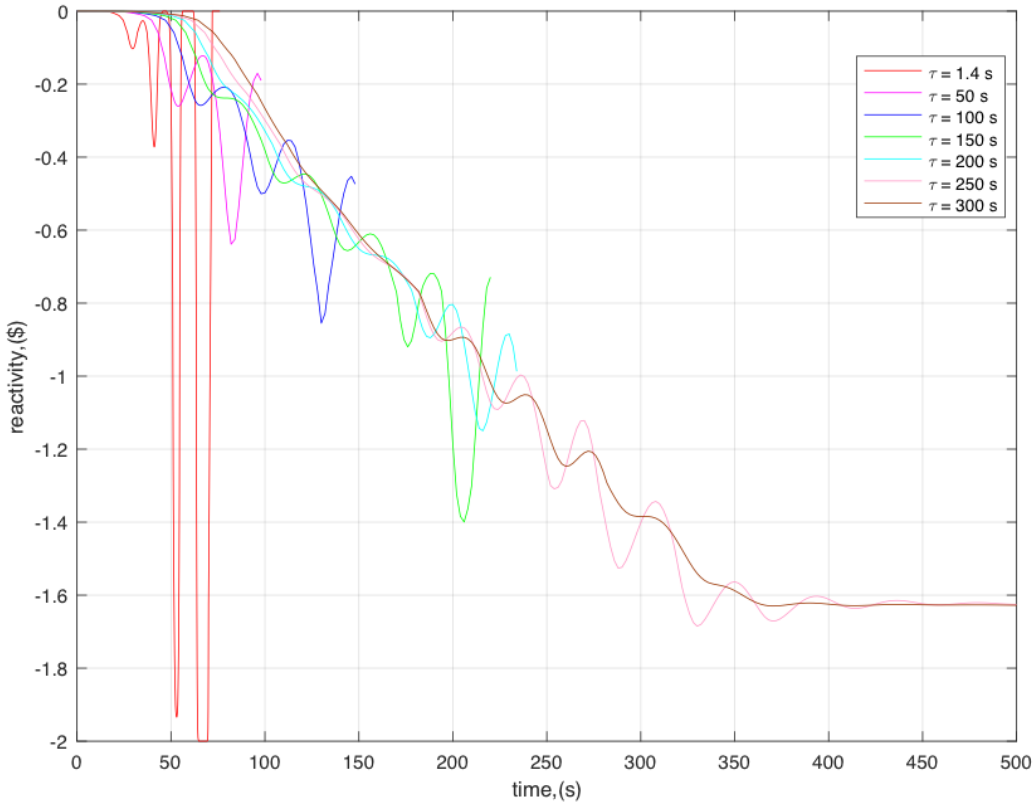

Figure 75: ARC system reactivity insertion in the UTOP as τ is increased.

Integrating twice gives a linear relation, and the constants of integration are found through the boundary conditions. The concentration of lithium immediately at the fluid interface can be determined using thermodynamic data if the two fluids are in thermal equilibrium, providing a boundary condition at the lower end. For both scenarios, each chamber of the upper reservoir (filled with either potassium or helium) is assumed to be an infinite sink for soluble lithium, providing a boundary condition at the upper end. This infinite sink assumption is validated subsequently in Section 9.5. Finally, the lithium profile is determined as shown in Equation 33, where S_i is the equilibrium solubility of lithium in fluid i and L_{ARC} is the axial length of the ARC system tubes.

$$N_{Li}(z) = -\frac{S_i N_i}{L_{ARC}} z + S_i N_i \tag{33}$$

The solubility of liquid lithium in liquid potassium at equilibrium can be obtained from the equilibrium phase diagram or a correlation, whereas the solubility of liquid lithium in gaseous helium can be obtained from the vapor pressure of lithium. Although the outlet temperature for the B&B system under consideration is outside of the range of validity by 10°C, Equation 34 is used to determine the solubility of lithium in potassium due to lack of data at higher temperatures.

$$S_{Li \to K}\ [atom\%] \ = 691.86 \times \exp - \frac{4229.9}{T + 273} \quad : \ 63 \leq T \leq 500°C \tag{34}$$

The equilibrium solubility of lithium in potassium is 0.82 atom% at the inlet temperature, while the partial pressure (and thus solubility) of lithium into gaseous helium is near zero. Because the lithium profile is a maximum at the fluid interface, the low solubility indicates that lithium dissolution in helium

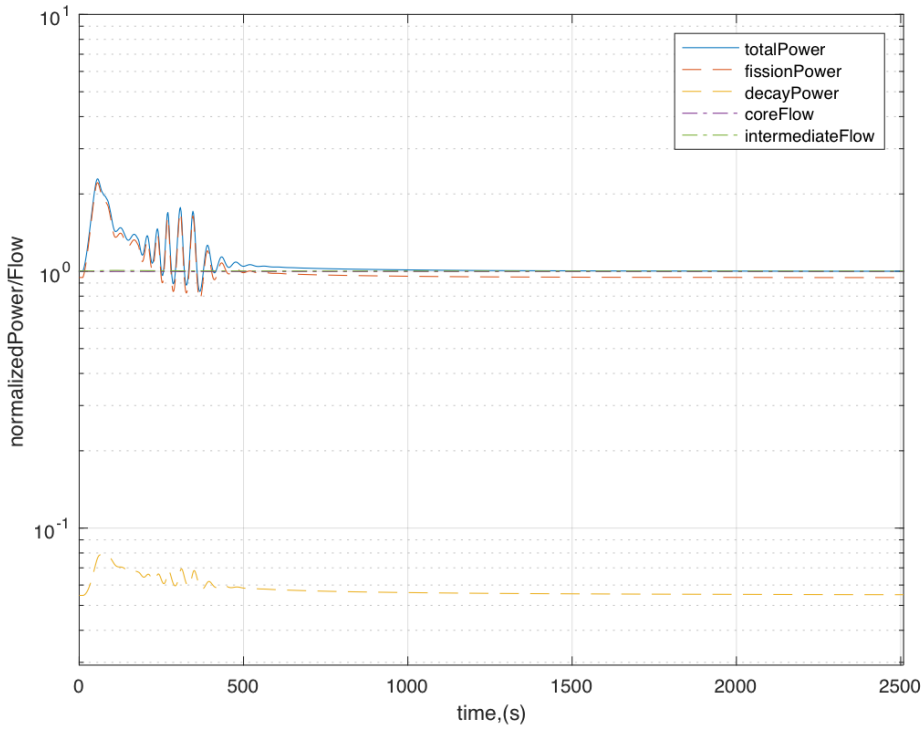

Figure 76: Power and flow with time for the UTOP scenario in the B&B core with ARC system inclusion and $\tau = 250$ s.

will be negligible, allowing for the in-core inventory of lithium to be evaluated as exclusively that which is dissolved in potassium.

9.2 Neutronic impact

To identify the root causes of any neutronic penalty, the study is done in steps as follows:

1. Fuel is removed from a number of pins per assembly and replaced with void to evaluate the impact of lower fuel volume fraction
2. A range of combinations of expander fluid, inert gas, and steel are added to the inside of the voided fuel pins to evaluate the impact of increased parasitic absorption by ARC in-core materials
3. Absorber fluid is added to the expander fluid to evaluate the impact of soluble absorber diffusion into the active core

The results of these steps are outlined in the following subsections.

9.2.1 Removal of fuel

In the standard ARC system design, multiple fuel pins may be replaced with multiple sets of concentric tubes in order to achieve a strong enough negative reactivity insertion. This impact is quantified by reducing the fuel volume fraction in each assembly to represent the loss of one, two, and three pins worth of fuel with the remaining volume fractions left unchanged. The reduced fuel volume fraction is made up by introducing a corresponding void volume fraction. The impact on k_{eff} of these modifications is shown in Figure 85.

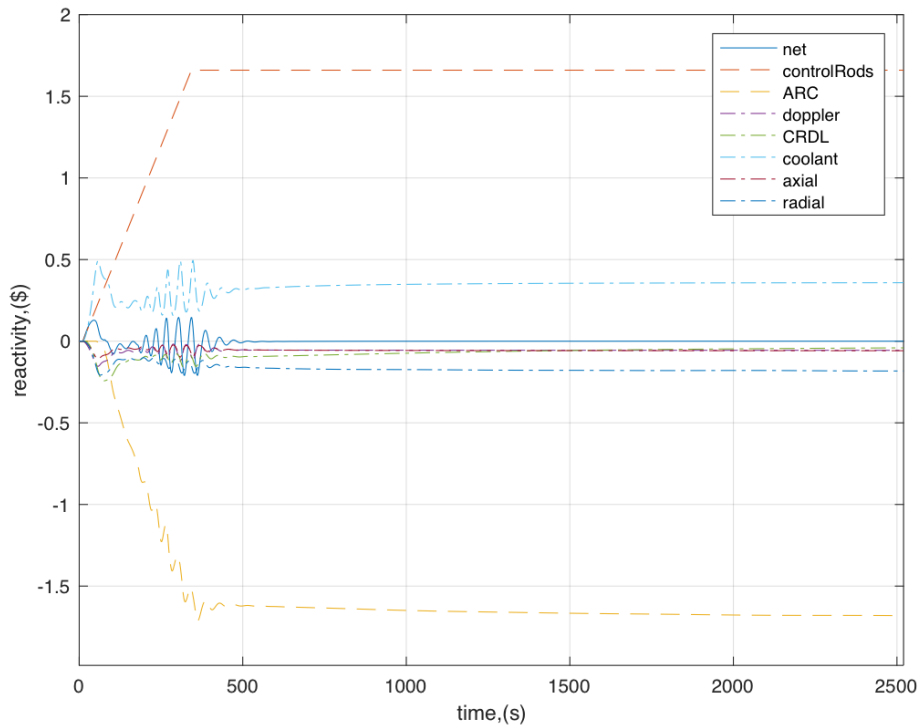

Figure 77: Reactivity feedbacks with time for the UTOP scenario in the B&B core with ARC system inclusion and $\tau = 250$ s.

The decrease in core reactivity is approximately linear with the number of fuel pins removed, and the maximum penalty is roughly 700 pcm for the case with three pins removed. For most core designs it is expected that only a single pin per fuel assembly will need to be replaced by ARC tubes; therefore, this quantification is expected to cover the majority of cases that a designer may wish to explore.

9.2.2 Addition of ARC tubes

This section introduces the in-core ARC materials (i.e. expander fluid, inert gas, and steel) into the model to determine their neutronic impact. In reality, some amount of absorber fluid will be soluble in the other fluids and will therefore also be present in the active core – this impact is quantified in Section 9.2.3.

In practice, a designer may wish to tailor the actuation characteristics by tuning the volume fractions of each ARC system constituent. To keep this study general, a variety of ARC system designs are investigated in terms of these variable volume fractions. To be conservative, it is assumed that three fuel pins have been replaced with ARC tubes. Then, a series of criticality calculations are performed while varying the volume fractions within the ARC tubes of steel, expander fluid, and inert gas. The minimum volume fraction for any of the three constituents is assumed to be 0.1. The ideal gas law at a pressure of 1 atm is used to determine the number density of helium atoms. Density correlations for HT9 and potassium are repeated here, along with that for lithium (the absorber fluid):

$$\rho_{HT9}\ [\frac{kg}{m^3}] \ = 7824 - 9.288 \times 10^{-5}T - 0.1859T^2 \quad : \ 298 \leq T \leq 923\ K \tag{35}$$

$$\rho_K\ [\frac{g}{cm^3}] \ = 0.8415 - 2.172 \times 10^{-4}T - 2.70 \times 10^{-8}T^2 + 4.77 \times 10^{-12}T^3 \quad : \ T \leq 1250°C \tag{36}$$

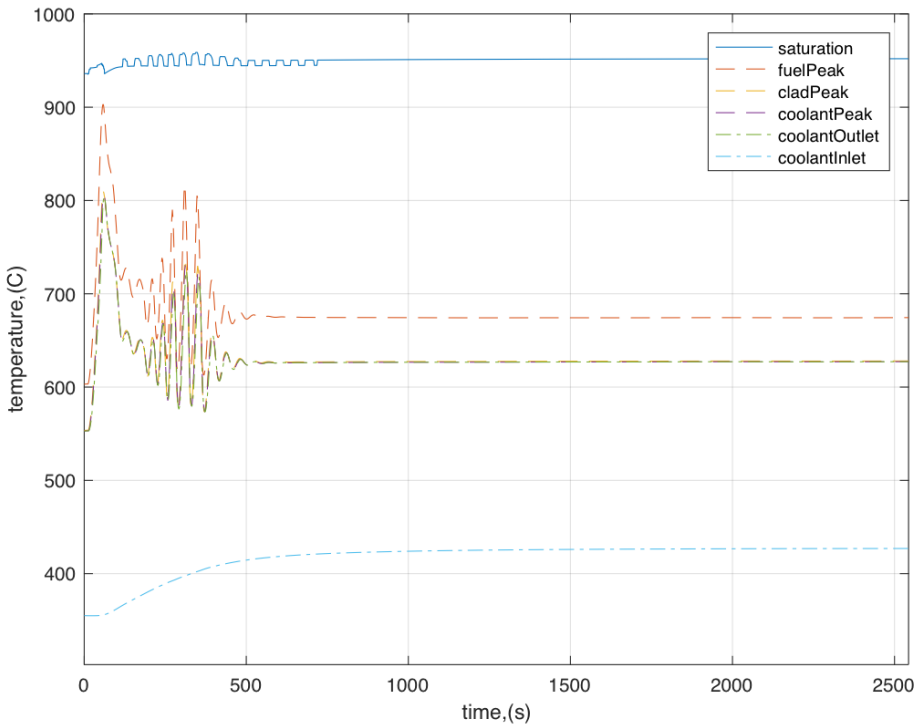

Figure 78: Core temperatures with time for the UTOP scenario in the B&B core with ARC system inclusion and $\tau = 250$ s.

$$\rho_{Li}\ [\frac{kg}{m^3}]\ = 562 - 0.1T \quad : \ 400 \leq T \leq 1300\ K \tag{37}$$

Compared to the removal of fuel, the addition of the ARC system materials results in a smaller k_{eff} penalty. The worst neutronic performance results from designs with higher steel and expander volume fractions due to their higher densities and cross-sections compared to the inert gas, leading to a neutronic penalty of at most 100 pcm. This study shows that, even with three fuel pins replaced by ARC tubes, a large design space exists to tune ARC systems without incurring significant neutronic penalties.

9.2.3 Soluble absorber

To assess the neutronic impact of the soluble lithium, a bounding criticality calculation is performed with the ARC design that introduces the most in-core lithium: three fuel pins replaced by ARC tubes of 80, 10, and 10 vol% expander, steel, and gas, respectively. The lithium is 100% enriched in ^{6}Li and dissolved in the expander fluid according to Equation 33. The Serpent model allows for depletion of fuel materials but keeps the concentration of lithium constant to reflect the assumption that lithium replenishment is faster than depletion. The criticality calculations show a neutronic penalty from the soluble lithium so small that it cannot be distinguished within the 20 pcm uncertainty of the calculations. This analysis shows that the neutronic penalty from in-core dissolved lithium is negligible.

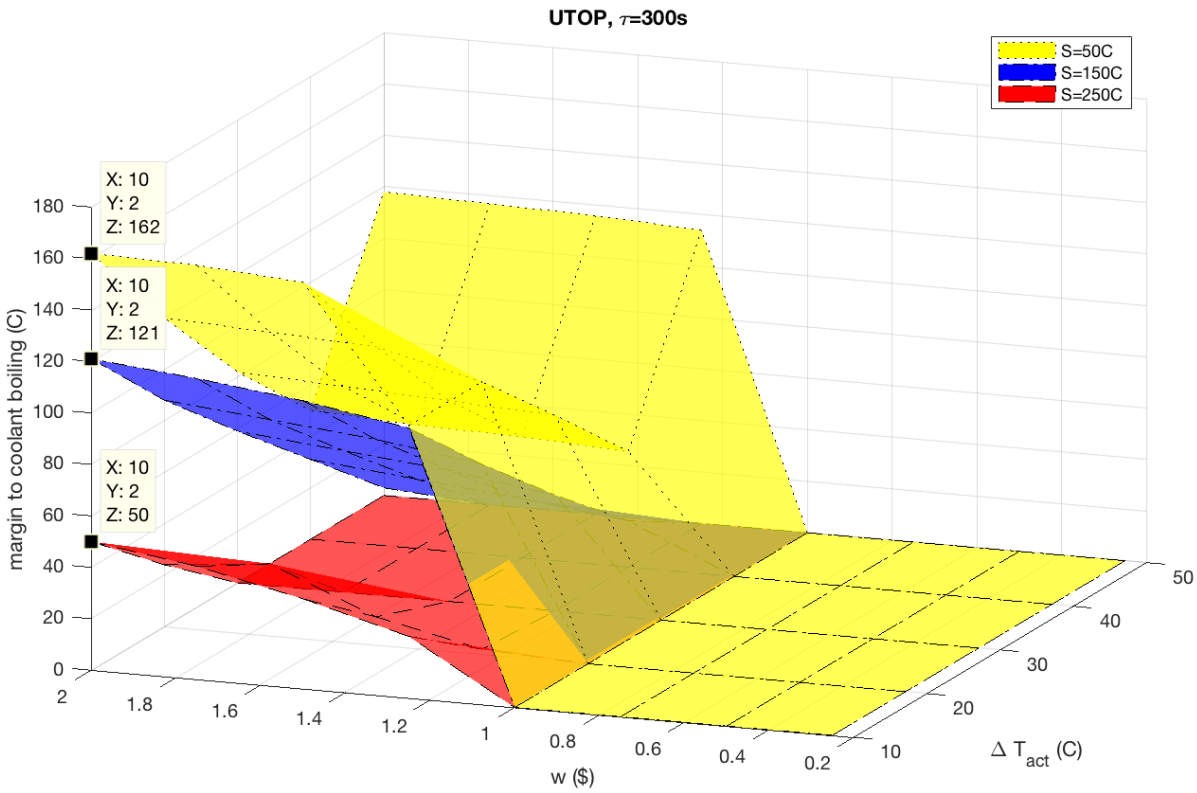

Figure 79: Margin to coolant boiling gained in the UTOP scenario of the B&B core with ARC system inclusion as a function of ARC system design parameters.

9.3 Tritium production

9.3.1 In-core tritium production

Although the neutronic penalty from the in-core lithium has been shown to be small, in-core lithium may still be undesirable from the perspective of tritium production. Tritium is of particular concern due to its high mobility and its role as a biological hazard. In-core tritium can be produced through a number of pathways, including (1) as a fission product, (2) in control material through the ^{10}B(n,2α)t reaction, (3) in helium through the ^{3}He(n,p)t reaction, and (4) in lithium through both the ^{6}Li(n,α)t and ^{7}Li(n,nα)t reactions. Pathways (1) and (2) will be present independent of ARC system inclusion, whereas pathways (3) and (4) will be enhanced by ARC system inclusion because neither He nor Li are normally present in significant quantities. Due to the low density of gases and the low relative abundance of ^{3}He (0.0002%), the main pathway for increased tritium production is likely the introduction of ARC system lithium. Since it is assumed that the lithium fluid will be significantly enriched in ^{6}Li and the ^{7}Li(n,nα)t reaction is a threshold reaction above 2.5 MeV [31], the ^{6}Li(n,α)t reaction will be the main contributor.

To quantify the increased tritium production, tritium inventories between Beginning of Cycle (BOC) and End of Cycle (EOC) as calculated by Serpent are compared. This is done both with and without ARC system inclusion to isolate the tritium produced specifically by the ARC system. In both cases, the control system is fully withdrawn, so tritium produced in the control elements is not considered. Calculations including lithium employ the profile specified by Equation 33.

Tritium production in the reference core is found to be 2.075E+04 Ci/yr. The addition of the ARC system brings the tritium production level up to 2.117E+04 Ci/yr, or a 2% increase, although it is emphasized that this is an over-estimation as it assumes a steady-state lithium profile independent of

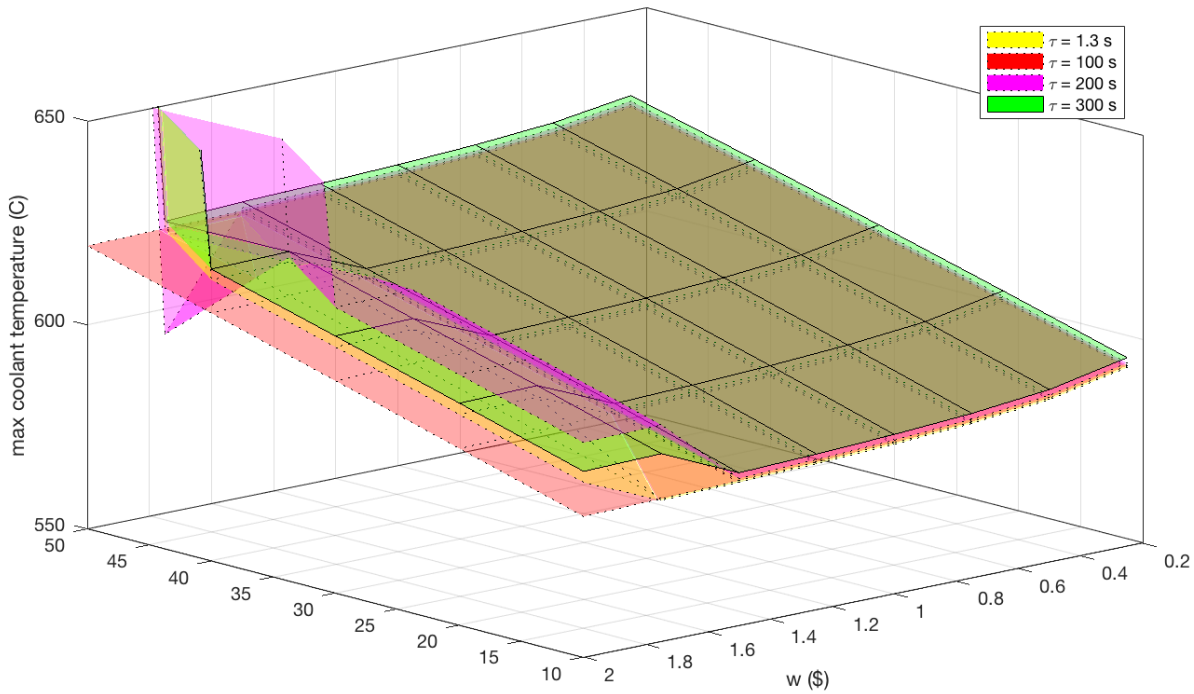

Figure 80: Peak coolant temperatures in the ULOHS scenario of the B&B core as a function of ARC design parameters with increasing τ.

neutron flux. Therefore it is concluded that the production of in-core tritium from the ARC system is minor.

9.3.2 Ex-core tritium production

In addition to that which has diffused into the active core, a large source of lithium lies below the core in the lower reservoir. The net tritium production in the lower reservoir with time is determined through Equation 38, where ϕ is the neutron flux in the lower reservoir region, σ_{Li} is the tritium production cross-section from lithium, σ_T is the cross-section for tritium burnout, λ_T is the decay constant of tritium, N_T is the number density of tritium, and N_{Li} is the number density of lithium at 355°C according to Equation 37.

$$\frac{dN_T}{dt} = \phi\sigma_{Li}N_{Li}(t) - \lambda_T N_T(t) - \phi\sigma_T N_T(t) \tag{38}$$

Tritium burnout occurs through (n,2n) and (n,3n) reactions, both of which are threshold reactions above 8 MeV. Therefore they are conservatively neglected in this analysis. Because there is a large amount of lithium in the system and no lithium production, the number density of lithium is conservatively taken as a constant. Making these assumptions, Equation 38 can be solved for N_T as:

$$N_T(t) = \frac{\phi\sigma_{Li}N_{Li}}{\lambda_T}\left[1 - e^{-\lambda_T t}\right] \tag{39}$$

Due to uncertainties in the physical geometry of the lower reservoir, both ϕ and σ_{Li} are tallied by Serpent 2 immediately below the lower shield without including the lower reservoir in the model. Therefore

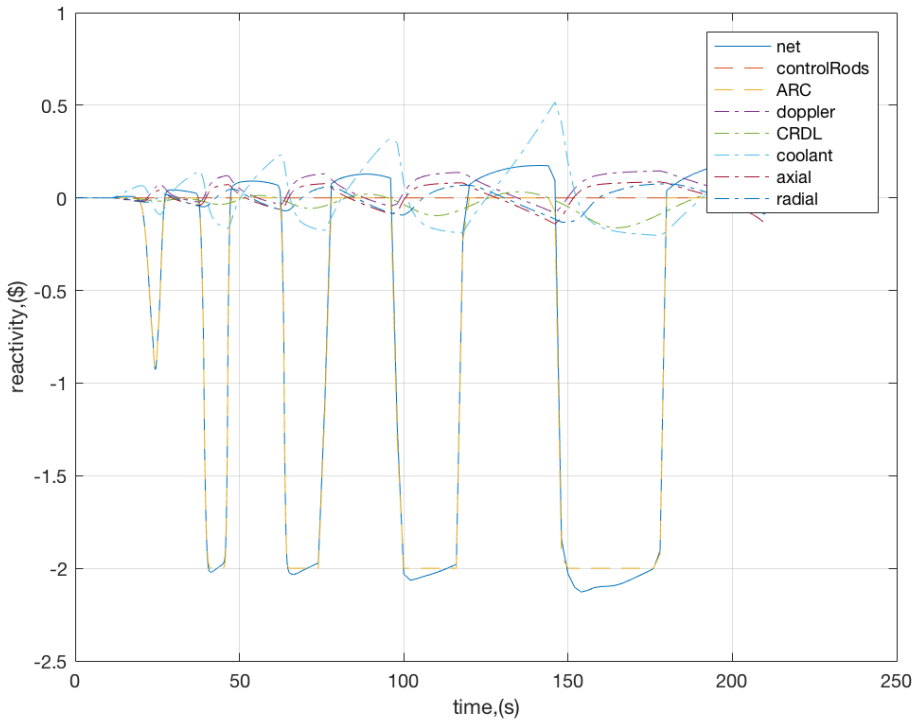

Figure 81: Reactivity feedbacks with time for the ULOF scenario in the B&B core with ARC system inclusion.

these values do not account for self-shielding effects in the lithium layer and are conservative in the sense that the neutron flux will be over-predicted.

Equation 39 can be used to determine the concentration of tritium in each assembly at BOC and EOC. Taking the difference of these values, integrating over all assemblies, and converting to units of Ci/yr, Figure 86 shows the tritium production in the lower reservoir as a function of lower shield thickness. In each case, the lower reservoir ^{6}Li volume is assumed to be equal to two times the volume of the ARC system tubes to account for the fact that during actuation some amount of absorber fluid will accumulate in the upper reservoir, requiring the lithium volume to be larger than the volume of the tubes.

Figure 86 indicates that tritium production attenuates approximately exponentially with shield thickness. In order for tritium production in the lower reservoir to be below that of the active core, the thickness of the lower shield needs to be increased from its nominal value of 5 cm up to roughly 11 cm, although this would still lead to a doubling of the overall tritium production as compared to the case without ARC system inclusion.

Also shown in Figure 86 is tritium production within the lower shield, determined in the same manner as was used for the lower reservoir but replacing variables in Equation 39 where appropriate. Because B_4C shield material can lead to tritium through ^{11}B(n,t)^{9}Be and ^{10}B(n,2α)t reactions, it is important to ensure that the increased shield thickness does not negate the reduced tritium production in the lower reservoir. Figure 86 indicates that tritium production in the lower shield is always orders of magnitude below the in-core production, and is therefore a small price to pay for reducing tritium in the lower reservoir.

This section demonstrates that tritium production in ex-core ARC system components may be larger than that of in-core ARC components. This ex-core production can be effectively managed by placing shielding between the active core and the ARC lower reservoir to meet the needs of the designer, however a tradeoff exists between tritium production and increased core length.

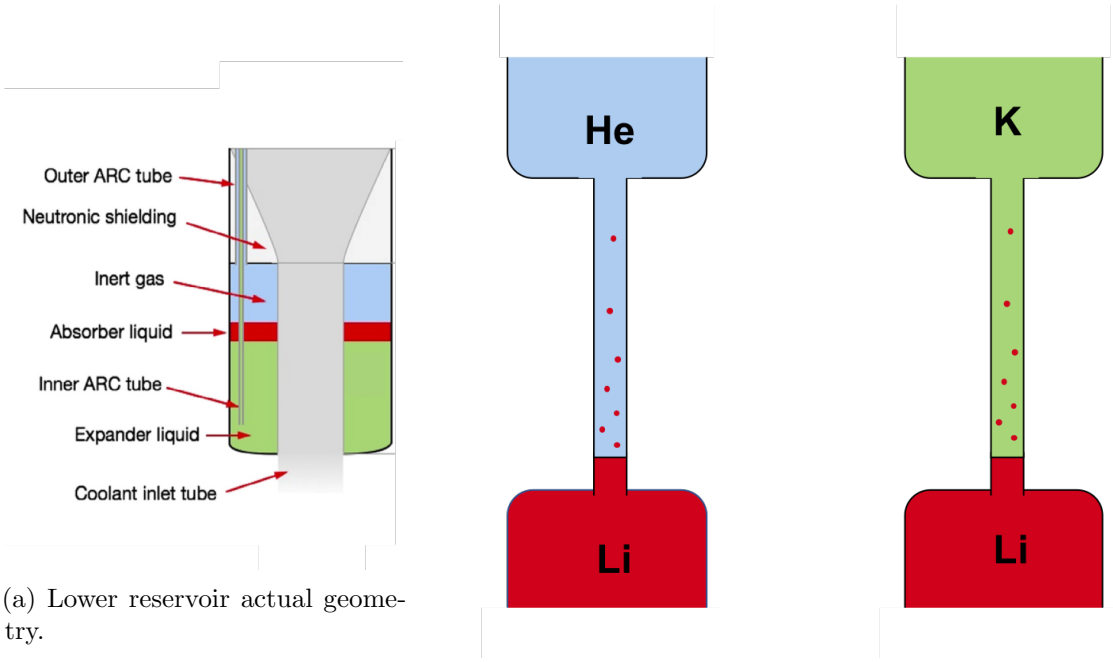

(a) Lower reservoir actual geometry.

(b) Simplified pathway (1)

(c) Simplified pathway (2)

Figure 82: Actual and simplified ARC system geometries used to study the impact of dissolved lithium in the core, fictitiously depicting the migration of lithium upwards into the active core.

9.4 Depletion of lithium reservoir inventory

With both diffusion and transmutation of lithium taking place, it is important to ensure that the lower reservoir maintains enough inventory to assure adequate actuation strength. This section investigates this concern.

9.4.1 Lower reservoir depletion through mass diffusion

The amount of lithium leaving the lower reservoir can be determined according to Fick's first law:

$$J_{Li}(z) = -D\frac{dN_{Li}}{dz} \tag{40}$$

Under the assumption that the lithium profile is dominated by diffusion, the concentration gradient can be evaluated with Equation 33. Although this assumption was conservative for estimating the neutronic penalty and tritium production, it is not conservative for estimating the amount of lithium diffusing from the lower reservoir. Figure 84 shows that the flux depletion mechanism may play a larger role than mass diffusion in high fission-power regions. Because flux depletion reduces the lithium concentration, it will increase the diffusion of lithium into the active core. This may be accounted for by modifying the setup to have the infinite sink for lithium atoms at the core midplane rather than the top of the core, representing a neutron flux that is strong enough to remove all lithium atoms at this location. In this way, the flux of lithium atoms from the lower reservoir will be doubled.

To determine the absolute rate of lithium leaving the lower reservoir, the interfacial area needs to be specified. Figure 87 shows the rate of lithium loss from the lower reservoir due to mass diffusion as a function of the inner ARC tube diameter for a range of diffusion coefficients. This figure demonstrates the need for an accurate diffusion coefficient. Unfortunately no experimental data could be found for lithium diffusion in either liquid potassium or gaseous helium. For diffusion between liquids, the diffusion coefficient can be estimated using the semi-empirical Wilke-Chang correlation, which has been found to

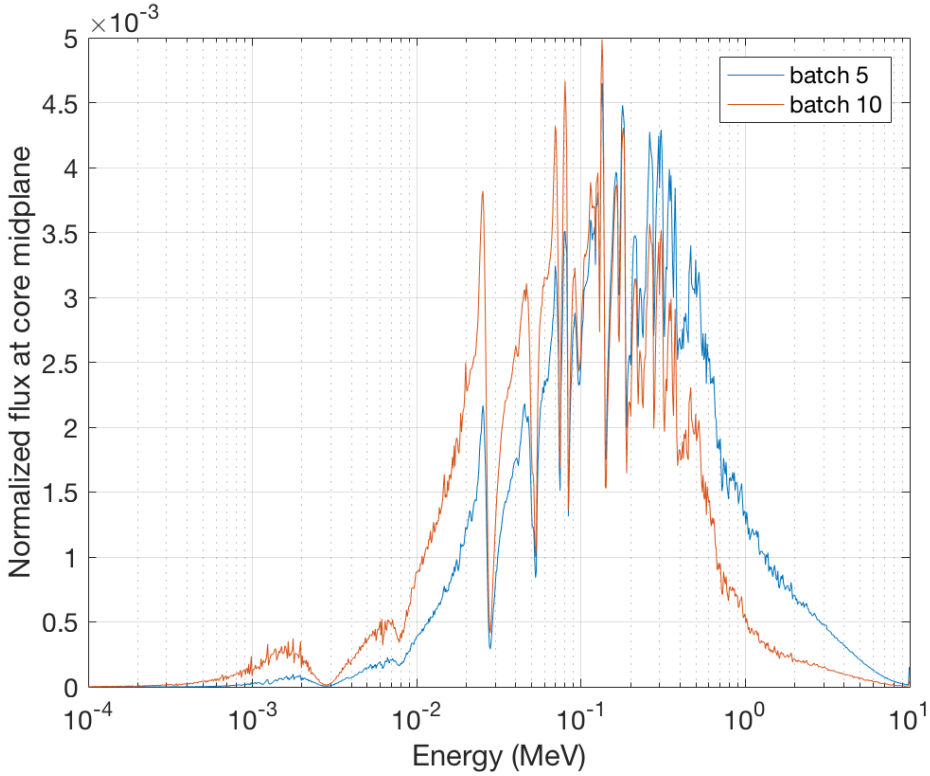

Figure 83: Normalized neutron spectra at two radial points within the B&B core. Batch 5 corresponds to a position close to the high flux zone and has experienced 12 burnup cycles, while Batch 10 corresponds to a position close to the core periphery and has experienced 2 burnup cycles.

predict diffusion coefficients to within roughly 20% [32] for a variety of organic fluids, although experience with liquid metals is not well characterized. However, diffusion coefficients are generally on the order of 10^{-10}-10^{-8} cm^2/s for a wide variety of liquid-liquid diffusion systems [32].

To assess the significance of these results, it is necessary to determine how much lithium will be lost during an assembly's lifetime. For the core under consideration, each assembly is in-core for 12 cycles of 2.5 years. Using the highest diffusion rate from Figure 87 over the entire assembly residence time, 3.3E+19 atoms of lithium are predicted to diffuse out of the lower reservoir. Converted to volume at the temperature of the lower reservoir, this corresponds to 5.6E-4 cm^3. The minimum lithium volume stored in the lower reservoir can be estimated by the volume of the inner ARC tubes, calculated to be 1590 cm^3 for the case of a single assembly with three ARC tubes. From this comparison, the comparatively small volume of lithium that will be lost to diffusion is considered negligible.

9.4.2 Lower reservoir depletion through neutron transmutation

Most of the lithium nuclei lost to transmutation will be split into nuclei of tritium and helium, both of which may take on gaseous forms. This study assumes that the gaseous nuclei generated are either kept in solution in the lower reservoir or accumulated in the inert-gas region of the ARC system such that they do not interfere with ARC system operation.

The amount of lithium lost to neutron transmutation can be determined in a manner similar to that which was used to quantify the ex-core tritium production in Section 9.3.2, except using the total transmutation cross-section as compared to the tritium production cross-section. The number of lithium atoms lost to transmutation over the course of an assembly's residence time is predicted in Table 16. As the lower shield thickness is increased, the amount of lithium lost to transmutation decreases. With a 5

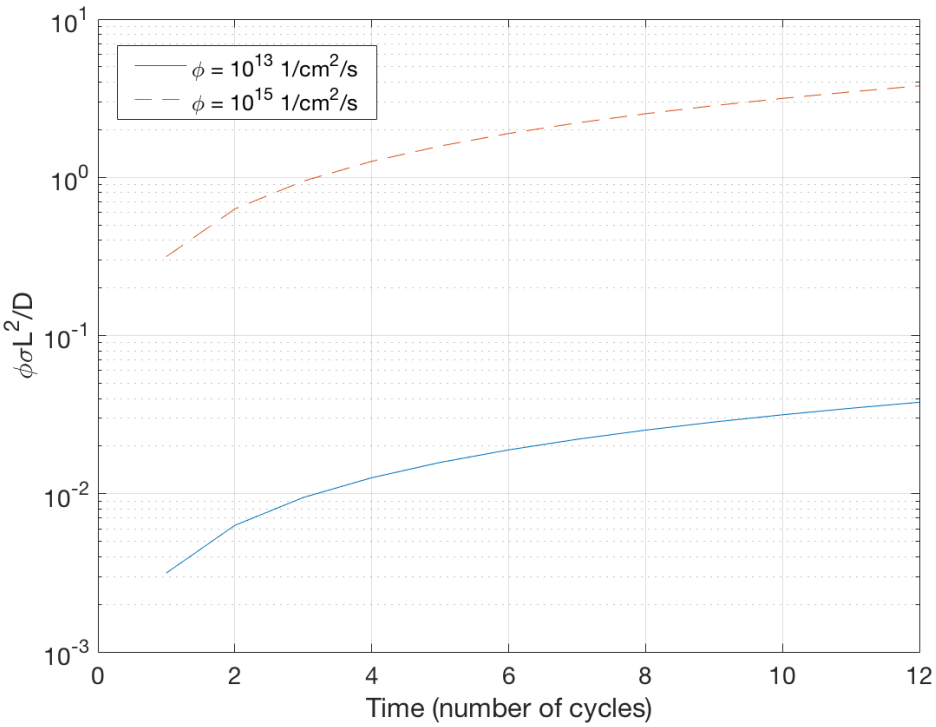

Figure 84: Dimensionless ratio as a function of residence time in the core for two different values of neutron flux.

cm thick lower shield, the volume of lithium lost is nearly 7 cm^3. This is nearly five orders of magnitude more than the volume lost to mass diffusion, although this amount can be brought down by more than an order of magnitude by increasing the lower shield thickness by 10 cm. Regardless, even with only a 5 cm thick lower shield, the volume of lithium lost to transmutation is more than two orders of magnitude smaller than the estimate for the lower reservoir lithium inventory of 1590 cm^3. This result implies that the amount of lithium lost to transmutation is likely less limiting than constraints imposed by tritium production outlined in Section 9.3.2, although still it should be adequately accounted for in the design process.

Table 16: Amount of lower reservoir lithium lost to transmutation, assuming the reservoir is located immediately below the lower shield and its lithium is 100% enriched in ^{6}Li.

Lower shield thickness (cm)	Average lithium transmutation rate per assembly (1/s)	Volume of lithium lost over assembly residence time (cm^3)
5	3.52E+14	6.65
10	9.60E+13	1.81
15	2.88E+13	0.54
20	1.19E+13	0.23

9.5 Validation of Infinite Sink Assumption

In previous analyses, two different assumptions were employed, each conservative for the analysis to which it was applied:

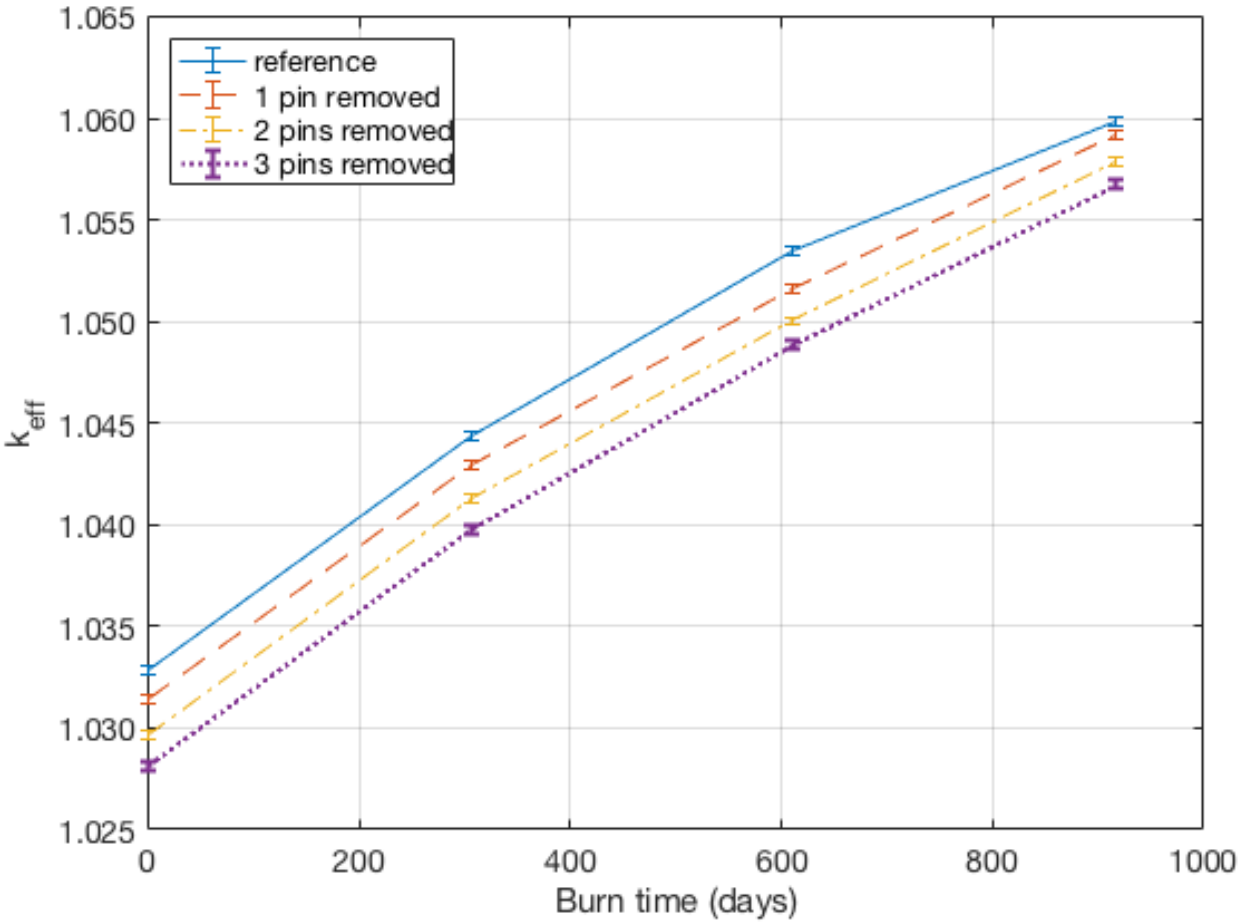

Figure 85: k_{eff} evolution in the equilibrium cycle with the fuel removed from a number of pins.

1. Neutron flux depletion mechanism is less important than mass diffusion mechanism (Section 9.2.3)
2. Neutron flux depletion mechanism dominates mass diffusion mechanism at the core center (Section 9.4.1)

In Case (1), it was assumed that the upper reservoir could act as an infinite sink for lithium atoms. This assumed boundary condition needs to be validated. In Case (2), the boundary condition is set to give an upper bound estimate, and no validation is necessary.

Using Equations 33 and 40, the amount of lithium in the upper reservoir can be determined as a function of assembly residence time, as shown in Figure 88 for a range of upper reservoir volumes and the same setup used in Section 9.4 (i.e. three ARC tubes per assembly, $D = 10^{-8}$ cm^2/s, and inner ARC tube radius $r = 0.75$ cm). Also depicted are the solubility limits of lithium in potassium at 510°C and 200°C (upper reservoir temperatures at standard operation and refueling, respectively) as determined by Equation 34.

Figure 88 shows how the volume of the upper reservoir can make an impact on the validity of the assumption that the upper reservoir acts as an infinite sink. As outlined in Section 4, typical upper reservoir sizes are likely to be on the order of 500 cm^3. This puts the amount of lithium dissolved in the upper reservoir more than 2 orders of magnitude below even the refueling temperature solubility limit. This provides validation to the infinite sink assumption used in Section 9.2.3.

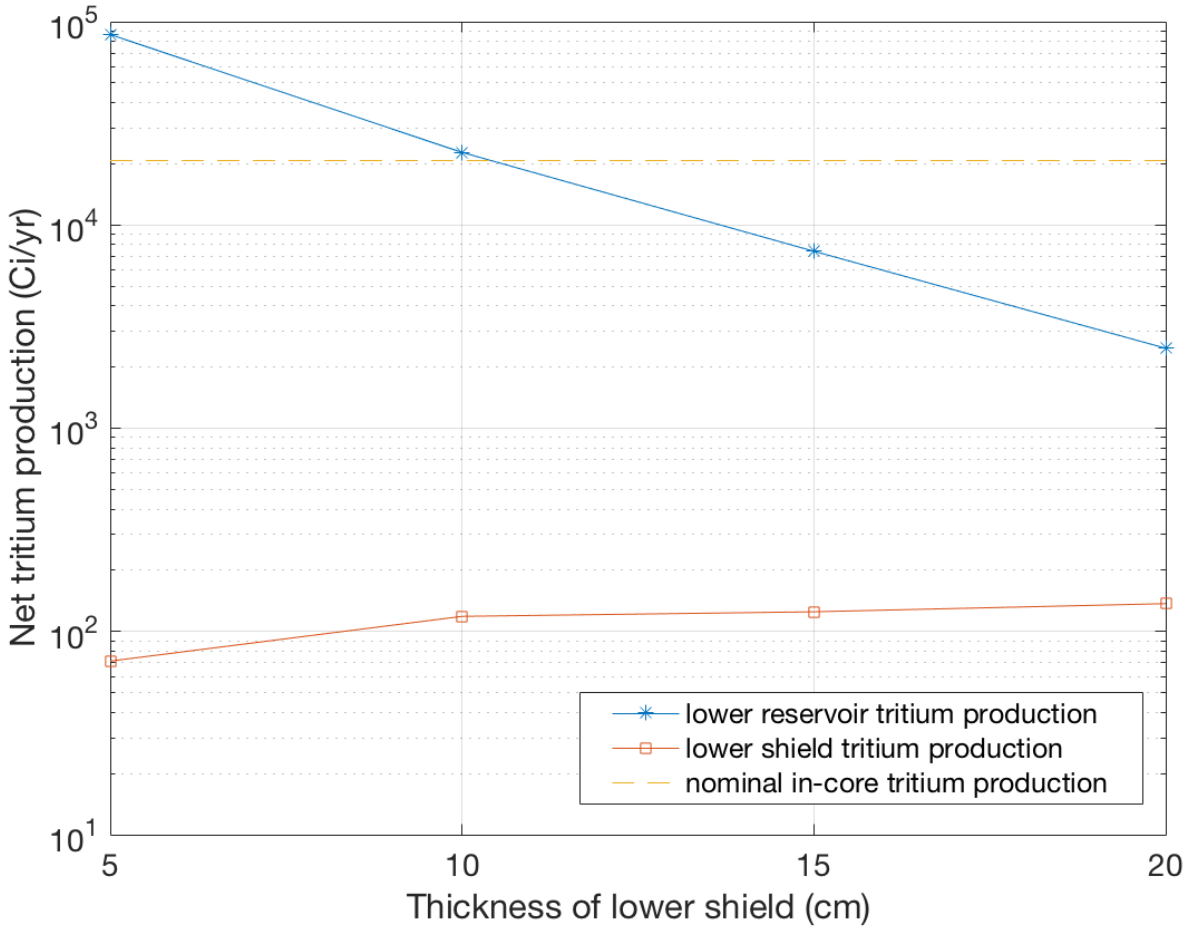

Figure 86: Amount of tritium produced in the lower reservoir and lower shield as the lower shield thickness is increased, as well as the nominal amount produced in-core.

9.6 Impact of System Breach

The potential impacts of a breach in the ARC system have been evaluated as part of this task. In the case of any breach, it is expected that the system will be rendered ineffective due to depressurization and potential loss of fluids. Because ARC systems will be incorporated into a large fraction of core assemblies, the systems are highly redundant and the breach of a small number of systems should be tolerable. However, it is important to know if and when systems are breached. To this end, the core cover gas and coolant chemistry should be monitored for the ARC system fluids. By tagging the ARC system inert gas with unique blends of xenon gas, it may be possible to determine which particular ARC system has been breached. In any case, if an ARC system is breached, it is likely that system fluids will escape into the core coolant, and the location of the breach will play an important role in the consequences. This study begins by evaluating how an ARC system may be breached, and then moves to evaluate the consequences of such a breach.

ARC systems may be conceptually divided into three regions: (1) upper reservoir, (2) lower reservoir, and (3) ARC tubes. The ARC tubes are similar in geometry and location to fuel pins, and therefore failure mechanisms in this region were evaluated along the same lines. For fuel pins, the primary failure mechanisms are (1) Fuel-Cladding Mechanical Interaction (FCMI), (2) Fuel-Cladding Chemical Interaction (FCCI), (3) over-pressurization, and (4) rod fretting against spacers or wire-wraps. In ARC tubes, FCMI

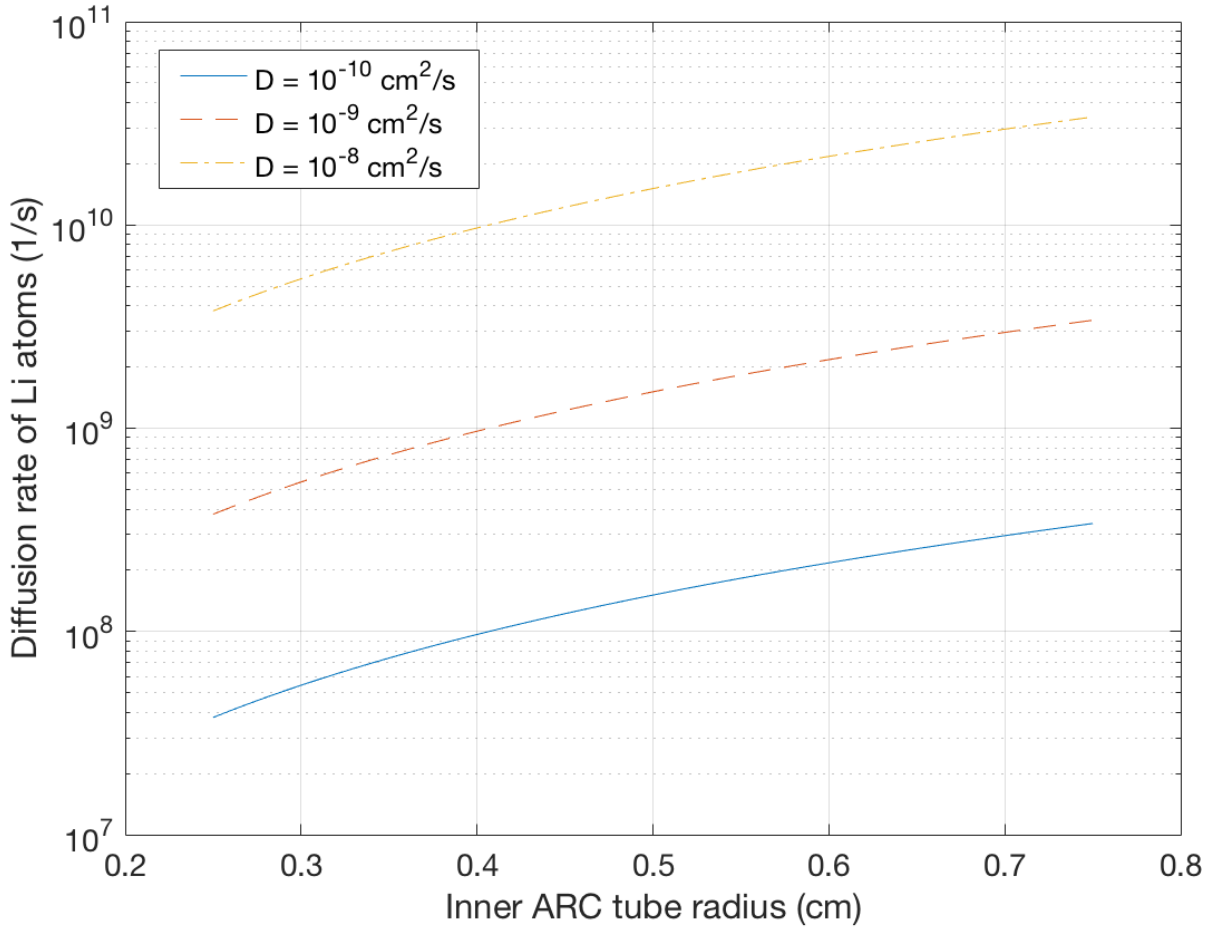

Figure 87: Rate of diffusion of lithium atoms from the lower reservoir into the active core as a function of the radius of the inner ARC tube for different assumed diffusion coefficients assuming an infinite sink for Li atoms at mid-core. All curves assume three ARC tubes per assembly.

is not an issue because the ARC fluids are all liquids. Additionally, FCCI is not of concern because all ARC fluids have very low corrosion rates with steels. Finally, over-pressurization is not likely to occur because there is no heat source inside the ARC tubes, avoiding excessive temperatures that lead to high pressures. Therefore a breach is most likely to occur as a result of rod fretting, although this phenomenon can be controlled to some degree by limiting peak flow rates. No credible failure mechanisms could be devised for either the upper or lower reservoir regions, and therefore this study considers breaches only in the ARC tube region.

It is assumed that ARC systems are loaded at higher pressure than the surrounding coolant, otherwise a breach would lead to inwards leakage of sodium into the ARC tubes. When an ARC system is breached, it is expected that depressurization could lead to any of the three ARC fluids leaking into the coolant. Of the three fluids, the inert gas has the highest potential for undesirable consequences due to the formation of coolant voids. Leakage of the absorber fluid is undesirable and may force a shutdown, but is more likely to cause a negative reactivity insertion due its capture cross-section. Both situations are examined in this section.

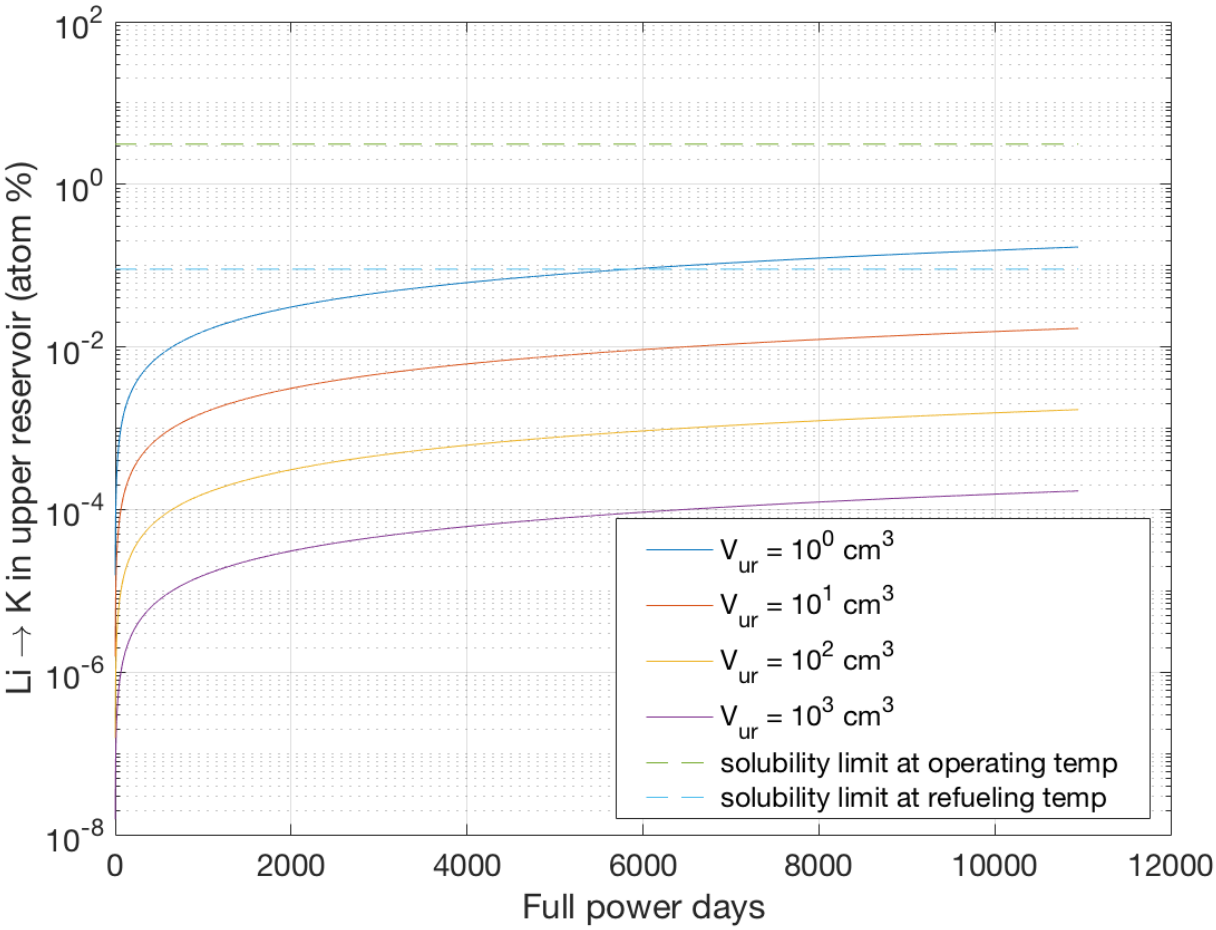

Figure 88: Atom percent of lithium dissolved in upper reservoir potassium as a function of time for various upper reservoir volumes, along with the solubility limits at operating and refueling temperatures.

9.6.1 Leakage of Inert Gas

To evaluate the reactivity insertion that may occur if the inert gas leaks into the coolant, it is necessary to know the volume and rate of leakage. Because these factors depend on the specific conditions of the breach, this study takes a simplified, conservative approach. When a breach occurs, it is assumed that the entire volume of gas leaks instantly into the coolant, forming a cohesive bubble that moves upward with the coolant flow. Although this is not physically accurate, this assumption leads to the worst case reactivity insertion, and is therefore a bounding estimate.

The volume of leaked gas is dependent on the axial location of the breach, the radius of the ARC tubes, and the pressure ratio between the ARC tubes and the coolant. To determine the gas bubble volume in the coolant, a set of ideal gas relations can be used, where P is pressure, V is volume, n is the number of moles, R is the universal gas constant, T is temperature, and the subscripts Ai, Af, and c refer to the ARC tubes in initial state before breach, the ARC tubes in final state after breach, and the coolant, respectively.

$$P_{Ai}V_{Ai} = n_{Ai}RT_{Ai} \tag{41}$$

$$P_{Af}V_{Af} = n_{Af}RT_{Af} \tag{42}$$

$$P_c V_c = n_c R T_c \tag{43}$$

It is assumed that P_c is known, and that upon breach the pressures are equilibrated, leading to $P_{Af} = P_c$. V_{Ai} is taken as the volume of gas in the ARC tubes, and can be calculated as in Equation 44, where r_o is the outer radius of the gas region (assumed known), r_i is the inner radius of the gas region, and h is the height of the gas region (taken to be the active core height).

$$V_{Ai} = \pi h [r_o^2 - r_i^2] \tag{44}$$

The number of moles of gas that make up the gas bubble can be determined through a molar balance as in Equation 45.

$$n_c = n_{Ai} - n_{Af} \tag{45}$$

This study will perform parametric sweeps over P_{Ai} and r_i, and therefore the unknowns are n_{Ai}, n_{Af}, n_c, V_{Af}, and V_c. This is an underdetermined system, and therefore an assumption must be made in order to eliminate one of the unknowns. The final assumption is that the volume of gas in the ARC tubes after breach is reduced by the portion of volume below the axial level of the breach. This assumption effectively means that the levels of the absorber and expander fluids will rise upwards to the level of the breach as the pressure equilibrates. Although it is possible that this may not happen if the pressure in the ARC fluids is not high enough, making this assumption causes the maximum amount of inert gas to be expelled into the coolant, giving an upper bound on the reactivity insertion that may result. This assumption can be formulated into Equation 46, where h_{breach} is the axial height of the breach:

$$V_{Af} = V_{Ai} - \pi h_{breach} [r_o^2 - r_i^2] \tag{46}$$

Once the volume of the gas bubble is known, the reactivity insertion from such a bubble can be determined using a calculated coolant reactivity worth curve for the system under consideration, as in Figure 46. Consistent with the other studies in this section, the reactivity insertion is evaluated for the large B&B core. This core has a very strongly positive void feedback, with nearly \$15 inserted during full core voiding, and therefore it is expected that a breach in the ARC systems of this core would be worse than in the majority of other SFR designs.

The void worth is strongly peaked at the axial core center, implying that a breach at the core center may lead to the largest reactivity insertion. This may not be strictly the case, however, as the amount of gas escaping through the breach increases as the height of the breach increases. The maximum reactivity insertion may therefore result from a breach somewhat above the core midplane, and this study therefore examines all axial positions.

Figure 89 shows a typical reactivity insertion curve determined by solving the set of equations above to determine the volume of the gas bubble, using the volume to find the mass of sodium displaced, and then multiplying that mass by the reactivity worths depicted in Figure 46. Although the void worth curve is generally symmetric, the curve of reactivity insertion is not due to the fact that the gas bubble is assumed to flow upwards through the core with the coolant. Therefore, bubbles which form below the highest-worth position will eventually flow past the region of highest worth, and thus the bubble's volume should be multiplied by the highest worth. For breaches that occur above the highest-worth position, this is not the case, and they are multiplied with the worth corresponding to the position of the breach.

Due to the fact that bubble size is larger as the breach height increases, the maximum reactivity insertion occurs when the breach takes place slightly above the highest-worth position. Because different ARC system designs will have different pressures and tube diameters depending on the desired actuation characteristics, a parametric study is performed to determine the sensitivity of the maximum reactivity insertion to different ARC tube radii and pressures. Figure 90 shows the results of this parametric study in the B&B core.

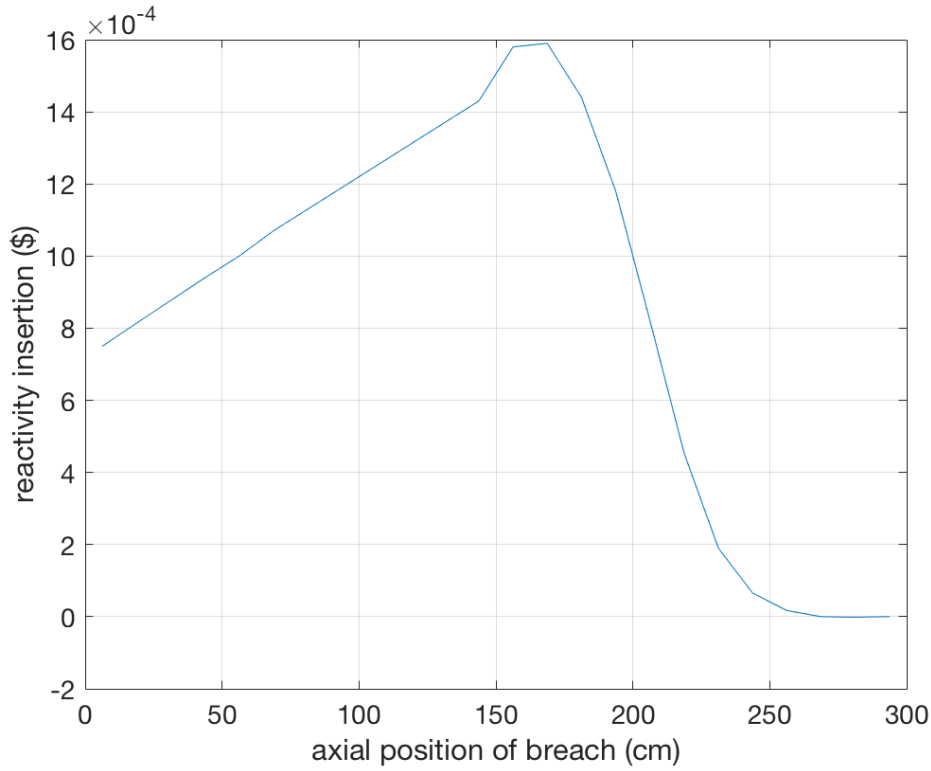

Figure 89: Reactivity insertion as a function of breach position for the breach of a single ARC system in the B&B core with $r_i = 0.23$ cm, $P_{Ai}/P_c = 1.5$, and three ARC tubes per assembly.

As the ARC tube pressure increases, the maximum reactivity insertion increases nearly linearly, as is expected for an ideal gas. As r_i is increased, the volume of the gas in the ARC tubes decreases, causing the maximum reactivity insertion to decrease proportionally to the volume. Therefore the largest reactivity insertions are to be expected from ARC systems at high pressure that have large volumes of gas. This parametric study shows that the largest reactivity insertion that could be expected from a single failed ARC system is only roughly 0.4¢, even under highly conservative assumptions. This is orders of magnitude smaller than the UTOP transients examined in Section 7, which were adequately handled even without ARC system inclusion. Additionally, this type of reactivity insertion is only very brief, as the gas bubble would flow with the coolant up and out of the core within a matter of seconds. Thus it is judged that the breach of an ARC system does not pose significant safety concerns, as long as a sufficient number of redundant ARC systems are functional to supply the negative reactivity insertion required by further transients.

9.6.2 Leakage of Absorber Fluid

In the case that the absorber fluid rises up to the level of the breach when pressures equilibrate following a breach, it is likely that some amount of the absorber fluid will be released into the coolant. Such an occurrence will result in absorber fluid flowing upwards through the core mixed with the coolant, where it will either de-mix in the hot pool and stratify near the cover gas due to its lower density or dissolve in the coolant sodium. For any lithium that dissolves in the coolant sodium, the amount will be so small that the lithium will be heavily diluted, leading to a negligible long-term impact. Therefore, leakage of absorber fluid will lead to only a temporary reactivity impact, similar to that for leakage of the inert gas.

This section aims to quantify the worst-case reactivity insertion which may occur from leakage of the absorber fluid into the coolant. This is done by performing direct perturbation calculations at BOEC and

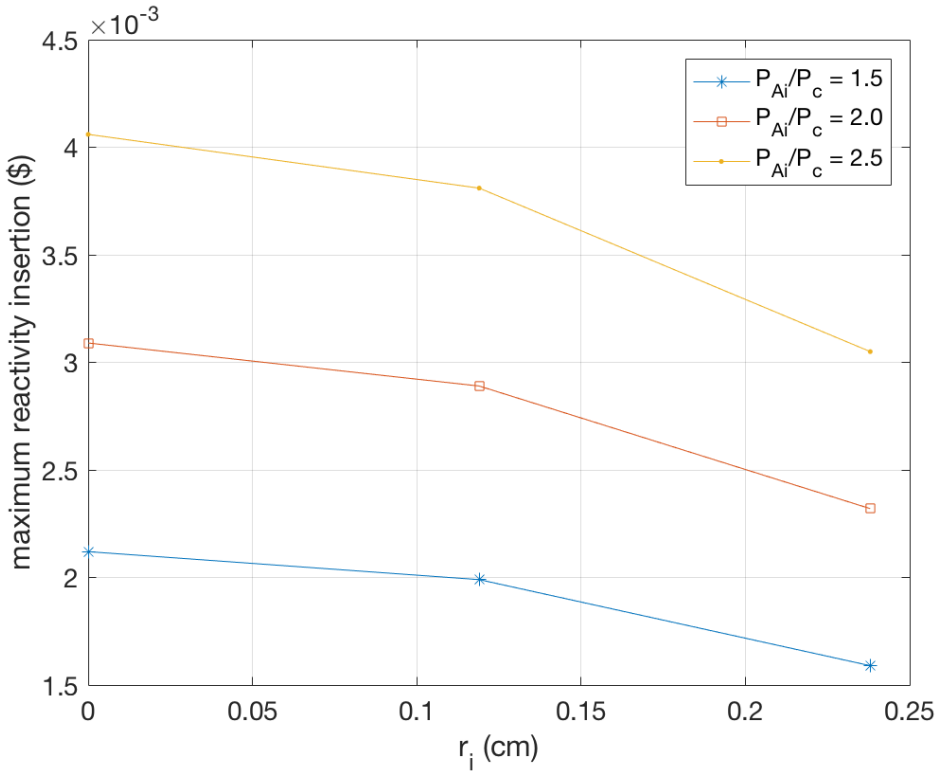

Figure 90: Maximum reactivity insertion as a function of the inner gas volume radius for a variety of ARC tube initial pressures, assuming the breach of an ARC system with three ARC tubes.

EOEC to determine the core reactivity with the entire absorber fluid inventory from a single ARC system replacing the coolant in the region of highest reactivity worth. The ARC system design assumed for this calculation is the same as that used in Section 9.4, i.e. three ARC-tubes with a lithium inventory of 1590 cm^3. Table 17 shows the maximum reactivity penalty at BOEC and EOEC.

Table 17: Difference in k_{eff} of the B&B core at BOEC and EOEC with a single ARC system's worth of absorber fluid at the location of highest worth.

	Nominal	With Leak	Reactivity Insertion ($)
BOEC	1.03319 ± 0.00022	1.03150 ± 0.00021	-0.46
EOEC	1.06026 ± 0.00021	1.05856 ± 0.00021	-0.47

At both BOEC and EOEC, leakage of a single ARC system's absorber fluid results in a negative insertion of nearly half a dollar. This rather large result is a product of the assumption that all of the inventory leaks instantly combined with the strongly localized worth seen in the B&B core, as reflected in Figures 44 - 46. However, it should be stressed that such a reactivity insertion will be temporary, as the absorber fluid will flow with the coolant up and out of the core. Therefore, a leak of the absorber fluid into the core is likely to result in a sudden and quick negative reactivity insertion. In order to examine what type of impact may be seen from such a reactivity insertion, the B&B transient model is modified to reflect this scenario. An insertion of -$0.47 is imposed beginning at 11 s and lasting for just 1 s, to reflect the fact that the core flow of roughly 10 m/s will wash the absorber fluid out of the core in less than 1 s. The results of this scenario are shown in Figures 91 - 93.

The assumed reactivity insertion causes a significant reduction in core power, although the temporary

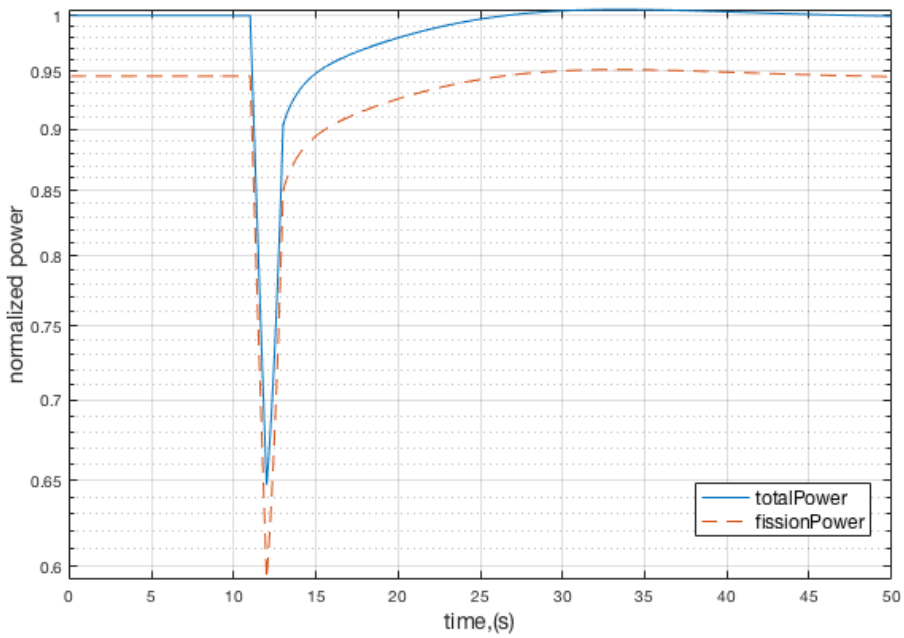

Figure 91: Power transient response to a breach in a single ARC system leading to a sudden leak of absorber fluid into the coolant.

nature of the insertion allows for the responding feedback mechanisms to bring core power back up to nominal levels very quickly. The resulting temperature response is very slight, with no negative implications expected. Due to the large power decrease, the transient may be detectable in core flux or outlet temperature measurements, which may be useful for detecting the breach of an ARC system. However, the severe assumptions made in this scenario mean that only the very worst case breach will lead to such a notable response, and therefore detection of an ARC system breach may be more difficult in practice.

It should be noted that this strong, localized reactivity transient may have important spatial effects that are not captured by this study, which employs a point-reactor kinetics model. To evaluate the possibility for spatial effects, a spatial kinetics model should be used in future studies.

9.7 Extension of Results to the ABR Core

Although the analysis of this section was performed entirely for the B&B core, many of the results can be directly extended to the ABR core. For instance, there is no reason to think the relative reactivity penalty should be any larger in the ABR core than what was determined for the B&B core. Similarly, the amount of lithium lost to diffusion into the expander fluid and the impacts of a possible breach should remain small. However, one significant difference will be in the amount of tritium produced in the lower reservoir. Because the B&B core has very low axial leakage probability, the flux level at the lower reservoir is extremely low. Conversely, the ABR core has a much higher axial leakage level, which will increase the rate of tritium-producing reactions in the lower reservoir. While the method of adding shielding between the active core and lower reservoir will still be effective, more shielding material may be required in order to achieve acceptable tritium production levels. In a similar manner, the depletion rate of lithium in the lower reservoir will be increased in the ABR core. The extra shielding required will lead to an increase in core height and an associated increase in pressure drop which should be adequately considered.

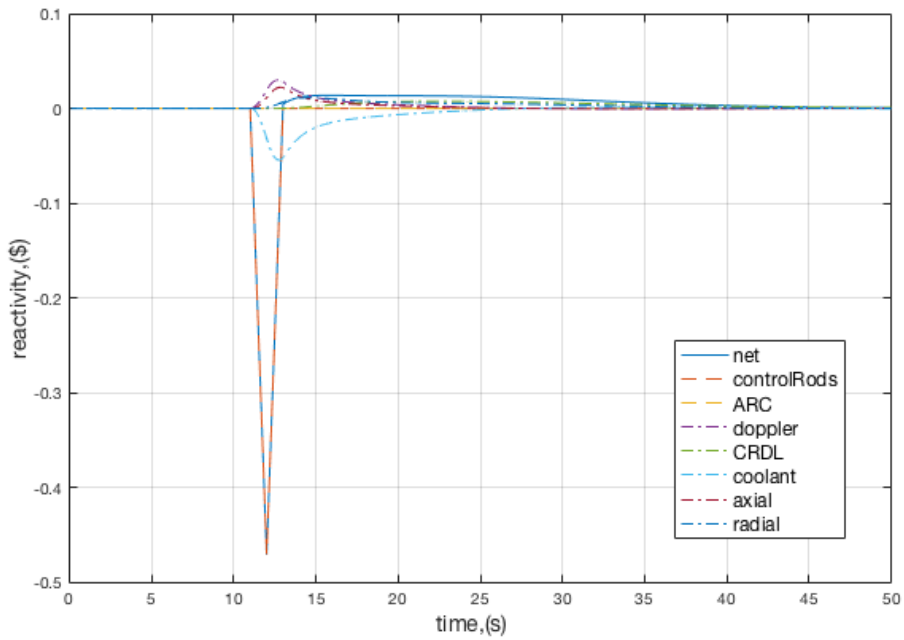

Figure 92: Reactivity transient response to a breach in a single ARC system leading to a sudden leak of absorber fluid into the coolant.

10 Improving Economic Performance

Sections 7 - 8 showed that the ARC system may provide benefits in terms of improving transient performance. This section examines a few reactor design modifications to understand if the ARC system can also enable improved economic performance. The goal of this section is to demonstrate that ARC systems may enable more aggressive designs without degrading transient performance to worse than the case without ARC system inclusion. In other words, the extra temperature margin enabled by the ARC system is traded against design performance improvements. Because complete passive safety was not achieved in the B&B core, only the ABR is examined.

10.1 ARC System Design

The results of Section 7 identified the best ABR ARC system design to have w =\$0.87, ΔT_{act} =10°C, and S =65°C. The study also showed there to be a large design space available within this particular core as long as the actuation strength was not too large. Therefore, this section assumes this same optimal ARC system design for the different design modifications examined.

10.2 Core Power Uprate

Due to the procedure that was used to optimize the various ABR designs outlined by Hoffman et al. [33], the settled design has roughly 17% margin in the power level before reaching the limiting constraint of fuel melting, including hot channel factors for film, cladding, gap, and coolant uncertainties. This margin effectively means that the core power can be uprated from 1000 MW to 1170 MW without violating steady-state safety constraints. The possibility of uprating the core power while maintaining acceptable transient performance through the use of the ARC system is the focus of this section. This will be evaluated by simply increasing the core power, with an assumed proportional reduction in cycle length to account for the limited core excess reactivity at BOC and higher rate of burnup accumulation. By

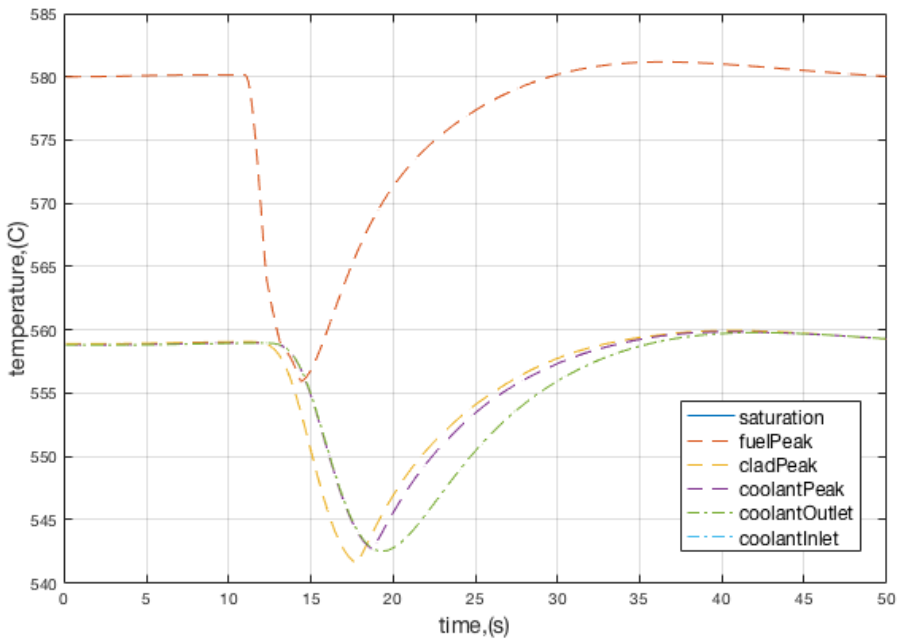

Figure 93: Peak temperature transient response to a breach in a single ARC system leading to a sudden leak of absorber fluid into the coolant.

uprating the core power without altering the design, economic performance is expected to improve through better economies of scale.

In addition to the shorter cycle length, the power uprate is expected to have a couple other impacts on core performance. First, the power density increase will lead to higher concentrations of short-lived fission products and a corresponding decrease in core reactivity. Second, the higher power density will reduce the amount of ^{241}Pu lost to beta decay (13 year half-life), and thus will provide a reactivity increase that may somewhat counteract the fission product effect. Finally, the higher core temperatures, especially in fuel, will have impacts on doppler broadening and further reduce core reactivity. For these effects, it is expected that a small adjustment of loading enrichment or cycle length will be enough to compensate the reactivity change. It is expected that the impact of these effects on the core dynamics will be small, as the core spectrum, neutron leakage, and fissile material loading are expected to be largely unchanged.

Table 18 shows the peak coolant and fuel temperatures during the first 30 minutes of each transient for the original core, the uprated core, and the uprated core with ARC system included. As is typical, peak fuel temperatures in the ULOF and ULOHS transients occur at the initial steady-state, while peak fuel temperature typically occurs shortly after full control rod withdrawal in the UTOP. Peak coolant temperatures in the ULOF and UTOP are seen to occur early after transient initiation, while peak coolant temperature is reached in the ULOHS at the new steady-state after the transient has equilibrated. These general behaviors are consistent over all cases reported in Table 18.

The power uprate causes increases of roughly 20-25°C and 35-40°C in peak coolant and fuel temperatures, respectively. The power increase does not lead to any coolant boiling or fuel melting, as is expected based on the results Hoffman et al. [33] that initially motivated the power uprate. The inclusion of the ARC system into the uprated core allows for peak temperatures to be brought down substantially, below those seen in the nominal core without the ARC system. With the exception of the peak fuel temperature in the ULOF and ULOHS, all peak temperatures are brought down, with coolant temperatures reduced by at least 30°C compared to the nominal case. No gains in peak fuel temperature are seen for the ULOF or ULOHS due to the peak fuel temperatures occurring before transient initiation.

Table 18: Peak temperatures in the three unprotected transients for the nominal and uprated cores, showing the impact of the ARC system.

	Power	ARC	ULOF	ULOHS	UTOP
Coolant (°C)	100%	no	819	690	631
	117%	no	841	711	665
	117%	yes	732	631	601
Fuel (°C)	100%	no	1724	1724	2062
	117%	no	1761	1761	2099
	117%	yes	1761	1761	1841

10.3 Flow Halving Time Reduction

Previous transient studies in the oxide ABR have assumed a pump coast-down halving time of 20 seconds in order to avoid boiling in the ULOF. While this assumed value is in line with similar studies in oxide cores (see for instance [34] [35]), it is expected that such long halving times will require the use of flywheels attached to the pumps [4], which is unattractive for a number of reasons. Flywheels are expensive, requiring large additions to standard centrifugal pump designs that increase the physical size and cost of the pump. Second, flywheels greatly increase the inertia of the pumps, making their steady-state power consumption significantly higher. Finally, according to the NRC it is widely recognized that flywheels have the potential to break off and become a "missile" [36]. The possibility of such a large object becoming a missile in the vicinity of the core cooling system poses safety risks that require extensive analysis and special considerations. Therefore if the use of flywheels can be avoided, significant savings are expected.

For most metallic SFRs with favorable transient characteristics, the pump halving time is on the order of 5 seconds [37] [28] with the pump itself providing enough inertia. This study aims to see if the oxide ABR can be designed with halving times on the order of those used for metallic cores while retaining acceptable transient performance through the use of the ARC system. To do this, the inertia of the primary pump is adjusted iteratively until the halving time during the initial pump coast-down period is roughly 5 seconds, while all other parameters, including the core power level, remain at their nominal levels.

Figures 94-96 show the ULOF results for the ABR with and without ARC system inclusion with a flow halving time of 5 seconds. Without the ARC system installed, the system reaches boiling within less than 30 s due to the large power/flow mismatch. As the pumps coast down, core power decreases much more slowly. This is due to the primary negative feedbacks, CRDL and radial expansion, being hindered by the poor thermal conductivity of the oxide fuel.

In the case with ARC system installed, the core power is brought down more rapidly due to the strong negative ARC system insertion, as shown by the yellow dashed line in Figure 95. Although early ARC system response is similarly hindered by the poor oxide fuel thermal conductivity, subsequent actuation is strong due to the specific ARC system design. For the results shown, $\tau = 1.3$ s, allowing for a rapid response once the elevated fuel temperature is communicated to the coolant. Even with this rapid response, no oscillatory behavior is seen. Figure 96 shows that the peak coolant temperature reaches its highest value around 30 s into the transient, with roughly 100°C of margin to boiling.

10.4 Extension of Results to Higher Conversion Ratio Cores

The results presented thus far have pertained to a burner-type reactor with conversion ratio equal to 0.66. This section gives qualitative discussion on the possibility of utilizing ARC systems in similar cores with higher conversion ratios, as in those explored by Hoffman et al. in [33], where kinetic parameters are calculated for designs having conversion ratios up to 1.0.

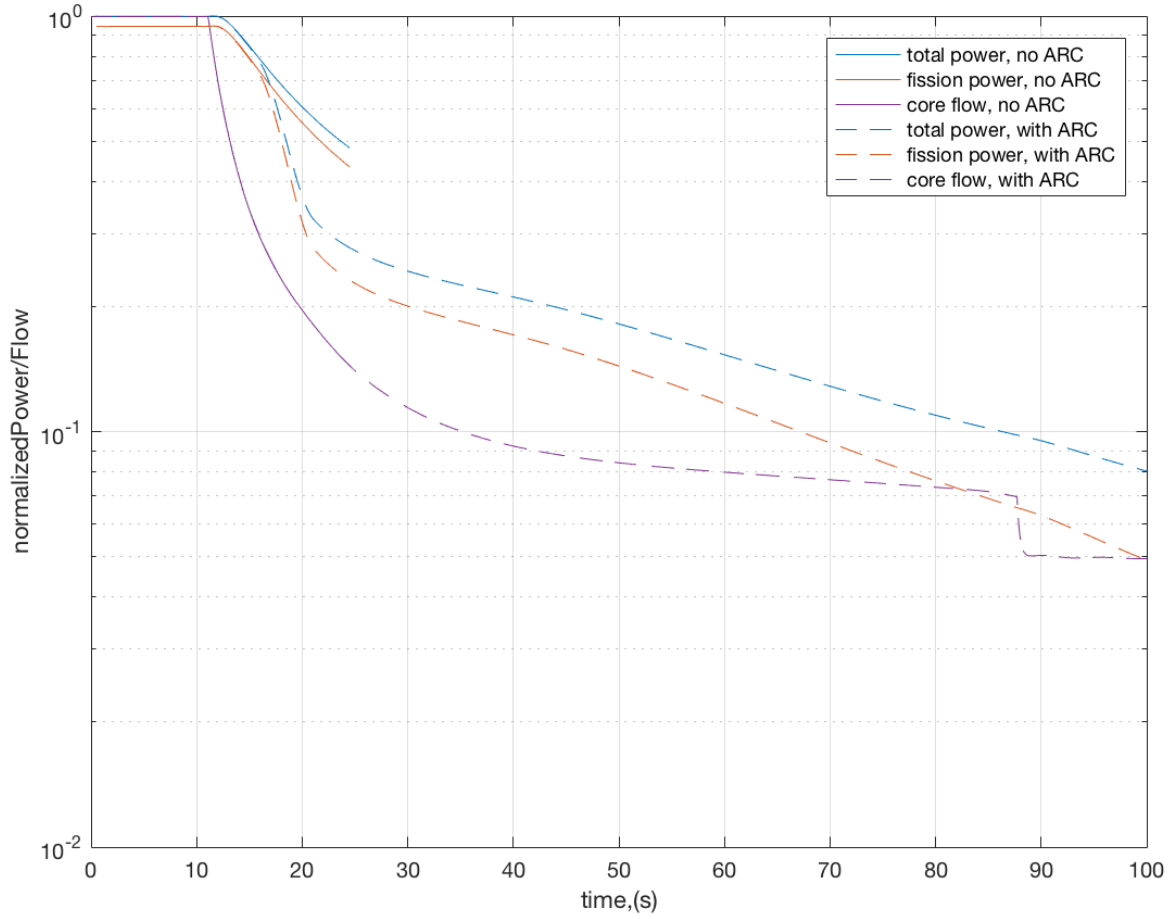

Figure 94: Power and flow in the oxide ABR with pump coast down halving time of 5 seconds, both with and without the ARC system.

As conversion ratio is increased, the reactivity swing approaches zero due to less excess reactivity at core loading. In addition, the coolant void worth, the only positive component of the transient feedback, decreases by roughly 2x as the volume fraction of coolant substantially decreases. The doppler coefficient also becomes stronger by roughly 40% as the amount of fertile material is increased. These three effects would combine to make the transients easier to handle in a higher conversion ratio core. On the other hand, as conversion ratio is increased, both the axial and radial expansion coefficients become less negative by about 50%. Because radial expansion is one of the strongest feedbacks in the overall response, this reduction could have significant negative implications on the transient response. Additionally, Hoffman shows that the prompt neutron lifetime decreases by roughly 20%, although this effect could be offset by the increase in the delayed neutron fraction by nearly the same amount.

Overall, the kinetics parameters for the oxide ABR change as the conversion ratio is brought up to 1.0, but these changes will likely have cancelling effects, leaving the transient response largely unchanged. Because multiple methods for avoiding oscillatory behavior in the oxide-fueled cores have been devised, it is likely that higher conversion ratio cores will maintain the design flexibility that was seen in the lower conversion-ratio core. In the end, this flexibility will likely allow the ARC system to play a similar role in improving the transient performance of higher conversion ratio cores.

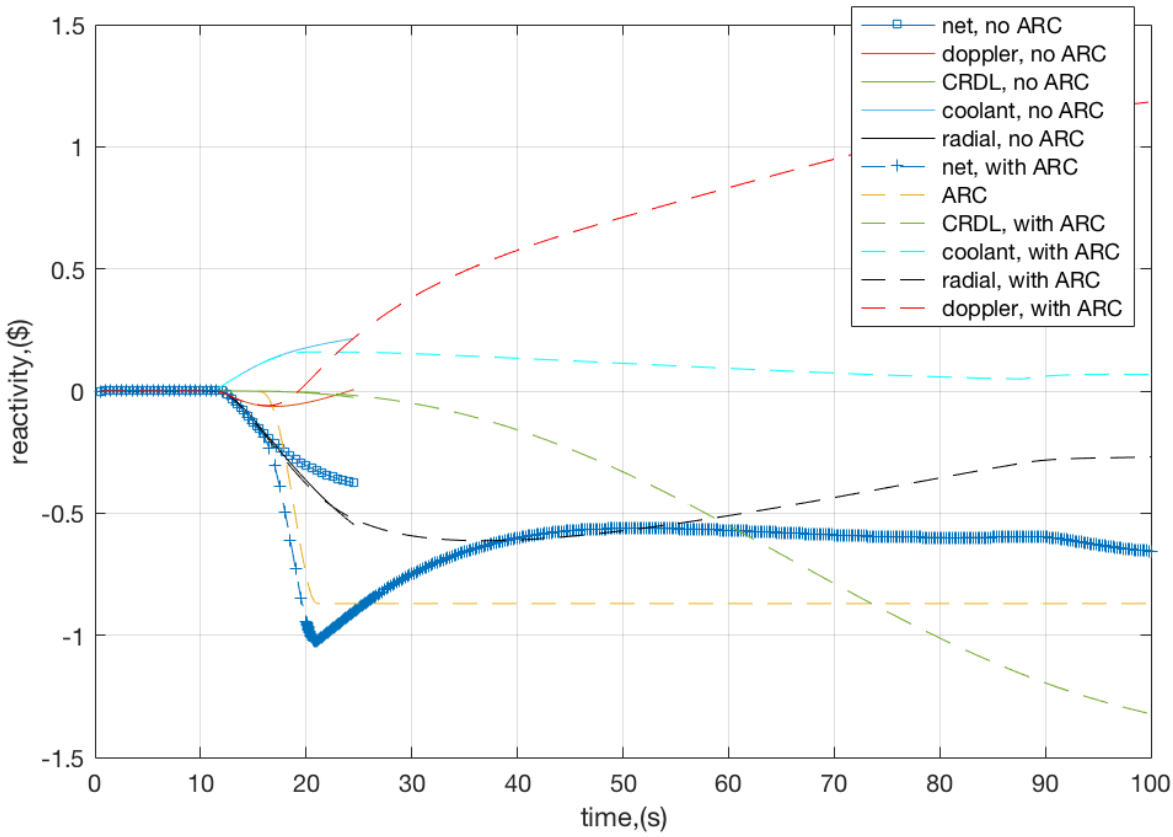

Figure 95: Core reactivity in the oxide ABR with pump coast down halving time of 5 seconds, both with and without the ARC system.

10.5 Extension of Results to Metallic-fuel Cores

Although not specifically examined in this study, it is expected that similar results may be extended to certain classes of metallic-fueled cores as well. The core examined in Section 8, although metallic, has unfavorable kinetic parameters. Due to its very strong positive coolant void feedback, the B&B core experienced oscillatory behavior with standard ARC system designs, and thus economic enhancements to that core were not explored. However, for smaller metallic-fueled designs it is likely that economic performance enhancements could be achieved. Small SFR cores, such as EBR-II, can achieve a negative coolant density feedback, allowing them to have excellent passive safety performance at the expense of higher neutron leakage and lower breeding ratios. Because such a core can already cope with unprotected accidents, any ARC system added to the core could be modest to the point that there is no chance of inducing oscillations as were seen in the large breed-and-burn core. By incorporating ARC systems of modest reactivity worth, it is likely that the core volume could be increased without sacrificing the excellent passive safety performance, thus allowing for improved neutron economy as well as increased power level.

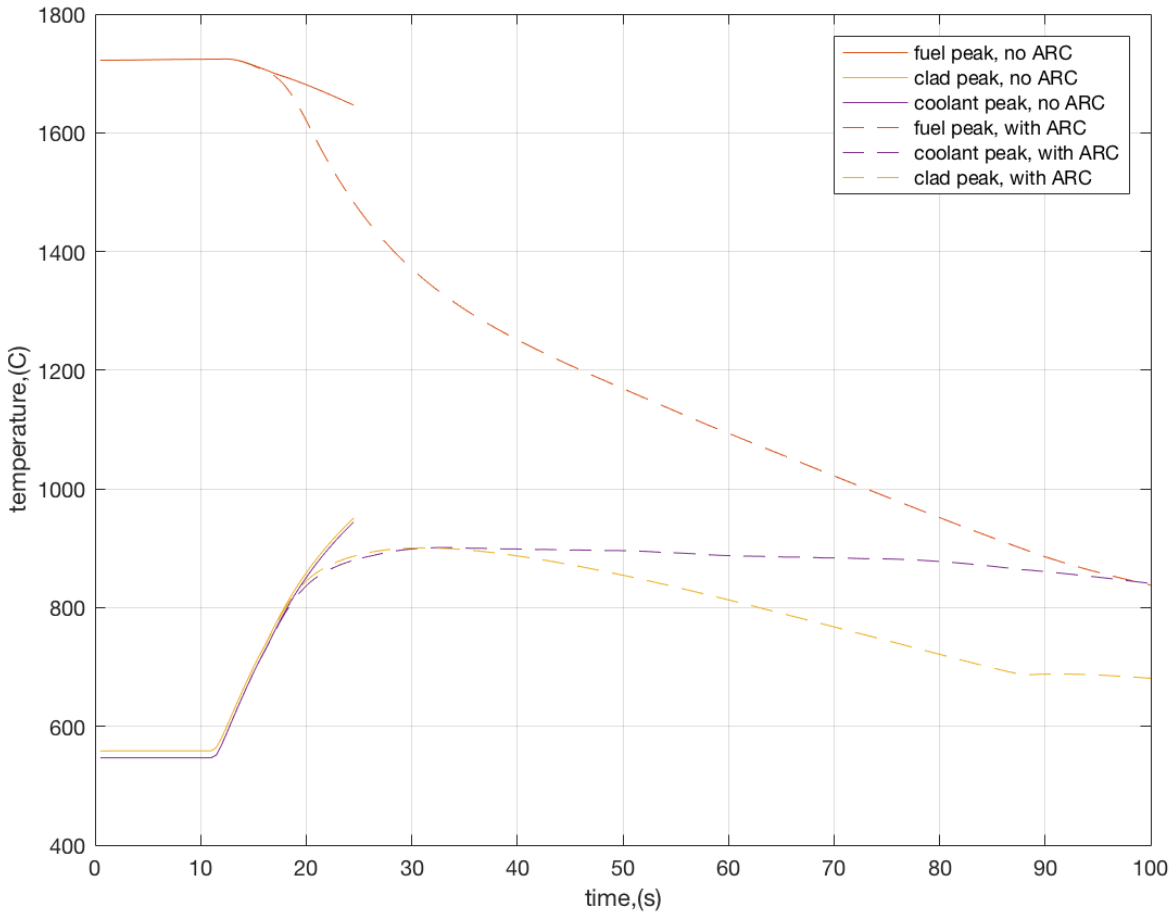

Figure 96: Peak temperatures in the oxide ABR with pump coast down halving time of 5 seconds, both with and without the ARC system.

11 Technology Gap Analysis

Throughout this work, either due to unknown information or particularly complicated physics, a number of assumptions have been made. Some of these assumptions are vitally important to the conclusions drawn, while others have more of a secondary impact or are only important for particular reactor systems. This section outlines these assumptions and frames them in the context of future work which should be performed before ARC systems can be utilized. In the end, the technology gaps are rated with respect to their importance and the difficulty of resolving them.

11.1 Technology Gaps

- **Solubility of Reaction Products in ARC System Fluids**: As the ARC system operates, lithium will be transmuted to tritium and helium. The current study has assumed that these reaction products will remain in solution of either the lithium or potassium fluids, but the actual behavior is poorly characterized. If tritium and helium do stay in solution, it is possible that they will impact the mutual solubilities of lithium and potassium, necessitating further study to ensure that mass diffusion of lithium does not increase. Otherwise if helium and tritium do not stay in solution, it is important to understand where they end up. The best case would be that they end up

in the upper reservoir mixed with inert gas, but they may also make their way into the expander fluid chamber of the upper reservoir, where a small gas bubble could form. This may have implications on the actuation characteristics of the ARC system, and should be fully investigated if the reaction products are found to precipitate out of solution. Such a study should account for temperatures at shut down as well, when the reaction products would be most likely to precipitate out.

- **Diffusion Coefficients of ARC System Fluids**: The diffusion coefficients of lithium into potassium and vice-versa are poorly characterized. As outlined in Section 9, these parameters may have a large impact on the amount of lithium lost from the lower reservoir. Although the current analysis shows it is unlikely to be a cause for concern, better characterization of the system diffusion coefficients will allow for more definitive conclusions to be drawn about absorber fluid depletion.

- **Solubility of Lithium in Potassium at Elevated Temperatures**: The solubility values used in this study do not fully cover the range of temperatures expected under transient conditions. In the case that an ARC system is actuated for an extended period of time, an elevated solubility may allow for non-negligible amounts of lithium to diffuse into the expander fluid. While it is likely that excessive amounts of lithium dissolved in the expander fluid will fall out of solution when temperatures are again reduced, this mechanism is not fully understood. The assumption is that any precipitate will fall back into the bulk lithium inventory, but it is possible that some amount of precipitate will remain in other regions of the ARC system, where it may lead to a reactivity penalty, additional tritium production, and decreased ARC system worth. The first step to understanding this behavior is to better understand the solubility of lithium in potassium at higher temperatures.

- **Impact of ARC Tube Swelling on System Actuation**: As the ARC systems remain in the core, swelling is expected to take place in the ARC-tubes due to neutron irradiation. This swelling may reduce the diameters of both the inner and outer ARC-tubes and lead to different actuation characteristics compared to "fresh" ARC systems. It is important to account for this for multiple reasons. First, the small diameters of the ARC-tubes raises the possibility for capillary forces to interfere with ARC system dynamics. Second, the reduced ARC-tube diameters resulting from swelling will likely lead to faster actuation. Because it was shown in the transient studies of this work that extremely rapid actuations may lead to oscillatory behavior, it is important to understand the swelling behavior so that oscillations can be avoided.

- **Loading Fluids into ARC System**: While the procedure for assembling an ARC system has been extensively explored, the procedure for loading the ARC fluids into the system during assembly is still not entirely clear. Because both lithium and potassium are solid at room temperature, they may be loaded in solid form and allowed to stratify once melted. However the inert gas must be loaded at pressure, which may be complicated by the need to perform accurate welds once the gas has been loaded. Additionally, while the fluids will remain properly stratified once they are in the proper configuration, it may be difficult to ensure that none of the inert gas or absorber fluid sit on top of the expander fluid within the upper reservoir when they are initially loaded. Ultimately this is not viewed as a barrier to realization of the ARC system concept, but the current study has not devised a solution to this particular issue.

- **Impact of ARC System Inclusion on Fuel Recycling**: Because ARC systems may be desired in a wide variety of SFR cores, the prospect of recycling fuel in assemblies that contain ARC systems should be investigated. Most recycling processes begin with some form of chopping and dissolution of each assembly, typically performed in open air. Typically this would be proceeded by a thorough scrubbing of each assembly to remove sodium from the exterior due to its reactivity with air and water. For assemblies with ARC systems included, large reservoirs of potassium, which is also reactive with air and water, now must be dealt with during the chopping and dissolution phases.

This may complicate the process and may necessitate the draining of each ARC system prior to reprocessing.

- **Use of Point Kinetics**: In most SFR cores, the use of point kinetics is justified due to the tight neutronic coupling between different regions of the core. However, for very large cores with many blanket assemblies, point kinetics may not be as well suited. This study assumed that point kinetics was a valid approximation for the B&B core, but it is possible that some transients, such as a localized flow-blockage, may induce significant asymmetries into the response. In cases such as these, ARC systems may not actuate uniformly across the core, and spatial dynamics of the transient may be important to accurate predictions. Another especially important case would be the breach of an ARC system leading to localized reactivity transients, which have the potential to induce spatial reactivity oscillations. This has not been investigated in this work.

- **Simultaneous Actuation Assumption**: In the current analysis, it was assumed that all ARC systems actuate simultaneously in response to a core heat-up. However, because each assembly will have a somewhat different outlet temperature, the actuation of each ARC system will not be simultaneous for a number of reasons. First, the absorber level within each ARC system will be different at the beginning of any actuation due to the steady-state variation in outlet temperatures. Second, because some transients may be more spatially-localized than others, it is possible that a heat-up in one section of the core may lead to the actuation of some systems much more rapidly than others that are further away from the initiating event. Finally, because some assemblies may be very over-cooled during steady-state operation, it is possible that these assemblies may not actuate nearly as strongly as others with a lower power-to-flow ratio. These uncertainties should be quantified in order to fully understand the dynamics of any transient with the ARC system included.

- **Impact of Lower Reservoir Temperature on Actuation**: During both the ULOF and UTOP transients, the inlet temperature does not change appreciably. However the defining characteristic of the ULOHS is a change in the inlet coolant temperature, some of which will be communicated through conductive and convective heating to the lower reservoir. As such, the expander fluid located in the lower reservoir will thermally expand, in addition to the expansion taking place in the upper reservoir. This thermal expansion has not been quantified or accounted for in the transient simulations performed thusfar, meaning the transient simulations likely underestimate the speed of ARC system actuation during the ULOHS scenario. While this may be the case, it is not expected that this will have important consequences due to the fact that the ULOHS was consistently the least challenging transient. Additionally, the kinetic behavior during the ULOHS exhibited no signs of oscillatory or unstable behavior even in very aggressive ARC system designs, and therefore it is anticipated that a slightly faster actuation is unlikely to induce oscillatory effects.

- **Impact of ARC Tube Axial Temperature Distribution**: Similar to the previous point, the axial temperature distribution of the ARC system is not accounted for in any of the transient simulations. This will have an impact on multiple aspects, but most importantly the density of the absorber fluid and the speed of actuation. Because the absorber fluid starts below the core, it will be at the temperature of the inlet coolant. However as a transient progresses, the absorber fluid will enter the active core where it will heat up. In rapid transients, this heating will likely be slow in comparison to the speed at which the fluid enters the core, and so impacts are likely to be small in the initial phase of the transient. In slower transients, however, the rate of heat transfer to the absorber fluid may be large enough that thermal expansion of the absorber fluid should be accounted for in determining the level of the fluid in the core. Additionally, during transients that terminate with elevated core temperatures, the heat up of the absorber fluid will cause it to have a lower density, and thus its effectiveness as a neutron poison will diminish. Depending on how high the core temperatures get, this effect may be more or less pronounced.

- **One-way Actuation Modification**: It was shown that the ARC system may not allow for fully-passive safety in the large B&B core of this study due to oscillatory behavior. Recent follow-up studies to this project have suggested that a modification to the standard ARC system may be made to allow for fully-passive safety even in challenging cores such as the B&B. This modification would involve the addition of a passive "valve" which preferentially allows flow in one direction more than the other. This would allow for rapid forward actuation of the system but retarded reverse actuation. The feasibility of such a modification, which will further complicate the assembly manufacturing process and possibly introduce additional stresses on ARC system components during actuation, has not yet been confirmed. However, preliminary studies of this modified ARC system have shown that it may be able to completely avoid oscillations in ARC-system responses, and thus warrants further study.

11.2 Summary and Ranking

A number of gaps exist concerning transport and thermodynamic properties of the ARC system fluids, which are particularly important if the ARC system is to be included in long-lived cores. These gaps may only be resolved through experimental measures and will likely require significant resources. A separate category of gaps may be resolved through more detailed modeling, including the impacts of neglecting axial temperature gradients within the ARC system fluids and the use of point kinetics. These gaps may be resolved without any extra experimentation, although some will require extensive modeling efforts. Another category deals with aspects which require engineering and process design. These gaps, including the loading of system fluids and the impact on fuel recycling, will require additional analysis similar to that performed in this project to determine the ARC system manufacturing process. The final technology gap, the potential for a modification to allow one-way actuation, will require both additional experimentation and simulation, but may have the potential to greatly enhance ARC system performance and applicability.

For each of the gaps, Table 19 provides a preliminary rating to characterize two aspects. First, the importance of the gap is rated on a scale of 1-3, with 1 signifying very high priority and 3 signifying relative unimportance. Second, the gaps are rated with respect to the amount of effort it will take to resolve them, with 1 signifying a gap that will be relatively straightforward to resolve and 3 signifying a gap that will require extensive effort. Therefore, a gap with ratings of 1 in both categories will be of both high importance and low effort, and a gap with ratings of 3 in each category will be of great difficulty and minor significance. These ratings may be used to determine directions for future work.

Table 19: Technology gaps rated according to their importance and ease of resolution.

Gap	Importance	Difficulty
Solubility of reaction products	2	3
Diffusion coefficients	3	3
Solubility at elevated temperatures	2	3
ARC tube swelling	2	1
Loading of system fluids	1	1
Impact on fuel recycling	3	2
Use of point kinetics	2	2
Simultaneous actuation	2	2
Lower reservoir temperature	3	3
ARC tube axial temperature distribution	3	2
One-way actuation modification	1	2

12 Summary

This project examined a number of aspects related to the incorporation of the ARC system into SFRs. The project began by fleshing out the principles and design of ARC systems. First, the literature concerning physical properties of the ARC system constituents was surveyed and the relevant properties were identified. Once complete, the physical design of ARC systems and how they fit into the standard SFR assembly design was studied in detail. The process for manufacturing assemblies including ARC systems was laid out and it was confirmed that ARC system installation does not overly complicate the manufacturing process. Then the time behavior of ARC systems in response to coolant temperature changes was examined using CFD to understand how quickly the system can actuate during a transient. Through an ad-hoc optimization process, the time-response was reduced to obtain a minimum τ value of 1.3 s, corresponding to the geometry of the ABR reference core.

Next, transients were simulated in two reference cores using the SAS4A-SASSYS-1 transient code system, both with and without ARC system inclusion. In order to enable the modeling of LOF transients, where heat transfer to the upper reservoir is significantly degraded, modifications to SAS4A-SASSYS-1 were made and tested. In the first reference core, an oxide-fueled ABR, the ARC system was found to significantly improve transient performance by increasing the margins to fuel melting and coolant boiling by roughly 800°C and 200°C, respectively. Although the response of the ARC system is relatively quick, it was found that $\tau = 1.3$ s was not fast enough to avoid small induced oscillations. Instead, it was found effective to increase τ so that oscillations are damped. Therefore it was found that ARC system inclusion could greatly benefit the passive safety of the ABR design. Based on these results, modifications to the ABR design were made to improve economic performance. By including the ARC system, it was found that the core can be redesigned with a higher power and shorter flow halving time while maintaining transient performance better than the original design without ARC system inclusion.

Whereas the ARC system proved consistently beneficial in the ABR core, the response in the second reference core, a metal-fueled B&B, was more complicated. Due to the combination of a strong positive coolant void feedback and the high thermal conductivity of metallic fuel, boiling was seen within 20 minutes for all three unprotected transients examined. By incorporating the ARC system, boiling in the ULOHS could be avoided, but large temperature-reactivity oscillations were seen in both the UTOP and ULOF that led to boiling. By increasing the heat transfer delay from the coolant to the upper reservoir, the oscillations could be made small enough to achieve passive safety in the UTOP scenario. However no combination of ARC design parameters could be devised to achieve passive safety in all three transients simultaneously. Therefore, while significant benefits were seen, the desired result of complete passive safety was not achieved.

Once it was established that the ARC system has the potential to benefit transient performance, the potential negative consequences of including ARC systems into the core were quantified. It was found that the neutronic penalty and the loss of lithium absorber are not likely to be significant barriers to implementation. The production of tritium, however, was found to be of greater concern due to the large volume of lithium in the lower reservoir. Although of potential concern, methods for mitigating the issue were proposed and found effective, and therefore it is not foreseen that this will preclude ARC system inclusion. Additionally, a simplified study was performed to quantify the potential effects of a breach in the ARC system during full-power operation. While the release of the inert gas into the coolant may insert reactivity by introducing a coolant void, this mechanism was conservatively evaluated to be negligible. Finally, the project concludes with an examination of gaps that should be resolved before ARC system technology can be viewed as mature. In total, it has been found that the ARC system may provide extensive benefits to a class of medium-sized SFRs, while benefits to a lesser extent are seen in the class of low-leakage B&B cores. Based on the results of this study, further development is recommended.

List of Publications

1. S. Qvist, C. Hellesen, R. Theile, A. Dubberley, M. Gradecka, E. Greenspan, "Autonomous Reactivity Control (ARC) – Principles, geometry, and design process," Nuclear Engineering and Design, 307 (2016).

2. S. Qvist, C. Hellesen, M. Gradecka, A. Dubberley, T. Fanning, E. Greenspan, "Tailoring the response of Autonomous Reactivity Control (ARC) systems," Annals of Nuclear Energy 99 (2017).

3. C. Keckler, S. Qvist, T. Fanning, M. Fratoni, E. Greenspan, "SAS4A/SASSYS-1 Simulation of ARC System in Oxide ABR for Improved Safety Performance," Transactions of the American Nuclear Society, American Nuclear Society Winter Conference, Washington D.C. (2017).

4. C. Keckler, M. Fratoni, E. Greenspan, "On the Importance of Control Assembly Layouts in Standing Wave B&B Cores," in proceedings of PHYSOR 2018, Cancun, MX (2018).

5. C. Keckler, A. Atamturk, M. Fratoni, E. Greenspan, "A Mixed-Integer Linear Programming Method for Optimal Orificing in Breed-and-Burn Cores," Transactions of the American Nuclear Society, American Nuclear Society Annual Conference, Philadelphia, PA (2018).

References

[1] T. KIM, W. YANG, C. GRANDY, and R. HILL, "Core design studies for a 1000 MWth Advanced Burner Reactor," *Annals of Nuclear Energy*, **36**, *3*, 331–336 (apr 2009).

[2] A. WALTAR, D. TODD, and P. TSVETKOV, editors, *Fast Spectrum Reactors*, Springer, New York (2012).

[3] M. TAKAMATSU, T. SEKINE, T. AOYAMA, and M. UCHIDA, "Demonstration of Control Rod Holding Stability of the Self Actuated Shutdown System in Joyo for Enhancement of Fast Reactor Inherent Safety," *Journal of Nuclear Science and Technology*, **44**, *3*, 511–517 (2007).

[4] M. EDELMANN, G. KUSSMAUL, and W. VATH, "Improved Fast Reactor Safety by Passive Shut-Down," *Progress in Nuclear Energy*, **29**, 379–386 (1995).

[5] M. KAMBE and M. UOTANI, "Design and Development of Fast Breeder Reactor Passive Reactivity Control Systems: LEM and LIM," *Nuclear Technology*, **122**, *2*, 179–195 (may 1998).

[6] S. QVIST and E. GREENSPAN, "An Autonomous Reactivity Control system for improved fast reactor safety," *Progress in Nuclear Energy*, **77** (2014).

[7] S. A. QVIST, *Safety and core design of large liquid-metal cooled fast breeder reactors*, Ph.D. thesis, University of California, Berkeley (2013).

[8] V. B. BOHM and W. KLEMM, "Zur Kenntnis Des Verhaltens der Alkalimetalle zueinander," *Zeitschrift fur anorganische und allgemeine Chemie*, **243**, *1*, 69–85 (1939).

[9] C. W. BALE, "The K-Li (Potassium-Lithium) system," *Bulletin of Alloy Phase Diagrams*, **10**, *3*, 262–264 (jun 1989).

[10] S. ZHANG, *Thermodynamic Investigation of the Effect of Alkali Metal Impurities on the Processing of Al and Mg Alloys*, Ph.D. thesis, The Pennsylvania State University (2006).

[11] H. W. DAVISON, "Compilation of thermophysical properties of liquid lithium," Tech. rep., NASA Lewis Reserch Center, Cleveland, OH (1968).

[12] D. W. JEPPSON, J. L. BALLIF, W. W. YUAN, and B. E. CHOU, "Lithium Literature Review: Lithium's Properties and Interactions," Tech. rep., Hanford Engineering Development Laboratory, Hanford, WA (1978).

[13] C. B. ALCOCK, M. W. CHASE, V. P. ITKIN, and M. W. CHASE, "Thermodynamic Properties of the Group IA Elements Thermodynamic Properties of the Group IA Elements," *Journal of Physical and Chemical Reference Data*, **23**, 385 (1994).

[14] O. FOUST, *Sodium-NaK Engineering Handbook*, Gordon and Breach (1972).

[15] L. LEIBOWITZ and R. A. BLOMQUIST, "Thermal conductivity and thermal expansion of stainless steels D9 and HT9," *International Journal of Thermophysics*, **9**, *5*, 873–883 (sep 1988).

[16] N. YAMANOUCHI, M. TAMURA, H. HAYAKAWA, and T. KONDO, "Accumulation of engineering data for practical use of reduced activation ferritic steel," *Journal of Nuclear Materials*, **191-194** (1992).

[17] R. OHSE, editor, *Handbook of Thermodynamic and Transport Properties of Alkali Metals*, Blackwell Scientific Publications (1985).

[18] K. J. BOWLES, "VAPOR PRESSURE OF POTASSIUM TO 2170 K," Tech. rep., NASA Lewis Research Center, Cleveland, OH (1968).

[19] H. C. YOUNG and A. G. GRINDELL, "Summary of design and test experience with cesium and potassium components and systems for space power plants," Tech. rep., Oak Ridge National Laboratory, Oak Ridge, TN (1967).

[20] S. J. GRISAFFE and D. C. GUENTERT, "ADVANCED RANKINE AND BRAYTON CYCLE POWER SYSTEMS: Materials needs and opportunities," Tech. rep., NASA Lewis Research Center, Cleveland, OH (1974).

[21] J. CAHALAN and T. H. FANNING, "The SAS4A / SASSYS-1 Safety Analysis Code System," Tech. rep., Argonne National Laboratory, Lemont, IL (2012).

[22] M. A. SMITH, C. ADAMS, W. S. YANG, and E. E. N. E. D. LEWIS, "VARI3D & PERSENT: Perturbation and Sensitivity Analysis," Tech. rep., Argonne National Laboratory, Lemont, IL (2013).

[23] J. HOU, S. QVIST, R. KELLOGG, and E. GREENSPAN, "3D in-core fuel management optimization for breed-and-burn reactors," *Progress in Nuclear Energy*, **88** (2016).

[24] J. LEPPANEN, "Serpent - a Continuous-energy Monte Carlo Reactor Physics Burnup Calculation Code: User's Manual," (2015).

[25] M. AUFIERO, A. BIDAUD, M. HURSIN, J. LEPPÄNEN, G. PALMIOTTI, S. PELLONI, and P. RUBIOLO, "A collision history-based approach to sensitivity/perturbation calculations in the continuous energy Monte Carlo code SERPENT," *Annals of Nuclear Energy*, **85**, 245–258 (nov 2015).

[26] M. AUFIERO, M. MARTIN, and M. FRATONI, "XGPT: Extending Monte Carlo Generalized Perturbation Theory capabilities to continuous-energy sensitivity functions," *Annals of Nuclear Energy*, **96**, 295–306 (2016).

[27] C. KECKLER, A. ATAMTÜRK, M. FRATONI, and E. GREENSPAN, "A Mixed-Integer Linear Programming Method for Optimal Orificing in Breed-and-Burn Cores Chris Keckler," in "Transactions of the American Nuclear Society," Philadelphia, PA (2018).

[28] D. WADE, R. WIGELAND, and D. HILL, "The safety of the IFR," *Progress in Nuclear Energy*, **31**, *1-2*, 63–82 (jan 1997).

[29] S. QVIST and E. GREENSPAN, "Design Space Analysis for Breed-and-Burn Reactor Cores," *Nuclear Science and Engineering*, **182**, *2*, 197–212 (feb 2016).

[30] C. KECKLER, M. FRATONI, and E. GREENSPAN, "On the Importance of Control Assembly Layouts in Standing Wave B & B Cores," in "PHYSOR 2018: Cancun," (2018), pp. 4058–4069.

[31] R. BATCHELOR and J. H. TOWLE, "The interactions of neutrons with Li6 and Li7 between 1.5 and 7.5 MeV," *Nuclear Physics*, **47**, *C*, 385–407 (1963).

[32] D. GREEN and R. PERRY, *Perry's Chemical Engineers' Handbook*, 8 ed.

[33] E. A. HOFFMAN, R. N. HILL, and W. YANG, "Preliminary Core Design Studies for the Advanced Burner Reactor over a Wide Range of Conversion Ratios," Tech. rep., Argonne National Laboratory, Lemont, IL (2006).

[34] N. E. STAUFF, L. BUIRON, B. FONTAINE, and G. RIMPAULT, "Methodology for Designing a Sodium-Cooled Fast Reactor with Inherent Safety," *Nuclear Technology*, **181**, *2*, 241–250 (2013).

[35] M. SCHIKORR, E. BUBELIS, B. CARLUEC, and J. CHAMPIGNY, "Assessment of SFR reactor safety issues. Part I: Analysis of the unprotected ULOF, ULOHS and UTOP transients for the SFR(v2b-ST) reactor design and assessment of the efficiency of a passive safety system for prevention of severe accidents," *Nuclear Engineering and Design*, **285**, 249–262 (apr 2015).

[36] "Reactor Coolant Pump Flywheel Integrity," Tech. rep., Nuclear Regulatory Commission (1975).

[37] T. SUMNER, *Effects of fuel type on the safety characteristics of a sodium cooled fast reactor*, Ph.D. thesis, Georgia Institute of Technology (2010).